Science & Technology Facilities Council

Technical Report
RAL-TR-2019-006

SCARF Annual Report 2017-2018

D Ross (editor)

April 2019

Enquiries concerning this report should be addressed to:

RAL Library
STFC Rutherford Appleton Laboratory
Harwell Oxford
Didcot
OX11 0QX

Tel: +44(0)1235 445384
Fax: +44(0)1235 446403
email: libraryral@stfc.ac.uk

Science and Technology Facilities Council reports are available online at: http://epubs.stfc.ac.uk

ISSN 1358-6254

Science & Technology Facilities Council

SCARF Annual Report 2017-2018

Version: 1.0

Date: 15/04/2019

Edited by Derek Ross (derek.ross@stfc.ac.uk) 01235 445651

Content written by the respective authors

Date	Revision	Changes
18/01/19	0.1	Initial document
14/02/19	0.2	Addition of scientific contributions
25/03/19	0.9	Reformatting and restructuring
15/04/19	1.0	Released version

Abstract

Annual Report on the Usage and Scientific Impact of the SCARF Service

Dissemination

This is a public document

1. SCARF SERVICE

SCARF is a High-Performance Cluster for STFC staff, Facilities (ISIS, DIAMOND, CLF) and their users. The SCARF Service was started in 2004 and has been upgraded year on year and now represents a significant capital investment in High Performance Computing. Overall SCARF now has over 10000 CPU cores, 80TB memory and 1PB of disk space (Details in Appendix 1).

This report covers the year 2017-18 and outlines the research that SCARF has enabled.

SCARF Usage by Department

Each time a researcher uses the SCARF service the CPU time used is recorded. Jobs submitted to SCARF used 46.1 million CPU Hours during 2017-18.

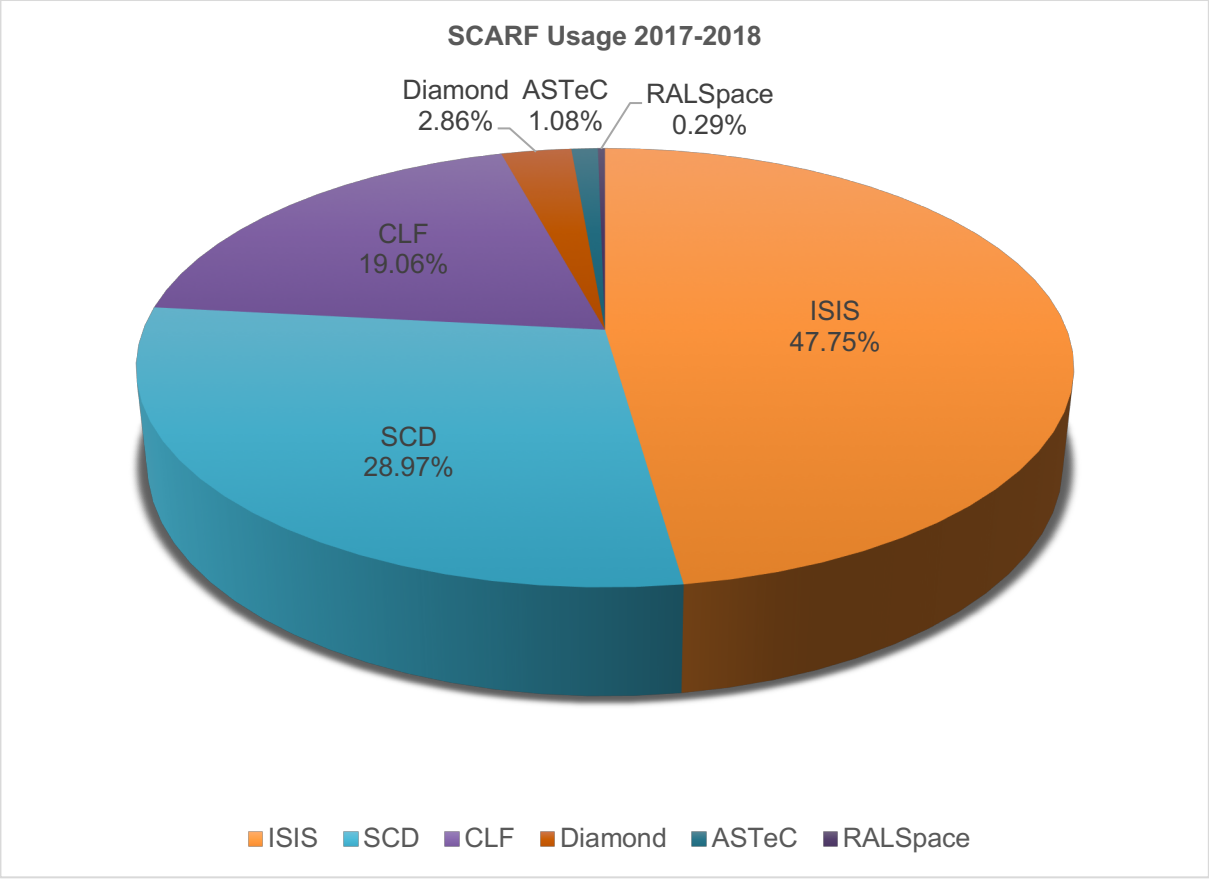

Figure 1:Pie chart showing percentage usage of the SCARF service by department.

It is clear from the usage chart that ISIS, CLF and Scientific Computing are the heaviest users of SCARF. The table below shows the number of active users affiliated with e.g. Staff, collaborating with or using the facilities of various STFC departments and significant external facilities such as Diamond or CCFE. We have stopped counting External access users separately; instead they are now counted under the STFC Department they are collaborating with. The Hartree Centre has been moved from the Scientific Computing Department to its own department, but this is not yet reflected in the SCARF accounting configuration.

	2017-18			2016-17			2015-16		
Dept	Active Users	CPU hrs	%	Active Users	CPU hrs	%	Active Users	CPU hrs	%
SCD/Hartree	89	13366201.2	29.0	71	12229692.6	34.7	52	11394064.3	36.2
ISIS	79	22031657.5	47.7	61	12998061.7	36.8	54	10413282.5	33.1
CLF	60	8794902.9	19.1	56	7893198.1	22.4	43	6829135.47	21.7
DIAMOND	16	1320589.3	2.9	11	1717467.6	4.9	3	1653629.8	5.2
ASTEC	2	496252.9	1.1	0	0	0	2	58299.64	0.19
RAL Space	1	133180.9	0.3	4	432680.9	1.2	5	989267.1	3.1
CCFE	0	0	0	0	0	0	1	81.59	0
PPD	0	0	0	3	15108.7	0.04	0	0	0
Totals	**247**	**46142784.7**	**100**	**206**	**35286209**	**100**	**165**	**31451022**	**100**

Figure 2: Table displaying detailed CPU usage from 2017-18 comparing with 2015-16 and 2015-16

A significant amount of computational resource has been used on SCARF; section 3 highlights some of the scientific achievements that have been enabled.

SCARF Availability

The aim is to keep SCARF available to users as much as possible. SCARF was taken offline for 3 days during power testing of the RAL machine room. Upon completion of this power testing SCARF was unstable for a short period due to an interaction between system drivers causing RHEL6 nodes to reboot. Security patching occurred several times over the period, requiring downtimes on each frontend to reboot them.

SCARF Developments 2017-18

Major SCARF Developments are listed below. A more detailed list can be found in Appendix 5

- New capacity added in July 2018
  - 3552 Intel Xeon Gold 6216 cores for general use
- SCARF migrated to the RHEL 7 Operating System
- SCARF migrated to the SLURM batch system

Future Developments

As SCARF have now moved to a new storage system, the existing storage system will be decommissioned. In addition, several old SCARF hardware generations have been removed from service and will be decommissioned. Several aspects of functionality which were lost in the move from LSF to SLURM, particularly the web portal, will be reimplemented. A review of the SCARF website will take place to ensure the content is up to date and accurate and reflecting the large number of changes which have taken place this year, a training course for SCARF users will be organised

Help and Support

For any queries concerning the SCARF service, please email the SCARF Helpdesk scarf@hpc-support.rl.ac.uk

2. PUBLICATIONS AND PRESENTATIONS

The publications and presentations for research that made use of SCARF are a way of measuring the impact that SCARF itself has.

Publications

A list of publications is given in Section 6. A way of estimating the impact that SCARF has had is to analyse the Journal Impact Factor using the Journal Citation Reports published by Thomson Reuters (2017). The average Impact Factor for Journals published as a result of using SCARF is 3.752.

Presentations

Scientists have presented their work at 25 international conferences (See Section 6). This helps to demonstrate that the science enabled by SCARF is world class.

3. SCIENCE HIGHLIGHTS

Kagome modes, a new route to ultralow thermal conductivity?

D.J. Voneshen[1], M. Ciomaga Hatnean[2], T.G. Perring[1], H.C. Walker[1], K. Refson[3,1], G. Balakrishnan[2] and J.P. Goff[3].

1. *ISIS Pulsed Neutron and Muon Source*
2. *Department of Physics, University of Warwick*
3. *Department of Physics, Royal Holloway*

The efficiency of jet turbine engines depends heavily upon the temperature that can be reached within them. Current engines operate several hundred degrees above the melting temperature of the superalloy turbine blades [1]. This is only made possible by cooling air forced through the inside of the blade, and a thermal barrier material on the outside which keeps the surface below its melting temperature and prevents oxidisation [2].

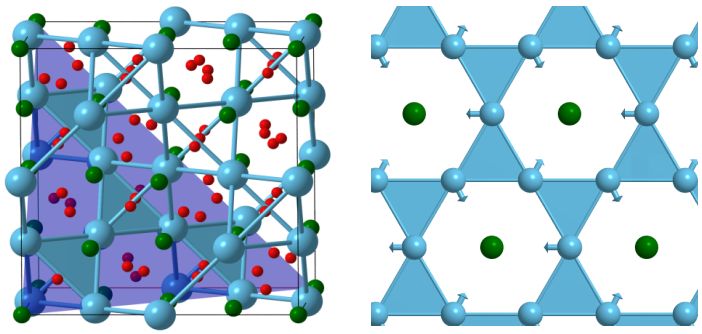

Figure 3: (a) The conventional cubic cell of the pyrochlore $La_2Zr_2O_7$ with La in light blue, Zr in green and O in red. A kagome plane normal to the [111] direction is highlighted in blue. (b) A kagome mode in LZO with the ionic displacements shown. There is almost no motion of the Zr, O or the La site linking (111) planes together.

Using calculations performed on the SCARF cluster with the CASTEP code and inelastic neutron scattering performed on MERLIN at ISIS we have studied the next generation thermal barrier $La_2Zr_2O_7$. Our calculations show that there are strongly anharmonic vibrations of the rare-earth kagome planes (figure 3) which are likely responsible for the low thermal conductivity observed. These calculations are validated by comparison to the MERLIN experiment (figure 4). The strong anharmonicity is intrinsic to the kagome lattice and our results suggest that other kagome compounds will be fruitful places to search for low thermal conductivity materials [3].

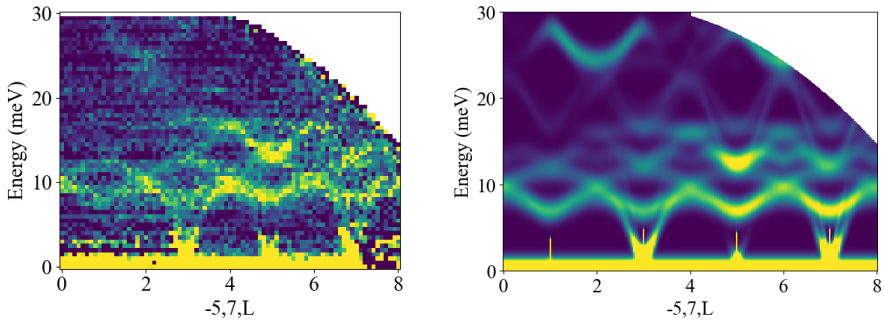

Figure 4: (a) The phonon spectrum obtained on MERLIN. (b) The calculated phonon from CASTEP running on SCARF.

References:

[1] J. H. Perepezko, *Science,* **326** (5956), 1068-1069 (2009)
[2] N. P. Padture, *Science*, **296**, (5566), 280-284 (2002)
[3] DJ Voneshen et al. arXiv:1809.06265 (2018)

Design of analysers for High-Resolution Broadband Neutron Molecular Spectrometers

M. Zanetti[1,2], S. Rudić[2], G. Gorini[3] and F. Fernandez-Alonso[2,4]

1. *Consilio Nazionale delle Ricerche, DSFTM, Roma, Italia*
2. *ISIS Neutron and Muon Source, Rutherford Appleton Laboratory, Chilton, Didcot, UK*
3. *Università degli Studi di Milano-Bicocca, Milano, Italia*
4. *University College London, London, UK*

TOSCA (ISIS, UK) and VESPA (joint Italy-UK design for the European Spallation Source - Lund, Sweden) are high-resolution, indirect-geometry inelastic neutron spectrometers that can operate from slightly negative energy transfers to 500 meV, and beyond, at pulsed neutron sources. In the past, our work was primarily devoted to TOSCA [1] upgrades, covering the neutron-guide design, the benchmarking of the moderator model and the development of the secondary-spectrometer design, followed by similar efforts for VESPA, by means of the McStas Monte Carlo ray-tracing package [2] – see previous SCARF reports for additional details. As the VESPA design and the feasibility studies for the TOSCA secondary upgrade progress, the choice of using large and curved analysers, built with high-mosaicity HOPG crystals, to allow for an unprecedented sample coverage and sensitivity, is being thoroughly assessed.

For a broadband inelastic spectrometer, the design of such analysers requires a careful selection of the position and orientation of each HOPG crystal that is used to select the final energy in the secondary spectrometer (i.e., the path of neutrons between the sample and the detectors), in order to achieve a high spectrum solution on this kind of instruments. In particular, according to analytical calculations based on simplifying assumptions, the HOPG tiles are required to focus the secondary neutrons to a unique point in space, in which the time of arrival is equal for any possible trajectory and selected energy. Starting from this scratch design, simulation-aided optimization and parametric studies can be performed with the aid of modern neutron-transport codes, which can take accurately into account the effects that were not considered during the first step.

As an example, Fig.5 reports the performance of the analysers which are being currently optimized for VESPA. The design of the new TOSCA analysers are being designed with the same approach.

The secondary time-of-flight and energy distribution of neutrons on a detector bank are presented there in the form of pixel maps. Differently from back-of-the-envelope calculations, here it is possible to take into account the effect of sample and HOPG tile size and mosaicity, thus it became apparent that neutrons are not focused in a single pixel, but they create a larger spot on the detection plane. To achieve high resolution at large energy transfers, the minimization of the temporal spread (here represented by the standard deviation) within each pixel is necessary and is object of simulation-aided optimization. From the computational side, the McStas code has been extended in order to accept a CAD-generated grid that stores the position and orientation of each HOPG tile in the analyser. During the simulation, the grid is probed after scattering from the sample and a single tile is dynamically assigned to its position, and neutrons which do not intercept the analysers are suppressed, and this highly benefits computational times.

Furthermore, HOPG mosaicity effects are being studied with McStas. It was shown that increasing the HOPG mosaicity, which increases the angular acceptance for Bragg scattering from the HOPG crystals, can significantly increase the number of neutrons collected at the detectors [3]. In parallel, we have also verified the effect that an increase of the mosaicity has on the instrumental resolution, which degrades at the high energy

transfers due to an increase of the temporal spread at the detectors. Another studied effect is related to the tolerances in HOPG production, meaning that each tile will not have the same exact mosaicity grade. This is realised by storing in a number of CAD-generated analyser grid a different mosaicity level for each tile, as sampled from known distributions with given mosaicity boundaries. By studying the variations in intensity and resolution for the different cases, it is possible to identify the right mosaicity tolerances for the best performance of the instruments.

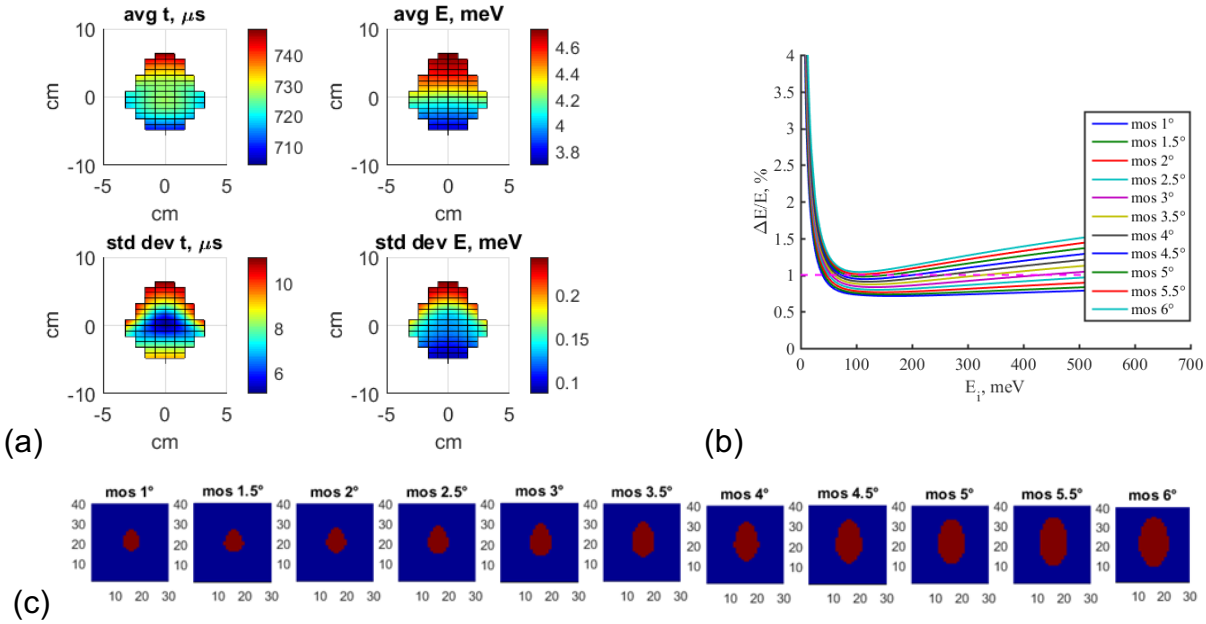

Figure 5: Simulation of VESPA secondary spectrometer performance. (a) pixel maps of secondary time-of-flight and final energy and their standard deviation with 2° mosaicity at the position-sensitive detector bank (the neutron footprint is limited to the pixels in which the intensity is within 1/500 of the maximum); (b) resolution of VESPA as a function of mosaicity; (c) footprint of secondary neutrons reaching the detector bank for different mosaicities.

The simulations performed on the SCARF cluster required very high statistics in order to generate high-quality results. Depending on the case, in particular on the virtual sample adopted during the studies, we used up to 800 cores for up to twenty-four-hour runs. SCARF was essential to these simulations because the physical processes involved are manifold and difficult to disentangle without recourse to detailed simulations, i.e., neutron moderation, reflection in the neutron guides, scattering processes and Bragg diffraction onto the analyser.

These activities to attain a sound design of the new instruments using simulation continue apace, with the exciting opportunity of benchmarking the simulation results with ad-hoc test rigs in the near future.

References:

[1] S. F. Parker, F. Fernandez-Alonso, A. J. Ramirez-Cuesta, J. Tomkinson, S. Rudić, R. Pinna, G. Gorini, and J. Castañon, 2014. Recent and future developments on TOSCA at ISIS. Journal of Physics: Conference Series 554, 012003.

[2] P. Willendrup, E. Farhi, K. Lefmann, 2004. McStas 1.7 - a new version of the flexible Monte Carlo neutron scattering package, *Physica B* 350 e735-e737.

[3] [3] R.S. Pinna, S. Rudić, M. Zanetti, D. Zacek, S.F. Parker, G. Gorini, F. Fernandez-Alonso. TOSCA Secondary Spectrometer Upgrade. RAL Technical Reports RAL-TR-2017-013. STFC, 2017.

Salt effects on Donnan equilibrium in montmorillonite

Ya-Wen Hsiao[1] and Magnus Hedström[2]

1. *Scientific Computing Department, STFC Daresbury Laboratory, U.K.*
2. *Clay Technology AB, Ideon Science Park, Lund, Sweden*

Smectite clay has low hydraulic conductivity, which is a desirable feature for barrier materials used in high-level nuclear waste repositories, as diffusion which is a slow process, will dominate transport to and from the containers containing the radioactive material. Still, it is important to understand the diffusion rates and paths of charged species, including escaping radionuclides, corroding agents that may jeopardize the waste containers, and corrosion products, through clay.

As a continuation from our previous work of monovalent salt [1], we investigated $CaCl_2$ diffusion between external bulk solution and bihydrated montmorillonite interlayers using atomistic molecular dynamics (MD) simulations. A range of different bulk concentrations were tested. The results of the simulations showed that excess salt entered the interlayers, in addition to the counterions compensating the negative layer charges. Numerically consistent predictions of the interlayer Cl^- concentration were obtained between MD and the Donnan equation augmented by the hydration energy cost as the excess free energy. This demonstrates the validity of using the approximation of a Donnan potential for the interlayer electrostatics. The MD density profiles show that cations and anions in the clay interlayers share the same physical space in the center of the two water layers. Thus, there are no separated anion and cation porosities in the montmorillonite-bulk system. Furthermore, our results demonstrate the different behaviour of the partition coefficient for a 2:1 salt as compared to a 1:1 salt. For a 1:1 salt, the partition function increases linearly with the bulk concentration, while the partition function of a 2:1 salt has a square root dependency. This results in substantially higher montmorillonite salt concentrations upon contact with $CaCl_2$ as compared to NaCl.

To be submitted to Journal of Physical Chemistry C.

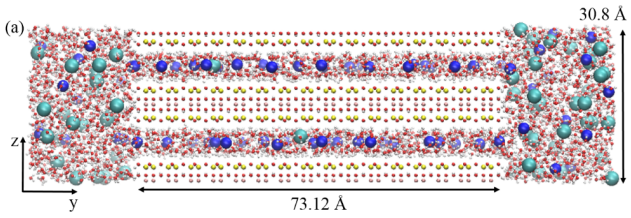

Figure 6: Simulation snapshot: large cyan/blue spheres: Cl-/Ca2+

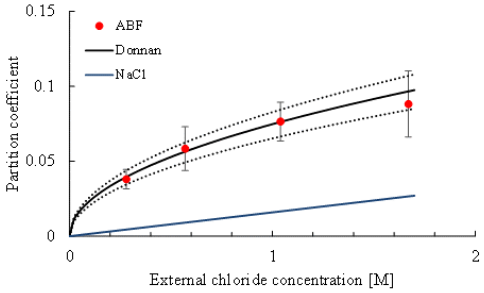

Figure 7: Cl^- partition coefficient for $CaCl_2$ obtained from MD (red dots) and Donnan equation (black curve), and comparison to that of NaCl (blue line)

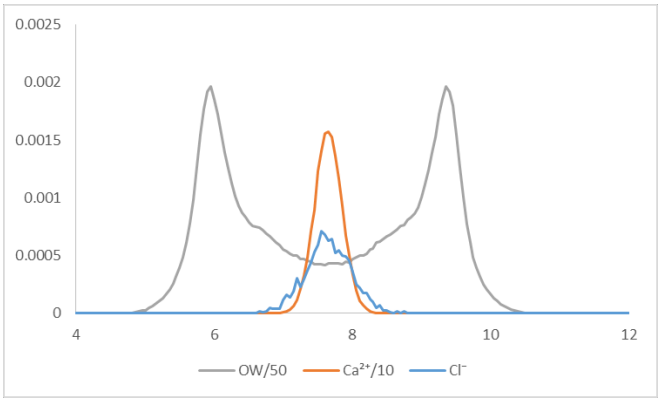

Figure 8: Density profiles in the interlayer along z-direction. Blue: Cl^-, orange: Ca^{2+}, grey: water oxygens.

References:

[1] Hsiao, Y.-W.; Hedström, M. Molecular Dynamics Simulations of NaCl Permeation in Bihydrated Montmorillonite Interlayer Nanopores. J. Phys. Chem. C **119**, 17352−17361 (2015).

Local adsorption structure and bonding of porphine on Cu(111) before and after self-metalation

D A Duncan

Diamond Light Source

Energy scanned photoelectron diffraction (PhD) is a unique technique that provides chemically specific, highly local structural information with a resolution down to hundredths of an Ångstrom. Broadly, in PhD, when a photoelectron is emitted from a material it has a finite probability to be emitted in almost every direction, a subset of those photoelectrons will be emitted towards the detector, but another subset will be emitted away from the detector, back into the material. However, as electrons are strongly interacting, there is a high probability that these electrons will be scattered, and that they will be scattered towards our detector. Due to the wave-like nature of electrons, these different pathways will interfere with one another resulting in a modulation of the photoelectron intensity as a function of the photon energy at our detector. However, because the electrons are highly interacting, they can elastically scatter multiple times before being scattered towards our detector, and thus there are no direct methods for PhD analyses, instead we must perform multiple scattering calculations, comparing theoretically calculated PhD modulations for a given model with those measured experimentally.

Thus far we have completed studies of two systems using the scarf cluster – free base porphine (2H-P) on Cu(111), and copper porphine (Cu-P) on Cu(111). The resulting structures from this iterative modelling of the experimental data, for 2H-P and Cu-P are shown in Figure 9. Specifically, in this study we were looking at the metalation of porphine by Cu atoms (converting 2H-P to Cu-P). We observed that both molecules adsorb with their centre above a bridge site (which means bridging two nearest neighbour surface atoms), and all four nitrogens in near atop or off atop sites (in other words directly above, or just off directly above a surface atom). The 2H-P adsorbs with the two N atoms that are more off atop closer to the surface (2.11 ± 0.05 Å) than the two N atoms that are more atop (2.27 ± 0.05 Å). In contrast the Cu-P adsorbs with the two N atoms that are more atop closer to the surface (2.11 ± 0.03 Å) and the more off atop N atoms further from the surface (2.40 ± 0.10 Å).

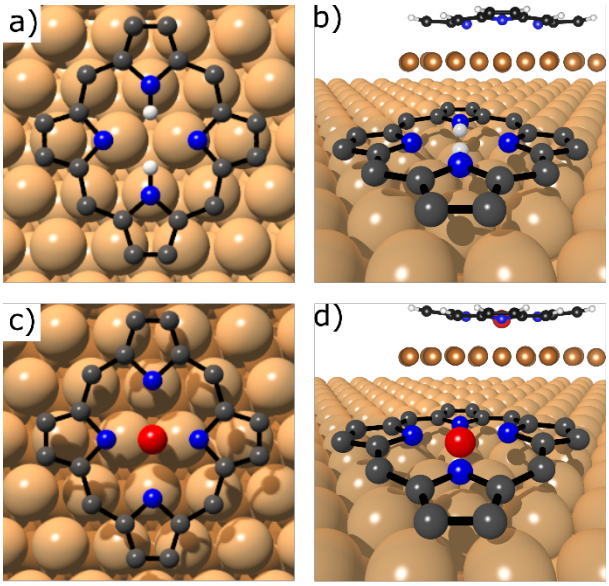

Figure 9: Model of the best fitting structure for (a, b) 2H-P and (c, d) Cu-P adsorbed on Cu(111) shown from (a, c) above and from (b, d) the side, as determined by the PhD analysis. Inset in (b, d) is the corresponding side view of the predicted DFT structure. The H, N, C, surface Cu, and central Cu atoms are depicted by the white, blue, dark grey, light brown, and red spheres, respectively. Note that H atoms are omitted from the experimental structures (they are not modelled in the multiple scattering PhD calculations), except the two H atoms (white spheres in (a) and (b)) of the amino groups in 2H-P, which are solely shown to differentiate the inequivalent N atoms in 2H-P.

Enhancing the propagation of laser-driven-relativistic-electron-beam through the use of graded-resistivity guides.

R. A. B. Alraddadi[1], A. P. L. Robinson[2], J. Pasley[3] and N. C. Woolsey [3]

1. *King Saud University, Riyadh*
2. *STFC Central Laser Facility, CLF*
3. *University of York, York Plasma institute).*

The resistive guiding concept is promising technique to enable the collimation laser-driven relativistic electron beams [1,2]. When a high atomic number (high-Z) wire is embedded in a lower-Z substrate a resistivity gradient is created across the interface between the two materials. This resistivity change enables the growth of a strong magnetic field in range of kT within 100's of femtoseconds. This fast growing and strong magnetic field limits the transverse expansion of the relativistic electrons confining them to wire enabling the propagation of a beam over long distances (100's μm) along the guide.

In our numerical work using SCARF facilities, a new generation of resistive guides has been investigated. We use SCARF-MagnaCarta resources to run three-dimensional Hybrid-PIC code ZEPHYROS [3] to investigate the performance of graded-resistivity guide targets. In these targets, a linear decreasing gradient in the resistivity is formed between the wire and substrate by reducing the atomic number Z of cladding sleeve of material. A two-dimensional slice of the target is shown in Figure 10.

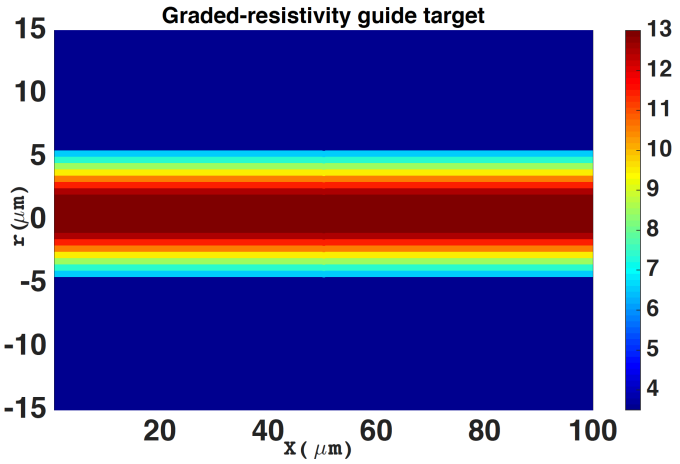

Figure 10: Atomic number maps of a graded-resistivity guide with a guide-element composed of an aluminium core clad in a sleeve of cladding material of decreasing atomic number from Z=13 (aluminium) to Z=6 (carbon).

Using these new guides and typical Vulcan petawatt laser parameters we find an increase in the width of the collimating magnetic field that forms at the material interface. An example cross-section of the magnetic field data is shown in Figure 11. The azimuthal magnetic field (blue curve) peaks close to guide's boundary (indicated by red dashed lines) and extends into the substrate as well as the guide-element. This improves the relativistic electron confinement and limits magnetic field growth in the interior guide.

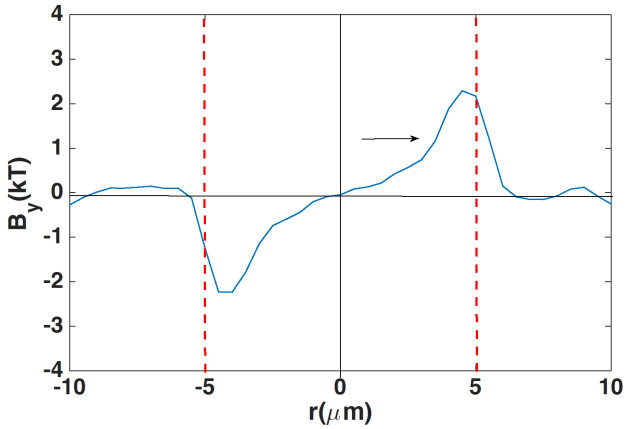

Figure 11: Cross-sections of the magnetic field, as a function of radial position r at x=10μm, taken at 2.2 ps and limited to -10 < r < 10μm in y-midplane. The vertical dashed lines show the boundaries of the guide-element. The arrow shows the gradient in the magnetic field inside the guide-element.

As a result of this extended magnetic field along *r*, simulations show a significant reduction in the temperature gradient and inhomogeneity along the guide as well as higher temperatures. An example of this is shown in Figure 12. These observations are important to future applications.

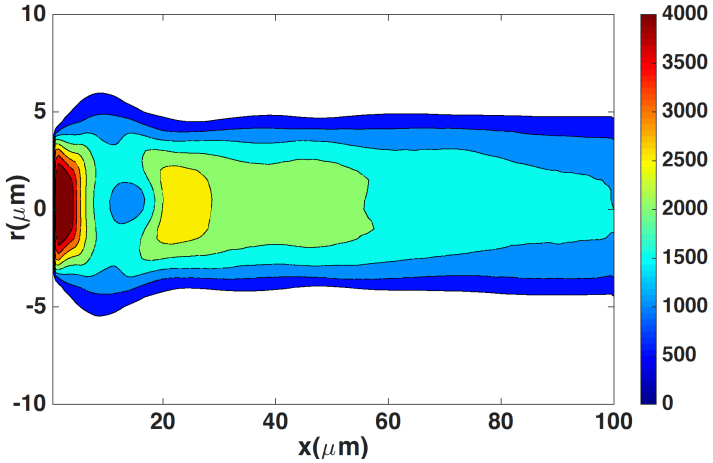

Figure 12: Contour plots of the resistive guide temperature in eV at 2.2 ps along the x- (i.e. propagation) direction in the y midplane (the substrate temperatures are not shown).

References:

[1] A. P. L. Robinson and M. Sherlock, *Phys. Plasmas*,14 (2007)083105.
[2] A. P. L. Robinson et al, *Phys. Plasmas*, 20(2013)122701.
[3] A. P. L. Robinson et al, *Nuclear Fusion,* 54.5 (2014) 054003.

Probing Structure and Mobility of Proteins in the Amorphous State at Low Hydration

Sara Gabrielli[1], Mark Telling[2,3], Gaio Paradossi[1] and Ester Chiessi[1]

1. *Dipartimento di Scienze e Tecnologie Chimiche, Università di Roma "Tor Vergata"*
2. *STFC, Rutherford Appleton Laboratory, Harwell Campus, OX11OQX, UK*
3. *Department of Materials, University of Oxford, Parks Road, Oxford, UK*

Project summary: The characterization of proteins in the dry state provides insight on the effect of lyophilisation on stability and biological activity, with implications in the pharmaceutical industry. Using SCARF, in conjunction with the computing capabilities of the Italian CINECA network, we have performed structural and dynamical analyses of lyophilised and hydrated Apoferritin (Apo), Insulin (Ins) and Lysozyme (Lyso) by means of Molecular Dynamics (MD) simulations; the simulated dynamical results being compared to experimental findings obtained from Quasi-Elastic Neutron Scattering (QENS) measurements performed at the Science and Technology Facility Council's ISIS Facility.

With SCARF support we have been able to extend our investigation of the structural and dynamical behaviour of proteins in the amorphous state at low hydration. The systems chosen for study were the iron storage protein, apoferritin, the hen egg-white protein, lysosyme, and the enzyme, insulin. Via simulation we have been able to obtain the simulated effect of temperature and hydration on the structural features of these three representative bio-molecules, focusing particularly on the predicted changes in secondary structure and the radial distribution of water molecules in the hydration shell. Taking advantage of existing Quasi-Elastic Neutron Scattering (QENS) results, we have also compared the experimental and simulated temperature dependence of the mean squared displacement (MSD) parameter; the latter being obtained directly from analysis of our simulated molecular dynamics trajectories.

Theoretical models have been used to describe the resulting experimental and simulated spatial, or momentum transfer (Q), dependence of the incoherent neutron scattering dynamic structure factor. Simulated and experimental MSD values for all three dry proteins are in satisfactory agreement and, in the temperature interval of 10-290 K, the expected transition from harmonic to an-harmonic behaviour was detected.

Our preliminary findings, reported as "Probing Structure and Mobility of Proteins in the Amorphous State at Low Hydration", have been presented at both the Italian Neutron Scattering Conference 2018 (4-6 July 2018, Parma, Italy) and at the Institute Laue Langevin & European Spallation Source User Meeting (10-12 Oct 2018), Grenoble, France.

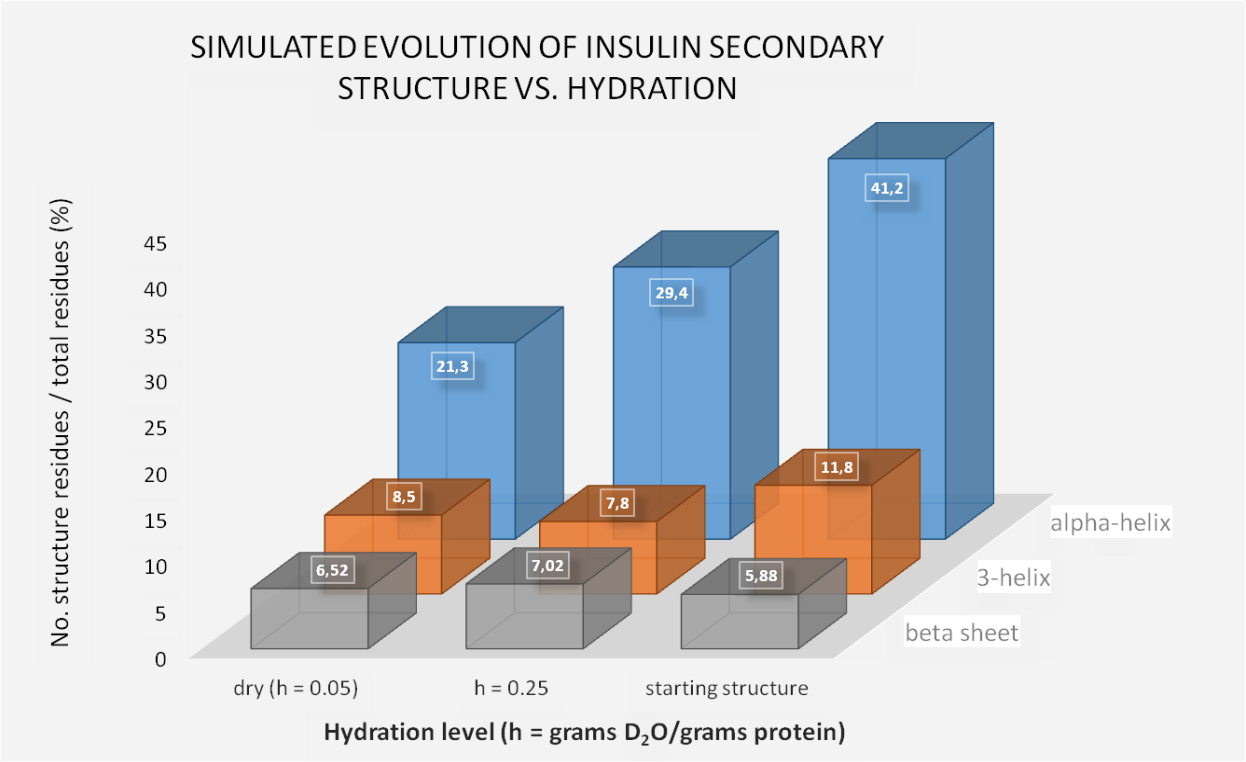

Figure 13: Evolution of the secondary structure of amorphous insulin as a function of hydration as simulated using SCARF and the Italian CINECA network.

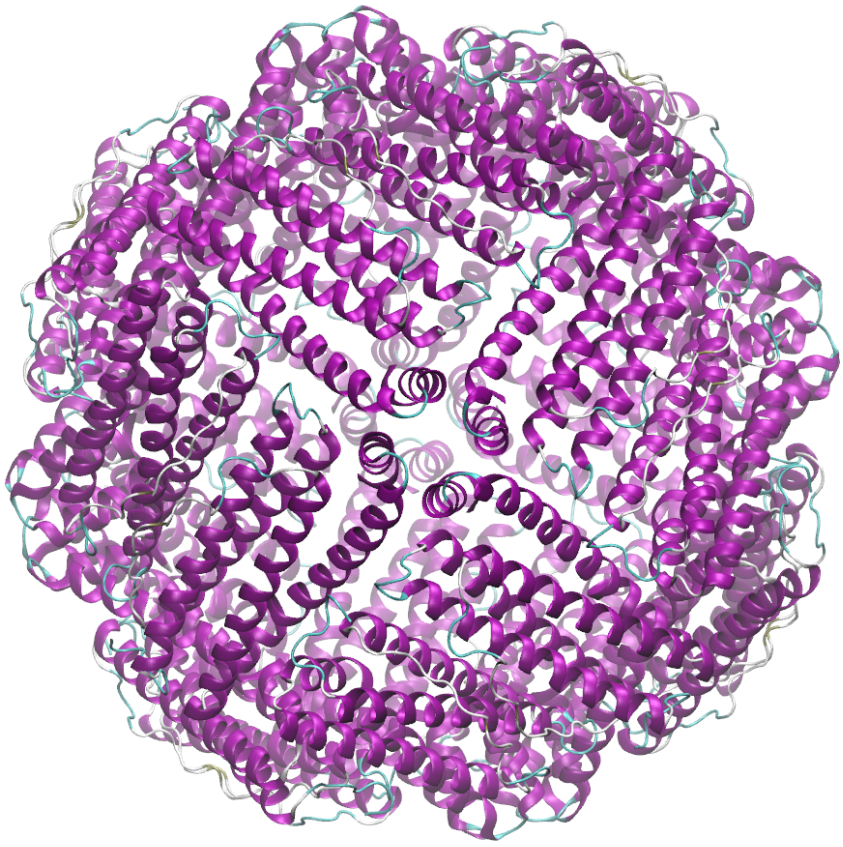

Figure 14: Crystal structure of apoferritin

Optimising Ion Source Extraction Optics for the ISIS Accelerator

Scott Lawrie

ISIS Low Energy Beams Group

ISIS is a world-leading centre for materials studies using neutrons and muons. It uses a high power synchrotron particle accelerator to smash protons into two solid tungsten targets. To generate high neutron flux at the targets, negative hydrogen (H^-) ions are injected into the synchrotron and then converted into protons. A new H^- ion source is being developed by the ISIS Low Energy Beams Group to replace the venerable Soviet-era technology used ever since ISIS began in the 1980s. A critical component of the new ion source is the extraction system, where particles are sucked out of a plasma and formed into a usable ion beam. As well as the desirable H^- ions, copious electrons are extracted, which need to be removed and their energy dumped safely. The IBSimu extraction modelling code is used to design the extraction system by solving Poisson equation self-consistently on a regular finite-difference mesh. The necessity to dump electrons means fully-3D simulations need to be performed, which increases vastly the number of mesh cells and time to converge on a solution.

Previous IBSimu modelling has been done on a desktop PC, whereby simulation geometry changes have been implemented in a loop. In this case, one simulation program solves different geometries sequentially one after another, which takes a long time. Recently, IBSimu has been installed on SCARF and a batch submission script written to loop through different geometry parameters and pass each parameter to a different simulation. In this manner, dozens of simulations can be run in parallel, rather than sequentially. In addition, SCARF nodes have more processing cores and memory than a desktop PC, so each simulation can be completed in higher detail on a finer mesh. SCARF has thus increased productivity many-fold, reducing the time to complete a parameter sweep from days to minutes.

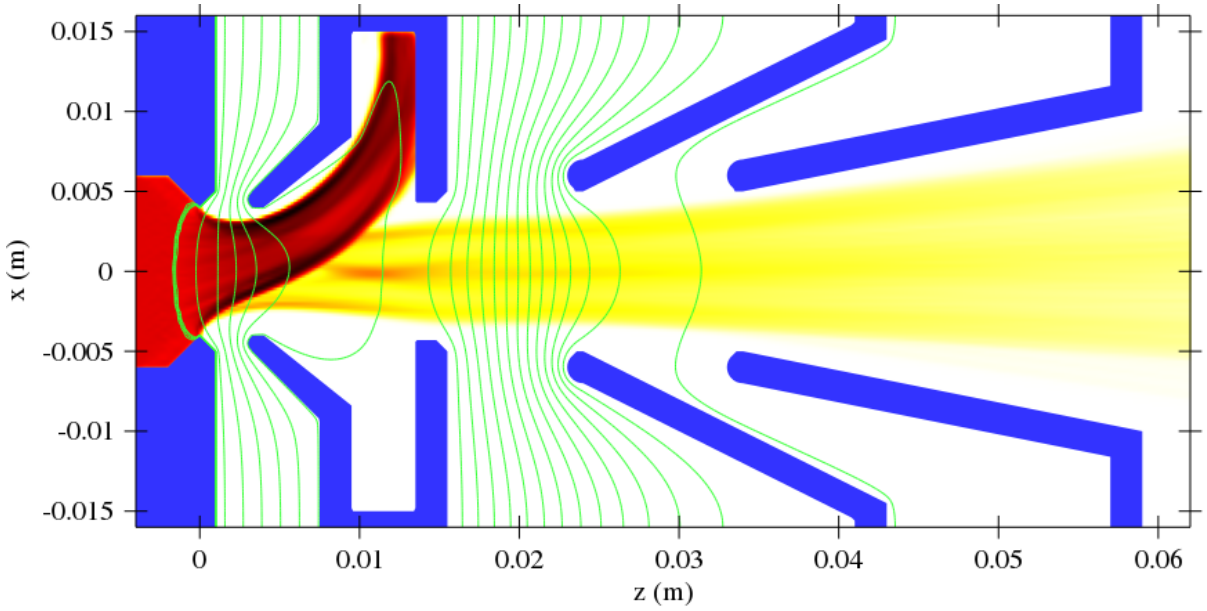

Figure 15: Particle tracking solution of the ion source extraction system. Metal electrode geometry (blue) sets up voltage contours (green) which accelerate and focus the H^- beam (yellow) and electrons (red) travelling from left to right. Deflection magnets sweep the electrons away into a dump, whereas the H^- beam travels on to the next accelerator section. SCARF enabled the concave green plasma boundary around z = 0 to be resolved extremely finely, which is important for precise predictions of beam behaviour.

Presented at the 6th International Symposium on Negative ions, Beams and Sources, Budker, Russia, September 2018. Due to be published in AIP Conference Proceedings.

Influence of Charge Transfer on the Isomerisation of Stilbene Derivatives for Application in Cancer Therapy

Nicole Holzmann[1], Leonardo Bernasconi[1], Roger H. Bisby[2], Anthony W. Parker[1]

1. *STFC Rutherford Appleton Laboratory, Harwell Oxford, Didcot, UK*
2. *School of Environment and Life Sciences, University of Salford, Salford, UK*

First isolated in 1982 from bark of African bush willow by Pettit[1], combretastatins are promising anti-cancer drugs targeting microtubule assembly. While the naturally occurring *cis* (Z-) isomers of those stilbene-based compounds show high cytotoxicity, their *trans* (E-) analogues are considerably less toxic. Photoisomerisation from the *trans* to the *cis* isomers can be achieved by both one- and two-photon excitation, the latter enabling the use of tissue penetrating wavelengths in the red or near-infrared region[2].

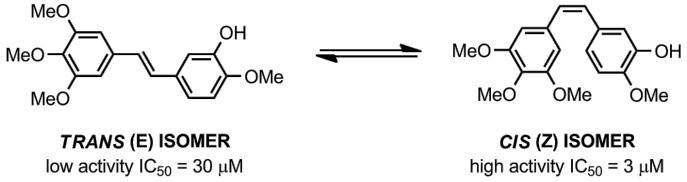

Figure 16: Light induced *trans-cis* isomerisation in combretastatins

In our previous work on the spectroscopic properties of trans isomers[3], we were able to confirm experimental results showing that a redshift of absorption wavelengths in stilbene derivatives occurs when the functional groups on the two opposing phenyl rings are substituted with electron pushing and electron pulling substituents on either side, introducing a charge transfer along the molecule[4]. This is of great importance for the application of these compounds as anti-cancer drugs, because higher absorption wavelengths facilitate tissue penetration of the irradiated light, which promotes the generation of the active form of the drug in situ.

More recently, we tackled another issue vital for the applicability of combretastatins and other stilbene derivatives in local cancer therapy: the isomerisation coordinate (IC)[5]. The IC provides a representation of the relaxation of all atoms in the molecule induced by the absorption of light, which is responsible for the trans-cis conversion. It is important that any alteration of trans combretastatins that, on one hand, improves the tissue penetration of the excitation wavelength does not, on the other hand, deteriorate the isomerisation to the cis isomers.

We used density-functional theory (DFT) and time-dependent density-functional theory (TD-DFT) calculations to study the interaction of (laser) light with substituted combretastatin molecules. According to the test set used in our previous work[3], we considered two combretastatins with low (non-CT1 and non-CT2) and two with high (CT1 and CT2) charge transfer character (Figure 17, left) for our computational study. The isomerisation occurs after electronic excitation of the *trans* isomers, where one of the HOMO (highest occupied molecular orbital) electrons is excited to the LUMO (lowest unoccupied molecular orbital, Figure 17, middle for CT1). This process decreases the double bond character of the internal C=C bond, which is then prone to rotate to give the *cis* isomer.

On SCARF, we performed a series of single-point DFT energy calculations scanning the C=C dihedral angle coordinate using NWChem6.6[6]. For the respective energies on the excited state (S_1) energy surface, the TD-DFT method was applied considering the 50 lowest excited states. For the overall scan (Figure 17, right, top) with a step size of 10˚, the optimised ground state *cis* structure was selected as reference point as both phenyl rings

deviate most from a planar arrangement, leading to reduced sterical hindrance, while the shallow energetic profile of the phenyl rotation[7] does not influence the overall energies significantly. A more accurate scan with a step size of 5˚ and with the optimised *cis* and *trans* excited state structures as reference points was carried out for the isomerisation region (Figure 17, right, bottom).

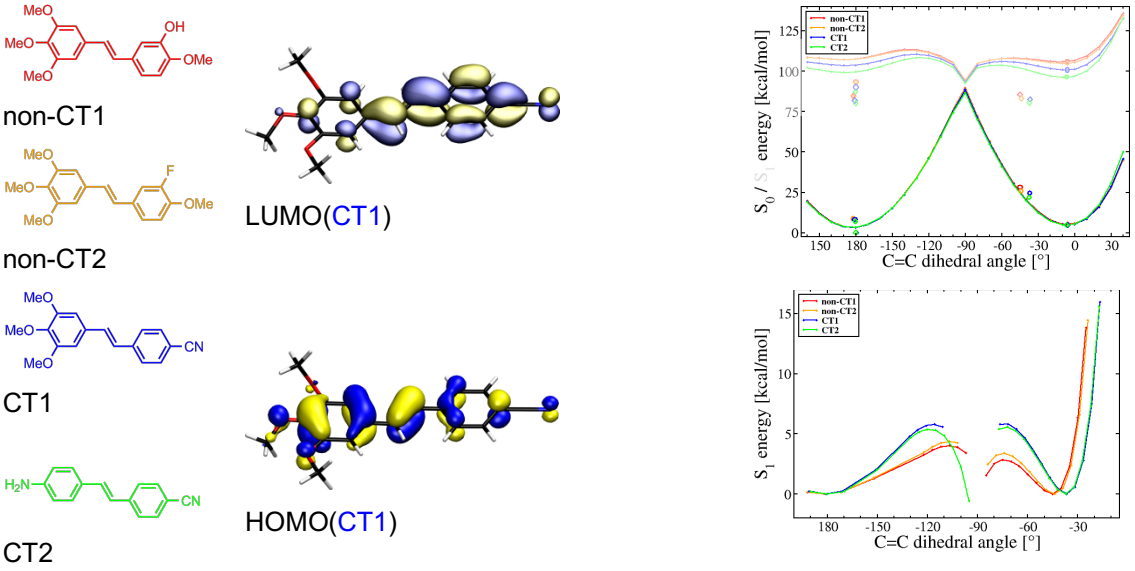

Figure 17: Stilbene derivatives with different charge transfer character (left), frontier orbitals of CT1 (middle), and calculated isomerisation coordinates for the ground state and the first excited state (right)

Our results illustrate that the isomerisation coordinate is essentially the same for all molecules in their ground state, while we observe a consequent reduction of the relative energies of the S_1 PES with increasing charge-transfer character. Barrier heights on the S_1 surface suggest that the *trans→cis* isomerisation is slightly favoured in non-charge transfer derivatives. The *cis→trans* isomerisation barriers for the charge-transfer compounds are of similar height as for the respective *trans→cis* isomerisation, which indicates that an even stronger charge-transfer character could reverse the unfavourable *trans→cis/cis→trans* barrier ratio. Furthermore, we have shown that the location of the conical intersection along the double bond rotation coordinate (i.e. the point along the IC at which the energies of the ground state and the first excited state are equal) is not affected by the charge-transfer character within the molecule. This suggests that, as for unsubstituted stilbene, the *cis/trans* product ratio is not influenced by the presence of charge-transfer substituents. Also, our analysis of the partial charges on individual atoms during the excitation suggests that different phenyl ring substitution patterns with electron accepting substituents on both sides of the molecule are likely to facilitate the isomerisation process. Our study has shown that the chemical modification of combretastatins and other stilbene derivatives provides a potentially very important route toward the development of new drugs for local cancer therapy.

References:

[1] G. R. Pettit, G. M. Cragg, D. L. Herald, J. M. Schmidt, P. Lohavanijaya, *Can. J. Chem.* 60, 1374 (1982).
[2] K. M. Scherer, R. H. Bisby, S. W. Botchway, J. A. Hadfield, A. W. Parker, *J. Biomed. Opt.* 20, 051004 (2015).
[3] N. Holzmann, L. Bernasconi, K. M. Callaghan, R. H. Bisby, A. W. Parker, *Chem. Phys. Lett.* 692, 146 (2018).
[4] K. M. Scherer, R. H. Bisby, S. W. Botchway, G. M. Greetham, J. A. Hadfield, A. W. Parker, M. Towrie, *Biomed. Spectrosc. Imagin*, 3, 211 (2014).

[5] N. Holzmann, L. Bernasconi, R. H. Bisby, A. W. Parker, *Phys. Chem. Chem. Phys*., in print.
[6] M. Valiev, E. J. Bylaska, N. Govind, K. Kowalski, T. P. Straatsma, H. J. Van Dam et al., *Comp. Phys. Commun.* 181, 1477 (2010).
[7] a) C. Jiang, R. Xie, F. Li, R.E. Allen, *Chem. Phys. Lett.* 474, 263 (2009). b) R. K. Chaudhuri, K. F. Freed, S. Chattopadhyay, U. S. Mahapatra, *J. Phys. Chem. A* 117, 9424 (2013).

Computational study on the absorption of Hg and Hg(II) by S bearing thiols

J. Rojas, C. Pinilla, A. Elena and N. L. Allan

In order to understand the absorption of Hg by thiols we have performed computing simulations within the density functional theory (DFT). We have devoted this study to understand the energetics related to the intermolecular interaction between Hg and different thiol molecules in order to understand the favourability of this process in an aqueous environment. We have performed studies in vacuum and well as in an aqueous environment to identify the most stable structures. Among the thiols molecules studied are Cisteíne $C_3H_7NO_2S$ **1**, 3-mercapto-3-metilbutan-1-ol $C_5H_{12}OS$ **2**, Silanol $C_3H_{10}O_3SSi$ **3** y Dimercaprol $C_3H_8OS_2$ **4** (figure 18).

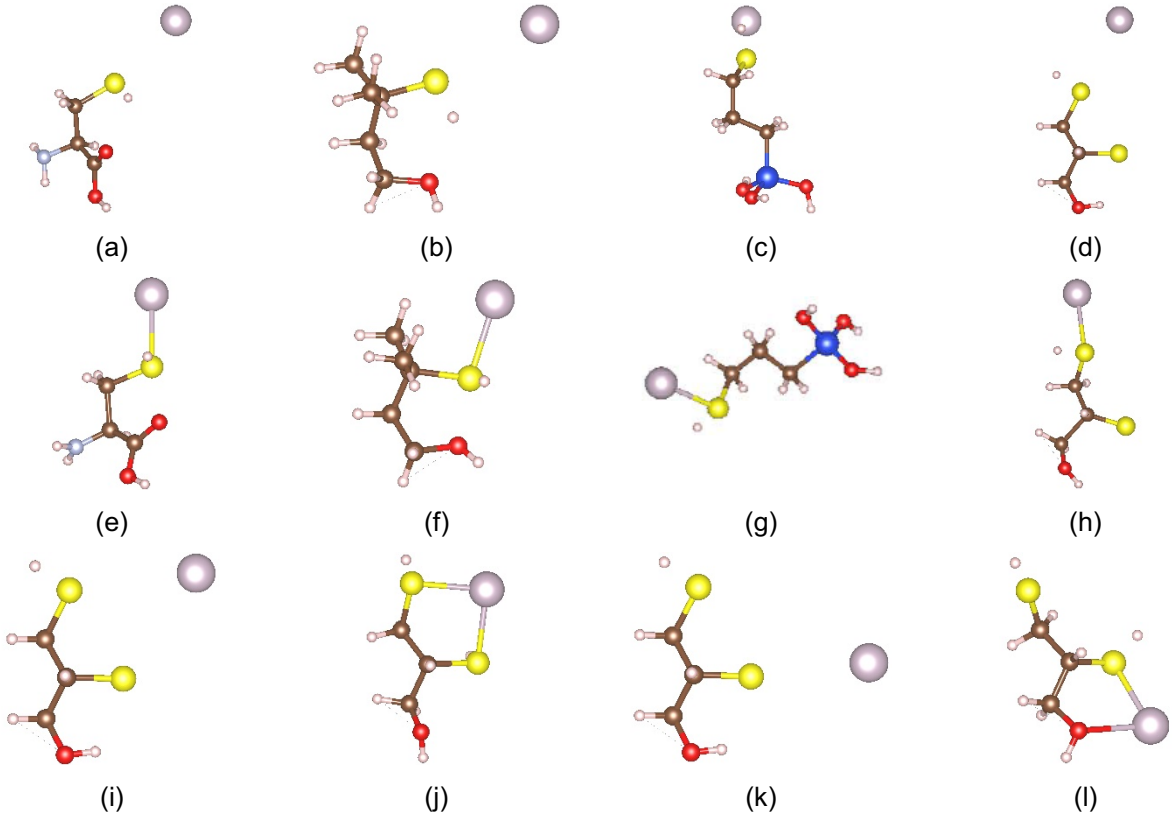

Figure 18: Final structure after relaxation for the interaction of Hg0, Hg+2–CYS 1 (a, e), C5H12OS 2 (b, f), silanol 3 (c, g) y BAL 4 (d, h, i, j, k, l) in vacuum.

A QM/MM study on Nitrite Binding in *Rp*NiR, a Three-Domain Copper Nitrite Reductase

Kakali Sen[1,2], Michael A. Hough[1], Richard W. Strange[1], Chin W. Yong[2], Thomas W. Keal[2]

1. *School of Biological Sciences, University of Essex, Wivenhoe Park, Colchester, Essex, UK*
2. *Scientific Computing Department, STFC Daresbury Laboratory, Warrington, Cheshire, UK*

Microbial copper-containing nitrite reductases (CuNiRs) are enzymes that catalyse the reduction of NO_2^- to NO, a key denitrification step in the global nitrogen cycle. This process involves a proton-coupled electron transfer reaction involving an electron donating T1Cu site and a catalytic T2Cu site. In two-domain CuNiRs, the electron is acquired from an external protein partner. The recently characterised *Rastonia picketti* (*Rp*NiR) system is a three-domain CuNiR, where the cupredoxin domain is tethered to a heme *c* domain that can function as the electron donor. The nitrite reduction starts with the binding of NO_2^- to the T2Cu, but very little is known about how NO_2^- binds to native *Rp*NiR. The structure of native *Rp*NiR [1] reveals it to be trimeric with high structural similarity to two-domain CuNiRs (Figure 19a,b). The linker that tethers the heme *c* domain to the cupredoxin domain is poised such that the sidechain of Tyr323 residue resides close to the T2Cu, potentially blocking the substrate access channel (Figure 19c).

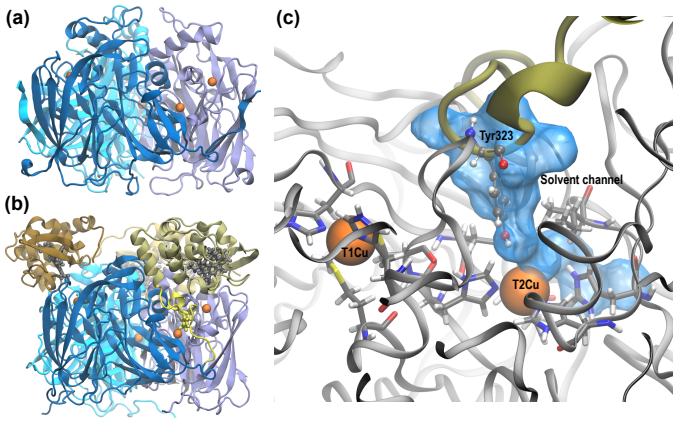

Figure 19: a) *Ac*NiR, a two-domain CuNiR from *Achromobacter cycloclastes*; PDB ID: 2BW4 and b) *Rp*NiR, PDB ID: 3ZIY. The Cu atoms are shown in orange and the heme units of the cytochrome domain are in black. c) Structural overlap of *Ac*NiR and *Rp*NiR. The backbone and active site residues from *Ac*NiR are shown for clarity. Tyr232 from the cytochrome domain of *Rp*NiR that blocks the otherwise solvent/ligand access channel is shown.

Until now no direct structural information of the binding mode of NO_2^- in native *Rp*NiR is available, though a recent crystallographic study of an *Rp*NiR active site mutant (D97N) [2] suggests that NO_2^- may bind via nitrogen rather than through the bidentate oxygen mode typically observed in two-domain CuNiRs [3]. The mode of nitrite binding is significant for the catalytic mechanism in CuNiRs and binding via either O or N of the nitrite to either Cu(I) or Cu(II) states is possible.

MD simulations reveal that Tyr323 does not rigidly block the substrate access channel to the active site but can be displaced by natural water dynamics in the resting state of the enzyme, causing the channel to open and allow NO or NO_2^- to enter or leave the catalytic site. This corroborates the structure of the D97N mutant [2], where similar displacement of Tyr323 was observed.

QM/MM optimization of MD snapshots revealed different modes by which NO_2^- can bind to the T2Cu. These are clustered into bidentate top-hat, monodentate top-hat, L-shaped N-bound and symmetric N-bound geometries of the nitrite. On energetic grounds, in the oxidized Cu(II) state the relative stabilities of the N-bound and top-hat states is not clear cut. However, for the reduced Cu(I) state there is a slight preference for the N-bound state in both native and mutant systems.

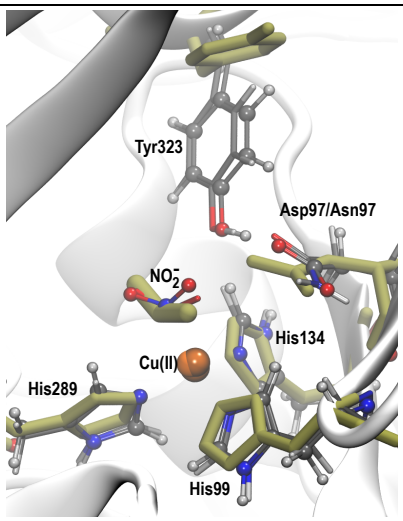

Figure 20: Superposition of the NO2- bound X-ray structure of D97N RpNiR (olive sticks) and two l-shaped N-bound conformers, obtained by simulations from an initially N-bound NO2- to the Cu(II) state in the native and D97N mutant systems.

Figure 20 shows the overlay of the X-ray structures of the nitrite-bound D97N mutant and two simulated conformers from the native and D97N mutant systems, with similar L-shaped NO_2^- orientations bound to Cu(II). In simulations, the Tyr323 was oriented in the substrate access channel as in the native *Rp*NiR crystal structure, rather than being displaced as observed experimentally for D97N. Apart from the difference in the Tyr323 position, the orientation of NO_2^- and the active site residues are all structurally similar to the observed X-ray structure. Our findings indicate that the X-ray structure is consistent with the L-shaped N-bound NO_2^- orientations for the Cu(II) state in *Rp*NiR and not the reduced Cu(I) state. Such an L-shaped orientation is not the one primarily observed in structures of two-domain CuNiRs in the Cu(II) state, where a bidentate top-hat orientation of NO_2^- is mostly prevalent instead.

Several of these calculations were carried out using SCARF computational facilities.

References:

[1] Antonyuk, S.V.; Han, C.; Eady, R.R.; Hasnain, S.S. *Nature* **2013**, *496*, 123.
[2] Dong, J.; Sasaki, D.; Eady, R.R.; Antonyuk, S.V.; Hasnain, S.S. *IUCrJ* **2018**, *5*, 510.
[3] Horrell, S.; Kekilli, D.; Sen, K.; Owen, R.L.; Dworkowski, F.S.N.; Antonyuk, S.V.; Keal, T.W.; Yong, C.W.; Eady, R.R.; Hasnain, S.S.; S.S.; Strange R. W.; Hough, M. A. *IUCrJ* **2018**, *5*, 283.

Determining neutron cross sections for couple calculations of molten salt fast reactors.

Gregory Cartland-Glover[1], Dzianis Litskevich[2], Stefano Rolfo[1], Alex Skillen[1], David Emerson[1], Bruno Merk[2] and Charles Moulinec[1]

1. *SCD, STFC, Daresbury Laboratory, SciTech Daresbury, Warrington, UK.*
2. *School of Engineering, Department of Mechanical, Materials and Aerospace Engineering, University of Liverpool, Liverpool.*

A coupled neutronics and thermal fluid dynamics project investigated the behaviour of molten salt fast reactors. Our interest was to examine the feasibility of the application of frozen salt films situated onto the reactor vessel walls. Molten salt fast reactors (MSFR) are one of six Gen-IV nuclear reactor concepts (https://www.gen-4.org). The aim of Gen-IV reactors is to increase operational safety and improve the economic and environmental sustainability of nuclear power. In the MSFR concept considered here the nuclear fuel is dissolved in the molten salt and it can move freely within the reactor and the primary heat exchange circuit. The MSFR is operated at atmospheric pressure and high temperature. Both the lack of reactor internals (solid fuel elements) and atmospheric pressure can reduce the costs of the reactor construction and operation. The fuel used was natural uranium, which we used to represent spent nuclear fuel. Plutonium that has been separated from (SNF) was added to the fuel mix to provide enough fissile material sustain a nuclear chain reaction.

To test the feasibility of frozen salt films in a molten salt fast reactor, the neutronics and thermal fluid dynamics were modelled in a staggered explicit coupled approach (Multiscale Universal Interface - https://github.com/MxUI; Yu-Hang Tang *et al.* 2015). The neutronics were modelled in a nodal neutron diffusion solver called DYN3D-MG (https://www.hzdr.de/db/Cms?pOid=11771&pNid=542; Kliem *et al.* 2016; Rohde *et al.* 2016), and the thermal fluid dynamics in the computational dynamic solver *Code_Saturne* (https://www.code-saturne.org/cms/; Archambeau *et al.* 2004; Fournier *et al.* 2011). A temperature dependent porosity was implemented in *Code_Saturne* to capture the freezing of the salt near to a cold surface (Figure 21).

The coupled calculations were performed on the CIRRUS (http://www.cirrus.ac.uk/) of the Edinburgh Parallel Computing Centre and NEALE and SCAFELL PIKE clusters (http://community.hartree.stfc.ac.uk/wiki/site/admin/resources.html) of the Hartree Centre. However, in order to perform these simulations, the neutronic behaviour of the MSFR must be characterised. In the method used in the feasibility study, the Monte Carlo neutron transport code, Serpent (http://montecarlo.vtt.fi/) was used to model the neutron statistics in the core of the molten salt fast reactor. The calculations were performed on SCARF to prepare multi-group neutron cross-sections (Figure 22), which characterise the reaction, leakage and scattering of the neutrons across a range of operating temperatures in the steady mode. The neutron cross-sections were then used in the DYN3D-MG model of the molten salt fast reactor. Serpent also allowed us to determine the ratio of uranium to plutonium, which could sustain a nuclear chain reaction at the specified inlet reactor inlet temperature (Figure 23) and how the steady mode reactivity changed with the temperature and density of the molten salt in the reactor (Figure 24).

References:

[1] F. Archambeau, N., Mechitoua, M., Sakiz. "*Code_Saturne*: a finite volume code for the computation of turbulent incompressible flows - Industrial Applications". *International Journal on Finite Volumes*, 1, 1-62, (2004).

[2] Y. Fournier, J. Bonelle, C. Moulinec, Z. Shang, A. Sunderland, J. Uribe, 2011. "Optimizing *Code_Saturne* computations on Petascale systems". *Computers and Fluids*, 45, 103–108 (2011).

[3] S. Kliem, Y. Bilodid, E. Fridman, S. Baier, A. Grahn, A. Gommlich, E. Nikitin, U. Rohde. 2016. "The reactor dynamics code DYN3D". *Kerntechnik*, 81(2), 170–172 (2016).
[4] J. Leppänen, M. Pusa, T. Viitanen, V. Valtavirta, T. Kaltiaisenaho. "The Serpent Monte Carlo code: Status, development and applications in 2013". *Annals of Nuclear Energy*, 85, 142–150 (2013).
[5] U. Rohde, S. Kliem, U. Grundmann, S. Baier, Y. Bilodid, S. Duerigen, E. Fridman, A. Gommlich, A. Grahn, L. Holt, Y. Kozmenkov, S. Mitta. "The reactor dynamics code DYN3D – models, validation and applications". *Progress in Nuclear Energy*, 89, 170–190 (2016).
[6] H. Rouch, O. Geoffroy, P. Rubiolo, A. Laureau, M. Brovchenko, D. Heuer, E. Merle-Lucotte, 2014. "Preliminary thermalhydraulic core design of the Molten Salt Fast Reactor (MSFR)". *Annals of Nuclear Energy*, 64, 449–456 (2014).
[7] Yu-Hang Tang, Shuhei Kudo, Xin Bian, Zhen Li and G. E. Karniadakis. "Multiscale Universal Interface: A concurrent framework for coupling heterogeneous solvers". *Journal of Computational Physics*, 297, 13–31 (2015).

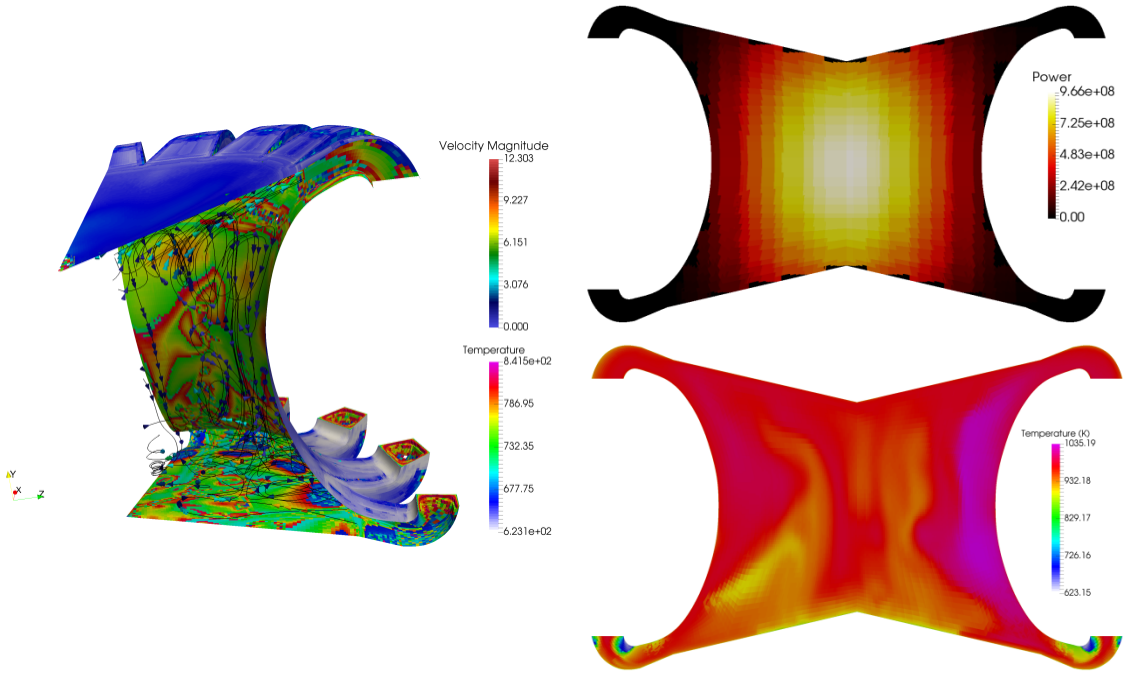

Figure 21: Contour and streamline plots of the thermal fluid dynamic and neutronic behaviour of a molten salt fast reactor operating with frozen wall technology, the calculations were performed on the CIRRUS and SCAFELL PIKE clusters. Left: Streamlines depicting the flow of fluid (velocity magnitude in m s^{-1}) in the reactor core and contour plots of temperature (K) on the surface of the frozen salt film. Right: Contour plots of the power (W) and the temperature (K) in the reactor core.

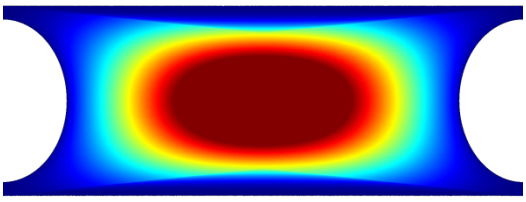

Figure 22: Mesh plot of the neutron population distribution in the core obtained by SERPENT on SCARF. 1.9 billion neutrons were used in creating this plot over 2000 transport cycles. Dark red: High neutron density; Blue: Low neutron density. 1 node of SCARF-17 took 24 hours to complete 2000 cycles.

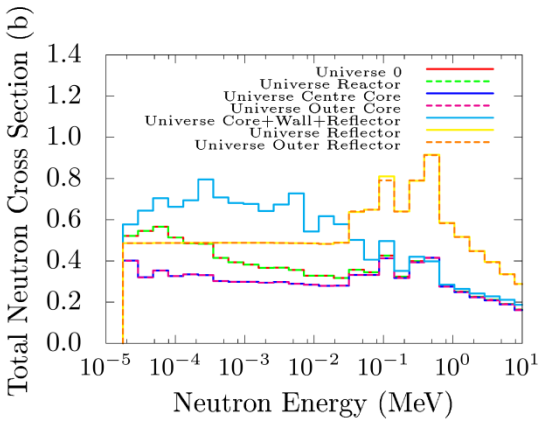

Figure 23: Plot of the total neutron cross section for different parts of the geometry modelled obtained by SERPENT on SCARF. The whole geometry (Universe 0), the reactor (Universe reactor) and sample regions in the reactor core and the reflector surrounding the core.

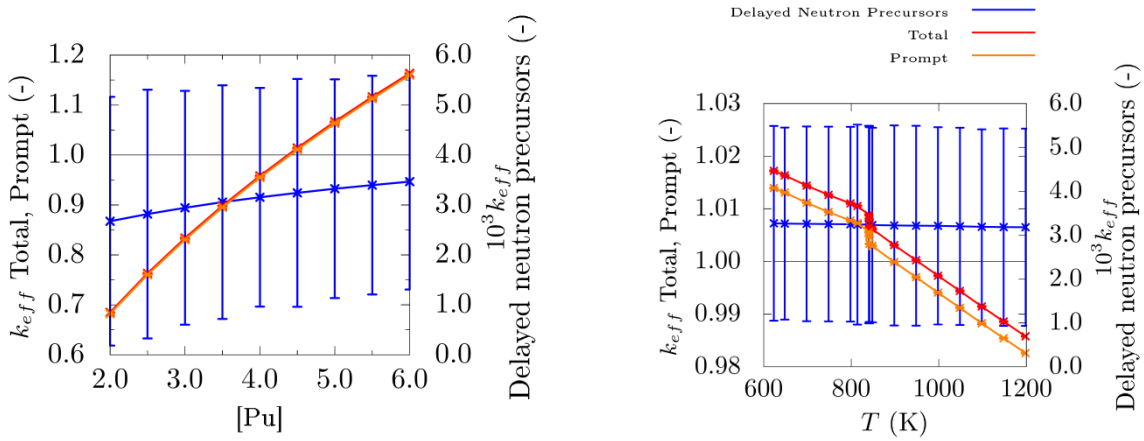

Figure 24: Plots of the steady state molten salt fast reactor, k_{eff}, the effective neutron multiplication factor which indicates whether a chain reaction can be sustained, which were obtained by SERPENT on SCARF. On the left is the variation of the reactivity with the concentration of plutonium at 898.15 K and on the right is the variation of the reactivity with temperature at a plutonium concentration of 4.4%. The assumed liquidus and solidus temperatures were 841.55 K and 814.22K, respectively. The step in k_{eff} on the right-hand plot occurs between these temperatures due to the change in density, as the state of the salt changes from liquid to solid.

Investigation of muon induced effects in Sr_2RuO_4 by DFT calculations

Ifeanyi John Onuorah, Pietro Bonfà, Roberto De Renzi

Dipartimento di Scienze Matematiche, Fisiche e informatiche, Università di Parma, Parco Area delle Scienze, Parma, Italy.

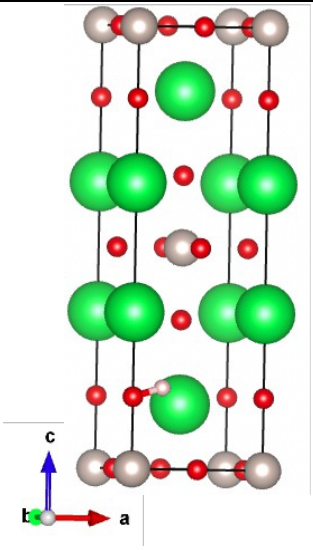

Figure 25: The Sr_2RuO_4 structure and muon (pink ball) site together with the bonds it makes with the O atom (red sphere)

We have continued to use the Density functional theory (DFT) based calculations to determine the muon implantation site(s) in lattices [1]. Calculations were run on the SCARF cluster with the DFT implementation in the Quantum Espresso code.

The muon implantation site together with the muon induced effects have been studied in Sr_2RuO_4. Sr_2RuO_4 is a layered superconductor, where in the mechanism that drives superconductivity, time reversal symmetry breaking has been observed by spontaneous magnetization measured with the muon spin spectroscopy (μSR) [2]. However, this particular effect has not been observed by other scanning probe methods. To understand the effect of the muon in the lattice, the muon site has been determined by DFT calculations. At the muon site, the muon bonds with the oxygen atom with bond distance of approximately 1 Å (Fig. 25). The study of the effect of the muon on the lattice has shown that only the host atoms in the vicinity of the muon site are displaced from their equilibrium positions. The displacement of the host atoms vanishes exponentially away from the muon site (Fig. 26). Further analyses of the effect of the muon on the density of states show no appreciable change due to the muon, even though the muon distorts the neighbour host ions from their equilibrium positions. Our calculations so far suggest that the implanted muon does not influence the intrinsic properties of Sr_2RuO_4. However, it is important to further understand the effect of spin-orbit coupling together with that of the muon on band splitting.

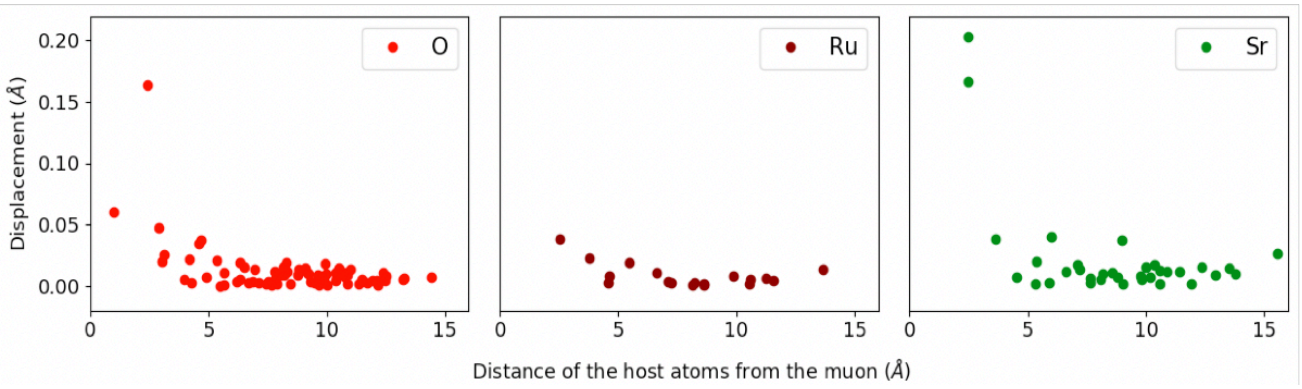

Figure 26: Displacement of the O, Ru and Sr atoms from their equilibrium position versus their distance from the implanted muon.

Also, for the study of the effects of the muon zero point motion with the stochastic self-consistent harmonic approximation [3], DFT has been used for force calculations of the supercells containing randomly displaced muon from their equilibrium position.

References:

[1] P. Bonfà and R. De Renzi, J. Phys. Soc. Jpn. 85, 091014 (2016).
[2] G. M Luke, et.al Nature 394, 558{561 (1998).
[3] I. Errea et. al Phys. Rev. Lett. 111, 177002 (2013).

A Plasma Undulator using Laser-Driven Parabolic Plasma Channel

Oznur Apsimon[1], Daniel Seipt[2], Yong Ma[2], Guoxing Xia[1] and Alec Thomas[2]

1. *The University of Manchester*
2. *Michigan University*

A plasma undulator is formed when a short laser pulse is injected into a parabolic plasma channel off-axis or at an angle that causes the centroid of this laser pulse to oscillate (Rykovanov et al., 2015; Apsimon et al., 2017). Ponderomotively driven plasma wake will follow this centroid given that the product of the plasma wave number and the characteristic Rayleigh length of the laser is much larger than one. This oscillating transverse wakefield works as an undulator (wiggler) forcing particles to follow sinusoidal trajectories and emit synchrotron radiation. Theoretically, a plasma undulator can generate order of magnitude larger effective magnetic fields than conventional undulators.

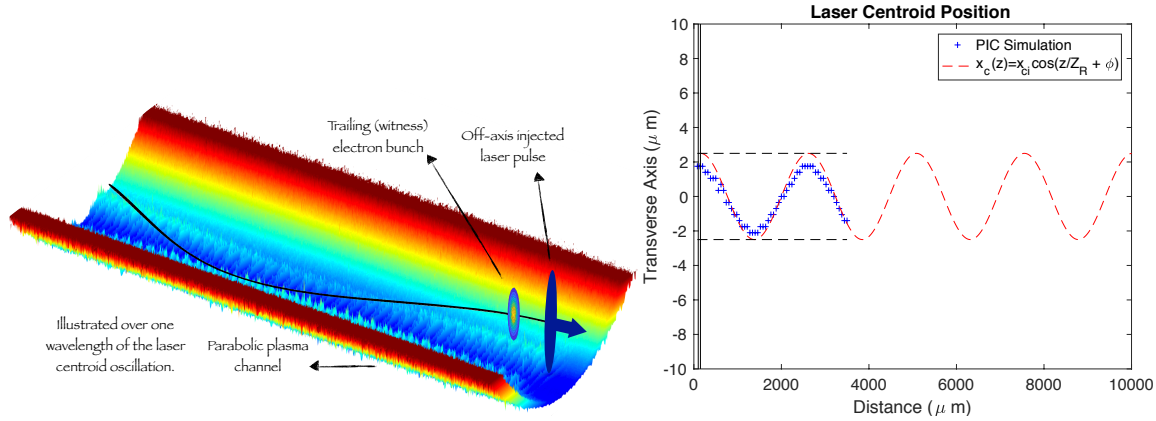

Figure 27: Left: Illustration of the propagation of a matched laser pulse in a parabolic plasma channel injected with an offset with respect to the channel centre. The laser is followed by a witness electron bunch. Right: Predicted laser centroid oscillation simulated by EPOCH on SCARF.

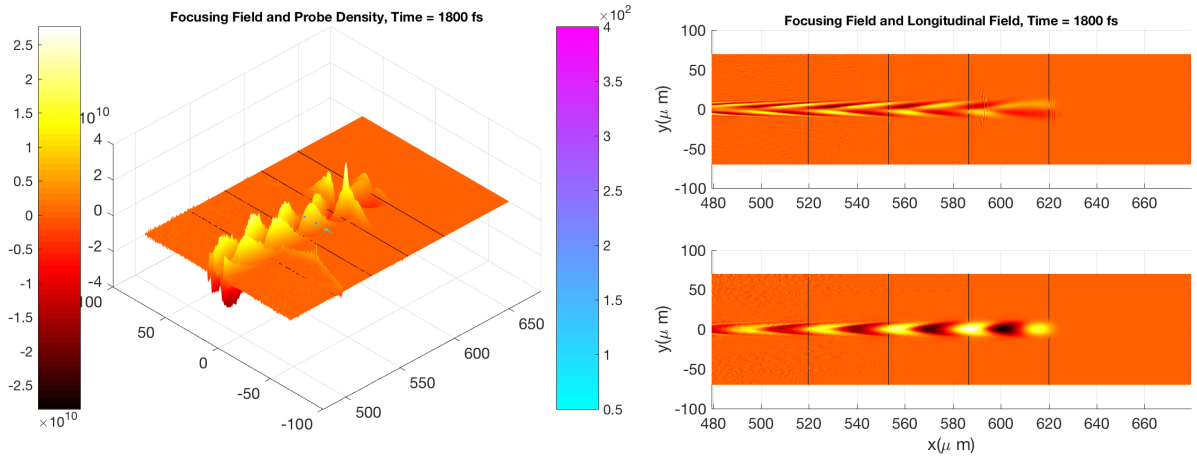

Figure 28: Focusing force induced by plasma wakefields and probe bunch density, and b) focusing and accelerating components of the plasma wakefields simulated with EPOCH on SCARF.

For the preliminary studies, a plasma with a density of $1\times10^{24}m^{-3}$ was driven by an 800nm laser pulse with an a_0 of 0.8. A parabolic plasma width of 9.41µm was analytically obtained (Rykovanov et al., 2016) for the laser spot size of 10 mum and implemented in the simulations. Studies are ongoing to optimise the shape of the field regions and the injection phase of the probe particles.

References:

[1] S. G. Rykovanov et al., Plasma undulator based on laser excitation of wakefields in a plasma channel, PRL 114, 145003 (2015).
[2] O. Apsimon et al., Design study for a plasma undulator experiment using capillary-based discharge plasma source, Pro- ceedings of International Particle Accelerators Conference, 1584-1586 (2017).
[3] S. G. Rykovanov et al., Tunable polarization plasma channel undulator for narrow bandwidth photon emission, Phys. Rev. AB 19, 090703 (2016).

INS sheds light upon PEF's superior barrier properties – a comparison with PET

Catarina F. Araujo[1], Mariela M. Nolasco[1], Paulo J. A. Ribeiro-Claro[1], Svemir Rudić[2], Armando J. D. Silvestre[1], Pedro D. Vaz[1,2], Andreia F. Sousa[1,3]

1. *CICECO − Aveiro Institute of Materials, Departamento de Química, Universidade de Aveiro, Aveiro, Portugal*
2. *ISIS Neutron & Muon Source, STFC Rutherford Appleton Laboratory, Chilton, Didcot, Oxfordshire, U.K.*
3. *CEMMPRE, Department of Chemical Engineering, University of Coimbra, Coimbra, Portugal*

Polyethylene furanoate (PEF) is a polyester easily prepared from sugars and often marketed as the sustainable alternative to PET. Besides its lower carbon footprint, PEF shows mechanical and thermal properties which are comparable to polyethylene terephthalate (PET) while offering greatly improved barrier properties. Compared to PET, PEF is 10 times less permeable to oxygen and 20 times less permeable to carbon dioxide, a characteristic very attractive to the packaging industry. Indeed, Coca-Cola and Danone partnered with Synvina to develop an efficient PEF production process and PEF bottles are expected to launch in the near future.

Despite their contrasting gas barrier performance, PEF and PET are structurally similar, differing only on the ring moiety, a six-membered aromatic ring for PET and a five-membered furanic ring for PEF. Therefore, this pair is quite interesting for exploring how structure correlates with barrier performance, the first step towards the rational design of new polymers with tailor-made properties.

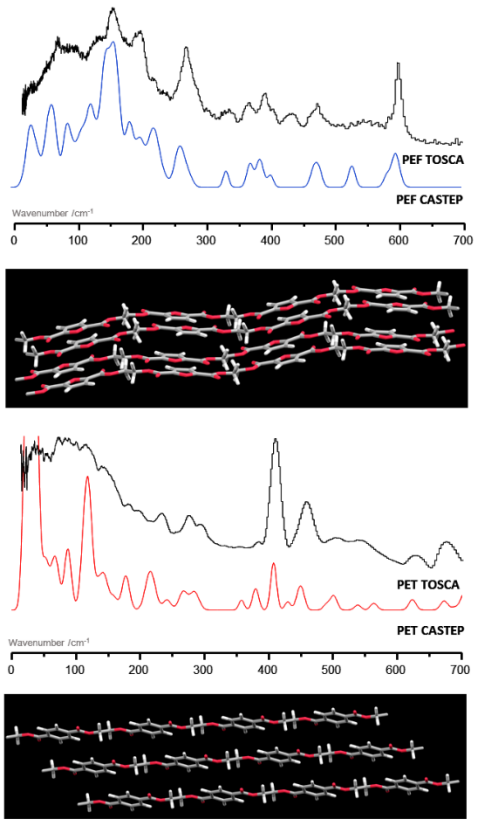

Figure 29: Experimental (TOSCA) and estimated (CASTEP) spectra of PEF (upper panel) and PET (lower panel) along with a 3D representation of their crystal structures.

Following this vision, researchers from CICECO – Aveiro Institute of Materials teamed up with Svemir Rudić, an instrument scientist at ISIS Neutron and Muon Source, to use Inelastic Neutron Scattering (INS) for the study of low frequency modes in PEF and PET. Vibrational assignments were performed with the aid of CASTEP calculations. The crystal structures of PEF and PET, reported in the literature, were used as starting points for geometry optimization followed by a phonon calculation to estimate INS intensities. All periodic calculations have been performed on the SCARF cluster.

The INS spectra of PEF and PET, collected on TOSCA, are shown in Fig. 29, along with INS spectra estimated using CASTEP. The correspondence among experimental and calculated spectra is very good, despite the fact that calculations were performed assuming perfect crystals, while the samples measured on TOSCA were semi-crystalline.

Vibrational analysis show that PEF's chains are less flexible than those of PET – and greater flexibility translates into increased permeability to gas penetration. For instance, the vibrational mode associated with aromatic ring flipping in PET is located at circa 116 cm^{-1} in the INS spectrum while the corresponding mode in PEF is found further upfield, at 160 cm^{-1}. This observation confirms previous NMR results [1] showing that PET's phenyl ring

behaves as a free rotor while in PEF the same motion is hindered. Likewise, a mode associated with the CH_2-CH_2 moiety ("seesaw" mode), is found at 200 cm^{-1} in the spectrum of PEF and 84 cm^{-1} downfield for PET, another marker of PEF's reduced chain flexibility. PEF's chain rigidity is due, in part, to an extensive network of C-H…O bonds which interlock adjacent chains (absent in PET) but also due to the intrinsic hardness conferred by the furanic ring, whose out-of-plane deformation gives rise to an intense mode at 602 cm^{-1} while the corresponding mode for PET's phenyl ring is found at 410 cm^{-1}.

The findings discussed above are presented in greater detail in a recent publication [2]. Further works on PEF analogues are expected to be published in the near future.

References

[1] "Chain Mobility, Thermal, and Mechanical Properties of Poly(ethylene furanoate) Compared to Poly(ethylene terephthalate)", Burgess, S. K.; Leisen, J. E.; Kraftschik, B. E.; Mubarak, C. R.; Kriegel, R. M.; Koros, W. J., *Macromolecules*, 47 (2014), 1383-1391, DOI: 10.1021/ma5000199

[2] "Inside PEF: Chain Conformation and Dynamics in Crystalline and Amorphous Domains", Araujo, C. F., Nolasco, M.M., Ribeiro-Claro, P. J. A., Rudić, S., Silvestre, A.J.D., Vaz, P. D., and Sousa, A. F., *Macromolecules*, 51 (2018) 3515–3526. DOI:10.1021/acs.macromol.8b00192

Exploring the hydrogen bond network of cellulose with Inelastic Neutron Scattering

C. Araujo[1], C. S. R. Freire[1], M. M. Nolasco[1], P. J. A. Ribeiro-Claro[1], S. Rudić[2], A. J. D. Silvestre[1], and P. D. Vaz[1,2]

1. *CICECO − Aveiro Institute of Materials, Department of Chemistry, University of Aveiro, Aveiro, Portugal*
2. *ISIS Neutron & Muon Source, Rutherford Appleton Laboratory, Chilton, Didcot, Oxfordshire, United Kingdom*

Cellulose, an ubiquitous naturally occurring polysaccharide, attracts attention from diverse research fields as a raw material for the development of novel, sustainable products – for example, as reinforcement in biobased composites. The physicochemical properties of cellulose based products greatly depend upon the supramolecular structure of cellulose fibres and there is a definite need for characterization tools able to assess structure-property relationships. Inelastic Neutron Scattering (INS) might be useful in this context, as this vibrational spectroscopy technique is very sensitive to the movement of hydrogen atoms – good for probing changes in the hydrogen bond network – and suited for the study of low frequency vibrations, which serve as a probe for the supramolecular architecture.

However, the few existing INS reports on cellulose date from the late 90's and early 00's and lack the high spectral quality attainable nowadays using optimized INS instruments, such as the new TOSCA. Therefore, the detection of very subtle spectral changes across different cellulose-based materials is now possible and the need for a definitive assignment of the raw material's INS spectrum became apparent. The INS spectra of cellulose samples from different sources (cotton, kraft pulp, bacterial cellulose) and varying water contents was collected on TOSCA.

Vibrational assignments were guided by literature reports and periodic CASTEP calculations performed on the SCARF cluster for the crystal structures of cellulose Iα and Iβ polymorphs. The agreement between collected and estimated spectra is very good, as illustrated in Fig. 30 where a section of the experimental spectrum of bacterial cellulose is compared with the estimated CASTEP spectra for the Iα and Iβ cellulose polymorphs. The full vibrational assignment is available in a recent paper [1], of which the most interesting results are summarized below:

CASTEP is very efficient in estimating the frequency and intensities of most fundamental modes, wings and overtones of cellulose, only failing for modes involving the OH moiety, a well-known shortcoming of the code.

INS is a viable tool for roughly assessing the degree of crystallinity – for instance, the contribution at 1282 cm^{-1}, arising from a cooperative C-H bending mode, is sharp and intense in the spectrum of bacterial cellulose (highly crystalline) but it decreases in intensity, merging into the broad profile underneath, as one moves from bacterial to cotton to kraft cellulose, reflecting their decreasing degree of crystallinity.

The spectrum of hydrated kraft cellulose, at 37 wt% water content, clearly indicates the formation of hexagonal ice resulting from the solidification of "free water", that is, water clusters fairly undisturbed by the surrounding cellulose chains. When the spectrum of Ice Ih is subtracted from that of hydrated kraft cellulose, the difference spectrum reveals modest changes associated with the presence of "bound water" – water molecules directly interacting with the surface of cellulose nanocrystals. The most significant change occurs at 910 cm^{-1}, a well-defined band in dry kraft cellulose which broadens and loses intensity in the spectrum of hydrated kraft cellulose. This contribution arises from methylene rocking, confirming the view that water preferentially interacts with the CH_2-OH moiety, leading to increased disorder of the hydroxymethyl group conformation at the cellulose surface.

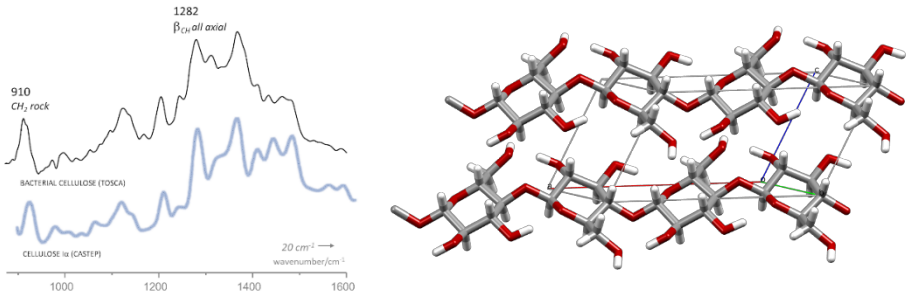

Figure 30: Left panel: Experimental spectrum (TOSCA) of bacterial cellulose compared with that estimated from cellulose Iα crystal structure. Right panel: 3D representation of the cellulose Iα crystal structure.

Following this study, researchers from CICECO recently performed INS measurements, on TOSCA, of cellulose based composites. The study of these complex systems will be greatly aided by the thorough vibrational assignment previously performed.

References:

[3] "Hydrogen Bond Dynamics of Cellulose through Inelastic Neutron Scattering Spectroscopy", Araujo, C.F., Freire, C.S.R., Nolasco, M.M., Ribeiro-Claro, P.J.A., Rudić, S., Silvestre, A.J.D., Vaz, P.D., *Biomacromolecules*, 19 (2018) 1305-1313, DOI: 10.1021/acs.biomac.8b00110

Neutron spectroscopy as a sensitive probe of cation···anion interactions in a deep eutectic solvent

C. F. Araujo,[1] J. A. P. Coutinho,[1] M. M. Nolasco,[1] S. F. Parker,[2] P. J. A. Ribeiro-Claro,[1] S. Rudić,[1] B. I. G. Soares[1] and P. D. Vaz [1,2]

1. *CICECO – Aveiro Institute of Materials, Departamento de Química, Universidade de Aveiro, 3810-193 Aveiro, Portugal*
2. *ISIS Neutron & Muon Source, STFC Rutherford Appleton Laboratory, Chilton, Didcot, UK*

Deep eutectic solvents (DES) are a novel class of designer solvents hailed as the sustainable alternative to ionic liquids. The most common type of DES are formed by mixing a salt, usually a quaternary ammonium halide, with an hydrogen bond donor, including amides, amines, alcohols and carboxylic acids. The term “deep eutectic” arises from an interesting phenomenon: the melting point of a deep eutectic mixture is significantly lower than that of an ideal mixture of its components. For instance, the iconic DES named “Reline” consists of a mixture of choline chloride (ChCl) and urea, whose ideal mixture would melt at 75ºC while the real mixture (1 ChCl: 2 urea) melts close to 20ºC. The difference between the ideal and real melting temperature is often called “melting point depression” and the mechanism behind this phenomenon is still poorly understood, although it is apparent that both enthalpic and entropic factors are involved. In order to better understand “Reline” it is useful to assess the hydrogen bond network and supramolecular architecture formed among the choline cation, chloride anion and urea within the eutectic mixture. For that purpose, researchers at CICECO – Aveiro Institute of Materials performed a thorough vibrational analysis of choline chloride, urea and “Reline” using infrared, Raman and Inelastic Neutron Scattering (INS) techniques. INS spectra were collected on TOSCA and their vibrational assignment was achieved with the aid of periodic CASTEP calculations, performed on the SCARF cluster. For the pure compounds, the starting geometry was derived from the crystal structures available at the CCDC. Since no crystal structure is available for the eutectic mixture (although it has been proved that, below the melting point, ChCl and urea do form a co-crystal), a hypothetical unit cell was built, based on the most stable of several DFT-optimized discrete clusters. Although the results were not brilliant the correspondence between experimental and estimated spectra was fair enough for the purpose of aiding the vibrational assignment of “Reline”.

Vibrational mode	Experimental frequency/cm^{-1}			Estimated frequency (CASTEP)/cm^{-1}		
	ChCl	Reline	Δ	ChCl	Reline	Δ
In-phase torsion, τ_1	286	252	−34	293	261	−32
Out-of-phase torsion, τ_2	341	296	−45	340	288	−52
Out-of-phase torsion, τ_3	349	333	−16	351	327	−24

Figure 31: Experimental and estimated frequencies of the methyl torsional modes in the pure choline chloride crystal and in Reline.

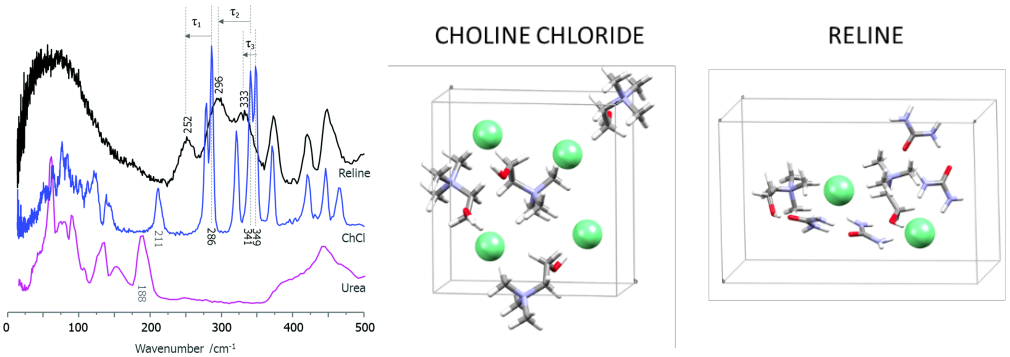

Figure 32: Left panel: Experimental spectrum of "Reline", choline chloride and urea (TOSCA). Right panel: 3D representation of the unit cells of choline chloride and Reline used for estimating vibrational spectra in CASTEP.

The most interesting aspect of the INS study, discussed in detail in the published paper [1], concerns the methyl torsional modes of the choline cation, which appear intense and well defined in INS spectra while being barely visible in infrared and Raman spectra. Methyl torsions in choline chloride are sensitive to their environment. As free volume around the cationic head increases the barrier to methyl group rotation decreases and so do the frequencies of their torsional modes, as seen for tetramethylammonium cations occluded within zeolite cages of increasing size. An increase in free volume around the cationic center is observed for the choline cation when going from the ChCl crystal to the eutectic mixture, as indicated by the red-shift of its methyl torsional modes, illustrated in Fig. 31 and Fig. 32.

Therefore, upon forming the eutectic mixture, chloride anions move away from choline's headgroup, likely due to forming competitive interactions with urea. This observation contradicts the old established notion that cation…anion interaction is disrupted at the -OH$\cdots Cl^-$ tail while confirming the results from Hammond [2], who used neutron diffraction to study Reline and observed that the OH$\cdots Cl^-$ distance, in the mixture, stays the same as in the ChCl crystal while the $CH_3\cdots Cl^-$ distance slightly increases.

Earlier this year the CICECO research team had another TOSCA mission, this time to study mixtures of urea with symmetric and asymmetric quaternary ammonium cations. The results are expected to be published in the near future.

References:

[1] "Inelastic neutron scattering study of reline: shedding light on the hydrogen bonding network of deep eutectic solvents"Araujo, C.F., Coutinho, J.A.P., Nolasco, M.M., Parker, S.F., Ribeiro-Claro, P.J.A., Rudić, S.,Soares, B.I.G., Vaz, P.D., *PCCP*, **19** (2017) 17998-18009, DOI: 10.1039/C7CP01286A

[2] "Liquid structure of the choline chloride-urea deep eutectic solvent (reline) from neutron diffraction and atomistic modelling", Hammond, O.S., Bowron, D.T. and Edler, K.J., *Green Chem.*, **18**, (2016), 2736-2744, DOI:10.1039/C7CP01286A

Understanding the Vibrational Spectra of Crystalline Isoniazid: Raman, IR and INS Spectroscopy and Solid-State DFT Study

Paulo J. A. Ribeiro-Claro[1], Pedro D. Vaz[1,2], Mariela M. Nolasco[1] and Ana M. Amado[3]

1. *CICECO, Departamento de Química, Universidade de Aveiro, Aveiro, Portugal.*
2. *ISIS Neutron & Muon Source, Rutherford Appleton Laboratory, Chilton, Didcot, Oxfordshire, UK*
3. *Química-Física Molecular, Departamento de Química, FCTUC, Universidade de Coimbra, Coimbra, Portugal.*

Isoniazid (pyridine-4-carbohydrazide, also known as isonicotinic acid hydrazide (scheme 1) is still one of the main drugs used in tuberculosis chemotherapy. Moreover, being a GRAS molecule (Generally Regarded As Safe), with ability to form to form sound associations with molecules bearing carboxylic acid groups [1], it is also particularly interesting in the expanding field of pharmaceutical co-crystals.

Isoniazid provides a clear example of the current status concerning the elucidation of the vibrational spectra of pharmaceutically active ingredients. Early assignments of isoniazid are frequently partial and often conflicting in several relevant points [2-5]. The more recent quantum chemical calculations [3-6] fail to select the most stable conformational form of the molecule or the correct hydrogen-bond contacts present in the crystal, leading to ill-based vibrational assignments. This situation precludes the full use of vibrational spectroscopy in the study of isoniazid systems and justifies a more comprehensive work. The vibrational properties of crystalline isoniazid have been fully described using a blend of spectroscopic techniques and computational methods. In combination with its optical counterparts (Raman and infrared spectroscopies), inelastic neutron scattering (INS) spectroscopy provides access to a detailed description of all the vibrational modes in the crystal. Periodic density functional calculations using CASTEP (Figure 33) were able to successfully reproduce the experimental spectra with a few exceptions. Discrete calculations, using G09, with a pairwise molecular approach, were used to circumvent the well-known problems of periodic calculations in the description of particular modes (e.g., carbonyl stretching and NH bending modes).

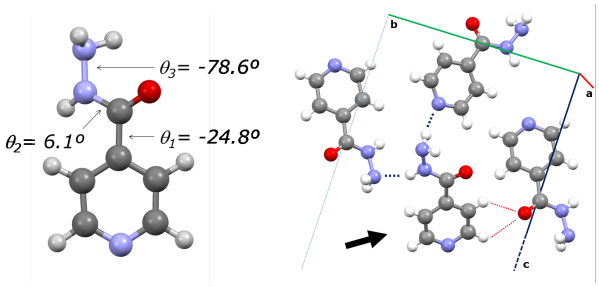

Figure 33: Optimized geometry of the isolated molecule (Gaussian09, left) and the crystalline structure (CASTEP, right). Torsional angles for the isolated molecule and relevant intermolecular contacts in the crystalline structure are shown (see text).

This combined approach was able to successfully reproduce the whole spectral range, allowing a sound assignment of the vibrational bands. Previous mis-assignments have been corrected and several spectral features of isoniazid crystal - such as the unusual combination of NH oscillators in the NH stretching region, the factor group splitting observed for large amplitude molecular vibrations, and detailed description of lattice modes region - are reported for the first time. In this way, this study contributed to further understand the structure of this API and to prevent the propagation of incorrect data analysis and mis-assignments.

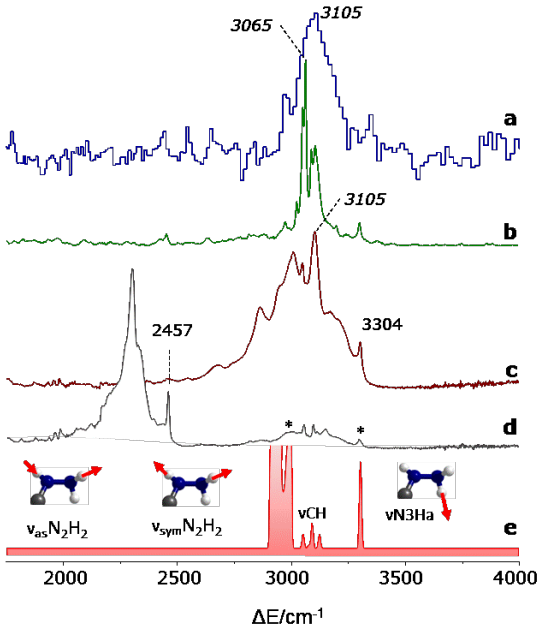

Figure 34: INS (a), Raman (b), and infrared (ATR, c) spectra of isoniazid, compared with the infrared spectrum of N-deuterated isoniazid (isoniazid-d_3, d) and the calculated infrared spectrum (CASTEP, e), including the visualization of atomic displacement vectors for the normal modes corresponding to the higher wavenumber band (right) and the two lower wavenumber bands (left). The asterisks (in line d) mark the bands from residual non-deuterated form. For the sake of clarity, the calculated bands at ca. 3000 cm-1, assigned to vN2H2 stretching modes, have been cut at about 5% of their intensity.

The success in describing isoniazid vibrational spectra was particularly relevant in view of the urgent need of reliable computational approaches to elucidate the vibrational properties of molecular crystals (Figure 35) namely, due to the rising importance of vibrational spectroscopy as a tool in pharmaceutical research technology.

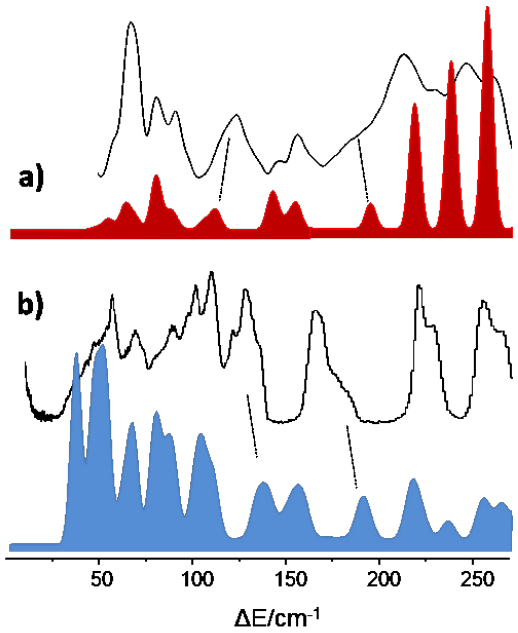

Figure 35: Experimental far-infrared spectrum (a) and inelastic neutron scattering spectrum (b) of isoniazid, compared with their CASTEP calculated (colored) versions, using the PBE functional. The dashed lines indicate the less obvious correspondences assumed.

The state-of-the-art solid-state density functional theory calculations (periodic boundary conditions, plane-wave DFT) gave deep insight into the vibrational properties of crystals and generally provided reliable assignment of the whole spectral range, but presented a few limitations, as described above. Nonetheless, the limitations were well identified and confined to specific modes and could be easily overcome with a little help from discrete calculations.

References:

[1] A. Lemmerer, Covalent assistance to supramolecular synthesis: modifying the drug functionality of the antituberculosis API isoniazid in situ during co-crystallization with GRAS and API compounds, CrystEngComm, 14 (2012) 2465-2478.
[2] D.J. Shaw, K. Adamczyk, P. Frederix, N. Simpson, K. Robb, G.M. Greetham, M. Towrie, A.W. Parker, P.A. Hoskisson, N.T. Hunt, Multidimensional infrared spectroscopy reveals the vibrational and solvation dynamics of isoniazid, J. Chem. Phys., 142 (2015).
[3] A. Favila, M. Gallo, D. Glossman-Mitnik, CHIH-DFT determination of the molecular structure infrared spectra, UV spectra and chemical reactivity of three antitubercular compounds: Rifampicin, Isoniazid and Pyrazinamide, J. Mol. Model., 13 (2007) 505-518.
[4] A.k. Pandey, A. Bajpai, V. Baboo, A. Dwivedi, Structural, Electronic, and Vibrational Properties of Isoniazid and Its Derivative N-Cyclopentylidenepyridine-4-carbohydrazide: A Quantum Chemical Study, J. Theor. Chem., 2014 (2014) 15.
[5] A.R. Owen, J.W. Golden, A.S. Price, W.A. Henry, W.K. Barker, D.A. Perry, Surface-Enhanced Vibrational Spectroscopy and Density Functional Theory Study of Isoniazid Layers Adsorbed on Silver Nanostructures, J. Phys. Chem. C, 118 (2014) 28959-28969.
[6] E. Akalin, S. Akyuz, Vibrational structure of free and hydrogen bonded complexes of isoniazid: FT-IR, FT-Raman and DFT study, J. Mol. Structure, 834 (2007) 492-497.

Solventless Olefin Epoxidation Using a Mo-Loaded Biomass Catalyst

Cécile Petit[1], Miguel V. Silva[1], Ana S. Mestre[1], Conchi O. Ania[2], Pedro D. Vaz[3,4], Ana P. Carvalho[1], Carla D. Nunes[1]

1. *Centro de Química e Bioquímica and Centro de Química Estrutural, Faculdade de Ciências, Universidade de Lisboa, Lisboa, Portugal*
2. *CEMHTI (UPR 3079), CNRS, Université d'Orléans, Orléans, France*
3. *ISIS Neutron & Muon Source, STFC Rutherford Appleton Laboratory, Chilton,Didcot, Oxfordshire, UK*
4. *CICECO – Aveiro Institute of Materials, Departamento de Química, Universidade de Aveiro, Aveiro, Portugal*

Reusable heterogeneous catalysts have attracted a great deal of interest from laboratory and industrial points of view [1]. Since most of the catalysts are expensive and contaminate the environment, the development of efficient methods for recovery and reuse of the catalysts is a very important aspect from an economical point of view. In recent years, to overcome these problems, heterogenization of homogeneous catalysts has attracted much attention because it combines the best properties of both homogeneous and heterogeneous counterparts [2]. Among the various approaches for immobilizing soluble catalysts, covalent attachment has been the most frequently used strategy, as the resulting heterogeneous catalysts have good stability during the catalytic reactions. In this approach, catalyst leaching from the support is minimized and thus, provides a way to prepare site isolated catalysts.

Carbons are the most versatile materials used in the modern fields of renewable energy, environmental science and catalysis. However, there is a need and indeed a desire to develop increasingly more sustainable variants of classical carbon materials particularly when the whole life cycle is considered. Therefore, the synthesis and application of sustainable carbon materials are receiving increasing levels of interest, particularly as supports of catalysts. Selective olefin epoxidation is a very important process since epoxides are relevant building blocks across many areas. In this context, Mo-catalyzed olefin epoxidation has received interest from both academic and industrial research laboratories. Continuing research on the development of stable, active and selective catalysts for olefin epoxidation, in this work we describe the preparation of a sisal derived carbon material inspired in literature that was further derivatized with a Mo complex – $[MoI_2(CO)_3(MeCN)_2]$. However, given its disordered nature, a proper structural characterization of these carbon materials is always hard and defying. In this way, using literature data that established some structural models with C, H, N elemental composition similar to the one we prepared helped us understand its structure [3] by performing DFT calculations to assess the structure of the carbon materials used in this work. The optimized structure using Gaussian 09 code at the M06-2X/6-311g(d,p) level with tight convergence criteria was adopted on all atoms, i.e., the ONIOM approach was not considered. The optimized structure of the carbon material is represented in Figure 36.

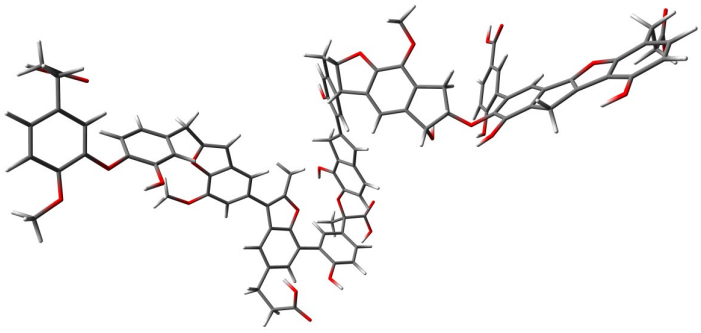

Figure 36: Optimized structure of the carbon material based on a literature geometry [3].

We have then carried out simulation of both the vibrational (FTIR) and of the ^{13}C NMR spectra and compared with the experimental data. According to Figure 37,

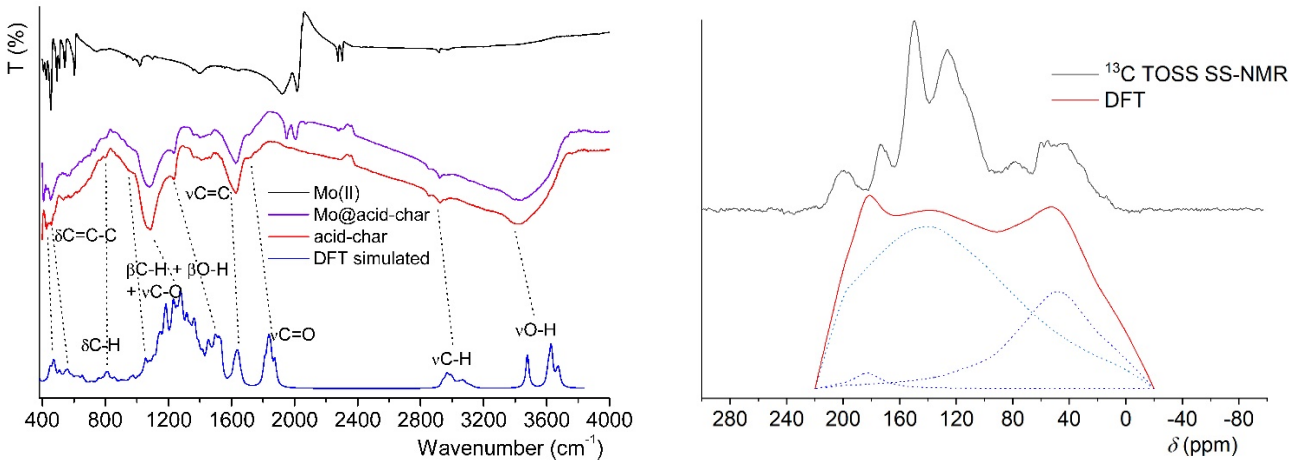

Figure 37: *Left*: FTIR spectra of Mo(II) complex (top), *Mo@acid-char* (middle-top) and acid-char material (middle-bottom) and the DFT simulated profile comparing directly with the spectrum from the carbon material. The band assignments and correlation between the experimental and simulated spectra are also shown. *Right*: Experimental (top) and DFT calculated (bottom) ^{13}C solid-state NMR spectra of the acid-char material. The dashed lines correspond to the individual components (comprising C=O, aromatic C=C and aliphatic moieties) used to fit the overall profile obtained from DFT simulations.

It should be noteworthy to mention the good agreement between the experimental and calculated spectra for both the ^{13}C NMR and the FTIR spectra, validating the choice of this structure as a model for the carbon material herein described.

References:

[1] A. Corma, M. Domine, J.L. Jorda, M.T. Navarro, F. Rey, J. Perez-Pariente, J. Tsuji, B. Mc Culloch, L.T. Nemeth, Chem. Commun., (1998), 2211
[2] G. A. Barf, R. A. Sheldon, J. Mol. Catal. A: Chem., 102 (1995), 23
[3] J.P. Mathews, A.L. Chaffee, Fuel, 96 (2012), 1

Clustering of super-resolution microscopy data helps to understand the adverse effect of anti-cancer drugs in cells

Michael Hirsch, Selene Roberts,

Octopus Facility, Central Laser Facility

Super-resolution microscopy is common technique in life science, which allows higher resolution than it is possible with classical diffraction limited microscopes. With a resolution as low as 20nm it becomes possible to separate individual protein clusters. In the Octopus facility super-resolution microscopes are used both for in-house research and by facility users.

Usually super-resolution images display tens of thousands of observations. Clustering algorithms are used to investigate functional behaviour of proteins under different conditions. Many algorithms use parameters that must be well chosen to make the algorithm effective. We adopted a recent development that uses Bayesian statistics in order to estimate the optimal parameter values and therefore avoids this issue. To achieve that, the parameter space has to be explored, which increases the computational effort. We also wanted to analyse much more data than has been anticipated in the original algorithm design. Therefore, we modified the clustering algorithm so that we could run it in hundreds of jobs on SCARF in a time efficient manner.

We used this arrangement to contribute to the investigation of the effect of the anti-cancer drug Lapatinib on cancers related to HER2 and HER3 of the epidermal growth factor receptor family.

Clustering of receptors is an important regulatory mechanism to prime cells to respond to stimuli. To understand these processes, it is therefore necessary to use clustering algorithms to measure parameters such as numbers of clusters, cluster radii and the number of localizations per cluster of proteins in cells for different perturbations. Cell samples prepared using many different conditions (e.g. with and without ligands and/or drugs) are imaged which generates a vast amount of data to be compared.

The cluster analysis, of HER2 and HER3 in the commonly used breast cancer cell line model SKBR3 cells, was important because HER2 is overexpressed in many tumours, and the deregulated proliferation of cancerous cells is driven by cooperation with its preferred receptor partner, HER3. In cells samples treated with the anti-cancer drug, lapatinib, and the natural stimulatory ligand for HER3, Neuregulin, we show that drug-bound HER2 induces higher order oligomers. We hypothesised that the nucleation of these receptors creates signalling platforms that explain the counterintuitive and undesirable, further increase in cell growth upon ligand binding in the presence of this anti-cancer drug.

J. Claus, G. Patel, F. Autore, A. Colomba, Gregory Weitsman, Fanya N Soliman, Selene Roberts, Laura C Zanetti-Domingues, Michael Hirsch, Francesca Collu, Roger George, Elena Ortiz-Zapater, Paul R Barber, Boris Vojnovic, Yosef Yarden, Marisa L Martin-Fernandez, Angus Cameron, Franca Fraternali, Tony Ng and Peter J Parker. *Inhibitor-induced HER2-HER3 heterodimerisation promotes proliferation through a novel dimer interface*. *eLife* (**2018**);7:e32271 doi: 10.7554/eLife.32271

Simulation and Analysis of Muon Avoided-Level-Crossing Resonance Spectra

Francis Pratt[1] and Stephen Cottrell[1], Leandro Liborio[2] and Simone Sturniolo[2]

1. *ISIS*
2. *SCD*

A joint ISIS/SCD project is under way to build a framework for computing muon stopping sites in a range of condensed matter systems which will provide strong support to the ISIS Facility μSR programme. One of the main requirements here is to be able to predict and interpret muon avoided-level-crossing (ALC) spectra in molecular systems. This requires open-shell electronic structure calculations using DFT which provide equilibrium geometries and hyperfine tensors of muoniated radical states which in turn define the measured ALC spectra.

Calculations for isolated molecules are made using Gaussian16 and solid-state calculations are made using CASTEP. Procedures for correcting for the significant quantum delocalisation of the muon have been established. A computer program CalcALC has been developed to provide a graphical user interface to the calculations, providing a smooth interface between the user-provided molecular structures as input and the simulated ALC spectra as output. The program manages the calculations by building, submitting and monitoring SCARF DFT jobs and interpreting the results. It can read output from both Gaussian and CASTEP jobs. It currently generates jobs only for Gaussian but in future it is hoped that it will be able to provide a complete end-to-end process using CASTEP as well.

The calculations have proved invaluable when working with ALC spectroscopy at the muon instruments, having now been used in conjunction with a number of ISIS experiments to guide and interpret the measurements. Fig.38 shows example calculations supporting a recent experiment studying muoniated radicals in vitamin E.

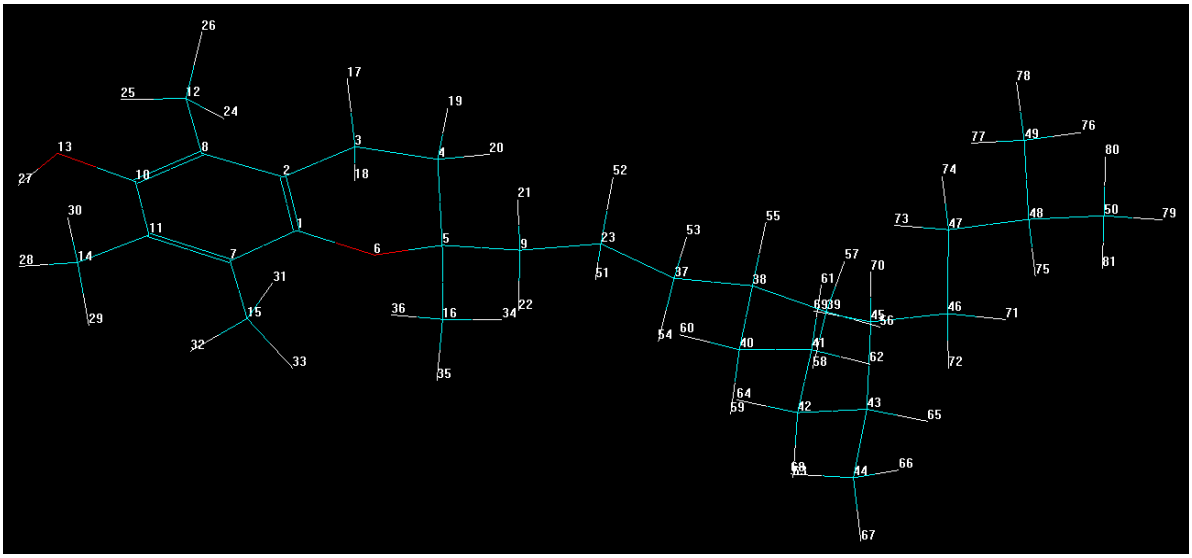

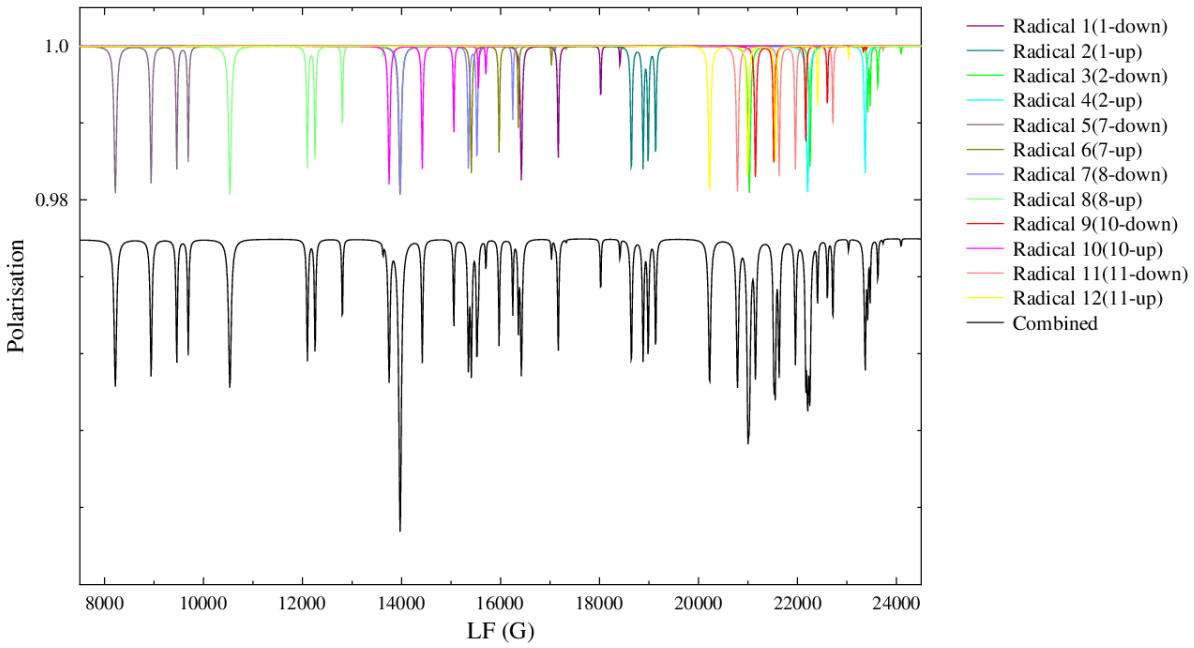

Figure 38: Twelve possible muoniated radical states for vitamin E in solution involve muonium addition above and below the six carbon atoms forming the phenyl ring, shown on the left side of the structure figure (previous page). The lower plot shows the spectrum simulated using SCARF and CalcALC for the case that all of the radicals form with equal probability. The experimentally measured spectrum of Jayasooriya et al is however found to be much simpler than this, corresponding to the signal from radicals predominantly forming at just one or two sites, along with rapid rotation of the methyl groups.

Modeling ion acceleration from ultra-thin graphene using the Vulcan petawatt laser

Leonard N. K. Döhl[1], Reem Alraddadi[2], Nicola Booth[3], Yuji Fukuda[4], Yasuhiro Kuramitsu[5], Christopher Ridgers[1], & Nigel Woolsey[1]

1. *York Plasma Institute, Department of Physics, University of York, York, UK*
2. *Physics Department, Science Colleges, King Saud University, Riyadh, Saudi Arabia*
3. *Central Laser Facility, Rutherford Appleton Laboratory, Didcot, UK*
4. *Kansai Photon Science Institute, Japan Atomic Energy Agency, Kyoto, Japan*
5. *Graduate School of Engineering, Osaka University, Osaka, Japan*

Understanding the physical mechanisms of laser-based ion acceleration is important for the development of energetic ion sources. These have potential applications in fast-ion ignition of inertial confinement fusion targets, oncology and radiography [1,2]. One approach to improve and increase the ion energies is by using ultra-thin targets. In our work we investigate the feasibility of high-energy ion generation by irradiating a high-contrast, ultra-intense laser pulse on targets composed of single- and multi-layer graphene. Graphene is the thinnest man-made material known and exhibits unique material properties that make it ideal for studying carbon ion acceleration [3,4].

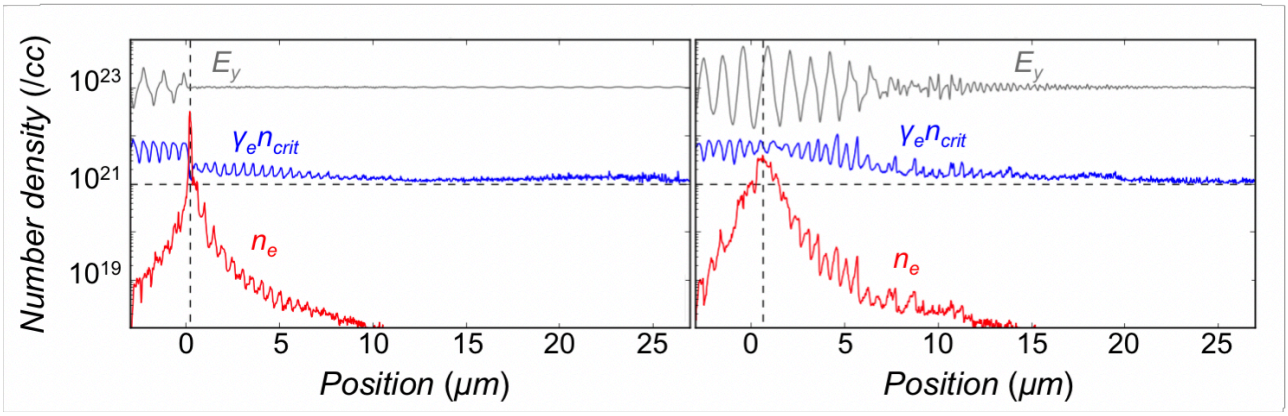

Figure 39: As the plasma density, n_e, transitions from an overdense to a relativistic underdense system (as in, $n_e < \gamma_e n_{crit}$) the plasma becomes transparent to a laser pulse (with electric field, E_y). Left image is at -525 fs and right image at -455 fs, i.e. before the peak of the laser pulse. The laser propagates from left to right in the spatial axis. When the transition from $n_e > \gamma_e n_{crit}$ at about -525 fs (left) to $n_e < \gamma_e n_{crit}$ at -455 fs (right) occurs, the laser pulse propagates through the relativistically transparent target.

The objective was to use EPOCH and SCARF to model an experiment on the Vulcan petawatt laser and interpret the spectra of laser-driven ions recorded with a detector stack composed of radiochromic film and CR-39 plates. A key aspect of the experiment was the use of a double plasma mirror in order ensure a high-contrast, ultra-intense laser pulse interacts with the target preserving the target integrity up until the interaction with the main peak of the laser pulse.

The simulated laser parameters reproduce the Vulcan petawatt beam as a Gaussian temporal profile of 700 fs at full-width-half-maximum. The graphene targets are defined as a uniform slab with a density ramp on the front and rear surface. To ensure reliable and converged results we have used one-dimensional simulations to explore the influence of simulation cell size and the number of particles per cell. In addition, we used the simulations to study how carbon ion energies vary with target thickness and peak laser intensity. This enables us to understand how the laser interaction physics links to the observations of high energy ions. A key observation from the simulations is the onset of relativistic induced transparency (RIT) [5].

Fig. 39 shows the calculated transverse electric field of the laser, E_y, the electron density, n_e, and relativistic critical density, $\gamma_e n_{crit}$. The onset of RIT occurs around -525 fs before the peak of the laser pulse. By -455 fs (70 fs later) when $n_e < \gamma_e n_{crit}$ the laser pulse has propagated through the graphene plasma slab. After the onset of RIT an electrostatic field, E_x, which is not associated with the laser, moves rapidly forward and drives the ions along with it. Over the time of RIT the ions are co-moving with the peak of E_x and, as a result, increase in energy.

References:

[1] S. Palaniyappan *et al.*, Nat. Commun. **6**, 10170 (2015).
[2] S. V. Bulanov *et al.*, Phys. - Uspeckhi **57**, 1149 (2014).
[3] V. B. Mohan *et al.*, Composites Part B **142** (2018) 200-220.
[4] N. Khasanah *et al.*, High Power Laser Sci. Eng. **5**, e18 (2016).
[5] G. M. Petrov *et al.*, Plasma Phys. Control. Fusion **59**, 075003 (2017).

Understanding the Interface between Water and Biomaterials: Combining Neutron Scattering and in-silico studies

Jose A Martinez-Gonzalez[1], Ilian Todorov[2] and Victoria Garcia Sakai[1]

1. *ISIS Neutron and Muon Source, STFC Rutherford Appleton Laboratory, Harwell Oxford, Didcot.*
2. *Computational Chemistry Group, STFC Daresbury Laboratory, Sci-Tech Daresbury, Keckwick Lane, Daresbury.*

Understanding the interactions between water and the surface of biomaterials is fundamental, for understanding wettability phenomena, adhesion of proteins or tissue regeneration around implant. Water in contact with the surface, so-called interfacial water, has attracted plenty of interest for many years. The properties of interfacial water are dependent on the specific interactions with the biomaterial, and typically result in significant changes to bulk state, such as the prevention of ice formation, water remaining in a glassy state below the freezing point of water. This project wants to improve the knowledge of the properties of this interfacial water using a combination of experimental and theoretical approaches. A new humidity cell that allows the characterisation of the growth of the different solvation layers of water using neutron scattering experiments will be developed. In parallel molecular dynamics simulations of biomaterials will be carried out, to obtain an atomistic view of the interface. Experiments and simulations combined provide a strong way to improve current water models and force-fields that define the interactions between the materials.

Actually, the work that we are developing at SCARF is focused in the theoretical studies on the project. We are using DL_Software package, developed by Computational Chemistry group at SCD, and Gromacs Software to obtain different classical molecular dynamics simulation of several biomaterials, such as silicon or phospholipids membrane in contact with water. At this stage, we are testing different models of force-fields for the materials and the water in order to collect as much as possible information that allow us to compare with the neutron experiments which will be performed during the next period of time (across next year). A preliminary visual analysis has been done and we are beginning the early computational analysis to obtain the spectroscopic properties of the interfacial water. Some visual representations of the interfacial water in contact with different materials are shown at Figure 40.

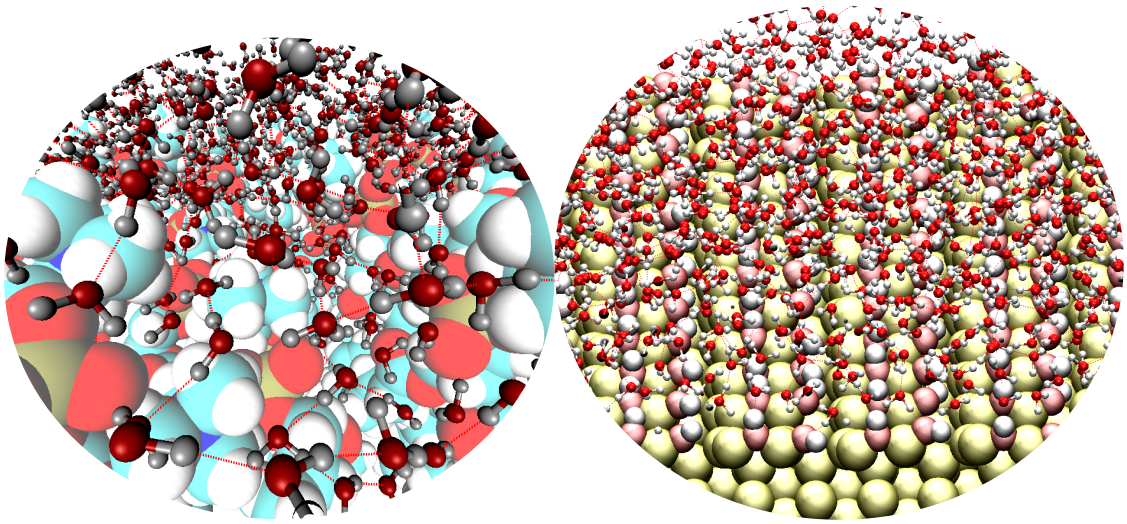

Figure 40: Visual representation of the interfacial water in contact with POPC (left) and with silicon terminated OH (right).

Evening out the spin and charge parity to increase T_C in unconventional superconductors

Swagata Acharya[1], Dimitar Pashov[1], Cédric Weber[1], Hyowon Park[2,3], Lorenzo Sponza[4], Mark van Schilfgaarde[1]

1. *King's College London, London, UK,*
2. *Department of Physics, University of Illinois at Chicago, Chicago, Illinois, USA*
3. *Materials Science Division, Argonne National Laboratory, Argonne, Illinois, USA,*
4. *LEM UMR 104, ONERA-CNRS, Châtillon, France*

We use the computing resources provided by STFC Scientific Computing Department's SCARF cluster to answer one of the longest standing questions in condensed matter: the origin and nature of superconductivity in unconventional superconductor Sr_2RuO_4. Using our recently developed QS*GW* + DMFT, we compute spin (Figure 41), charge (Figure 42) susceptibilities and show their collective contribution to the superconducting pairing (Figure 43). We also gain insight into the harmonious interplay of spin and charge degrees of freedom that lead to increment in superconducting transition temperature under strain, that also observes non-trivial changes in the Fermi surface topology (Figure 44). The work is available on arxiv[1].

References:

[1] S. Acharya, et al., arXiv preprint arXiv:1811.05143 (2018).

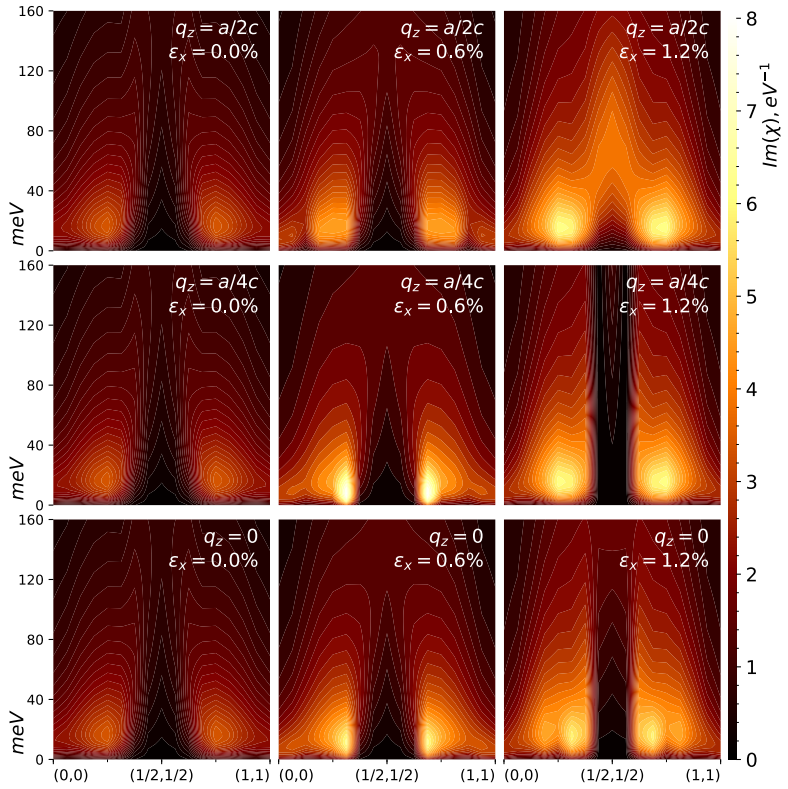

Figure 41: Spin fluctuations: incommensurability and coherence: Imaginary part of the dynamic spin susceptibility $X^S(q,\omega)$ are shown in the Cartesian *xy* plane at different values q_z, and for different strains ε_x. The unstrained compound shows a spin fluctuation spectrum strongly peaked at (0.3,0.3,q_z) (units 2π/a). At ε_x=0, X^S is nearly independent of q_z, but it begins to depend on q_z for ε_x>0. With increasing strain fluctuations become more coherent and strongly peaked, reaching a zenith at $\varepsilon_x = \varepsilon^*_x$ (0.6%), where T_c is maximum. For $\varepsilon_x > \varepsilon^*_x$, this peak becomes more diffuse; also a secondary incoherent peak emerges at (0.15,0.15, q_z), and the quasi anti-ferromagnetic vector (1/2,1/2,a/2c) acquires spectral weight around ω=40meV. Note also the spectral weight near the FM vector (0,0,0), and its evolution with ε_x.

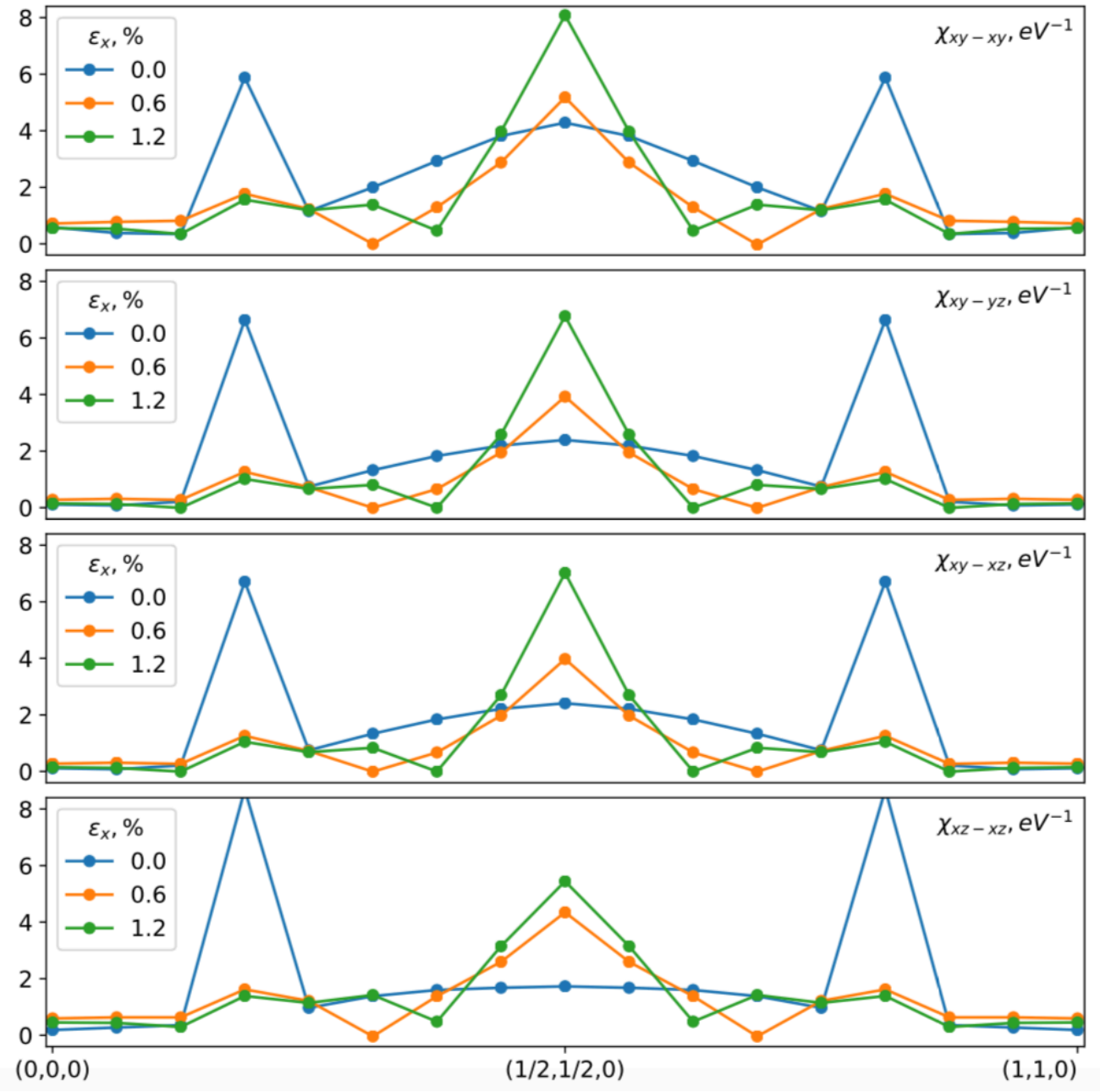

Figure 42: Charge susceptibilities and commensurability: Real part of the static charge susceptibility $X^C(q, \omega = 0)$, shown along the Cartesian (000) to (110) direction, and for different strains ε_x. The unstrained compound shows three-peaked charge fluctuation, with sharp peaks at IC vector (0.2, 0.2, 0) (and by symmetry at (0.8, 0.8, 0)) and a broad peak at (0.5, 0.5, 0). With strain the structure becomes sharply single-peaked at commensurate (0.5, 0.5, 0). The peak at the commensurate vector develops at the cost of the charge fluctuation weights from the IC vectors. The systematic evolution from large wavelength triplet to shorter wavelength singlet fluctuations, under strain, is common to all inter- and intra-orbital charge fluctuations. The strong, often the most dominant, inter-orbital charge fluctuations can be observed in Ru-$d_{xy\text{-}xz}$ and Ru-$d_{xy,yz}$ channels.

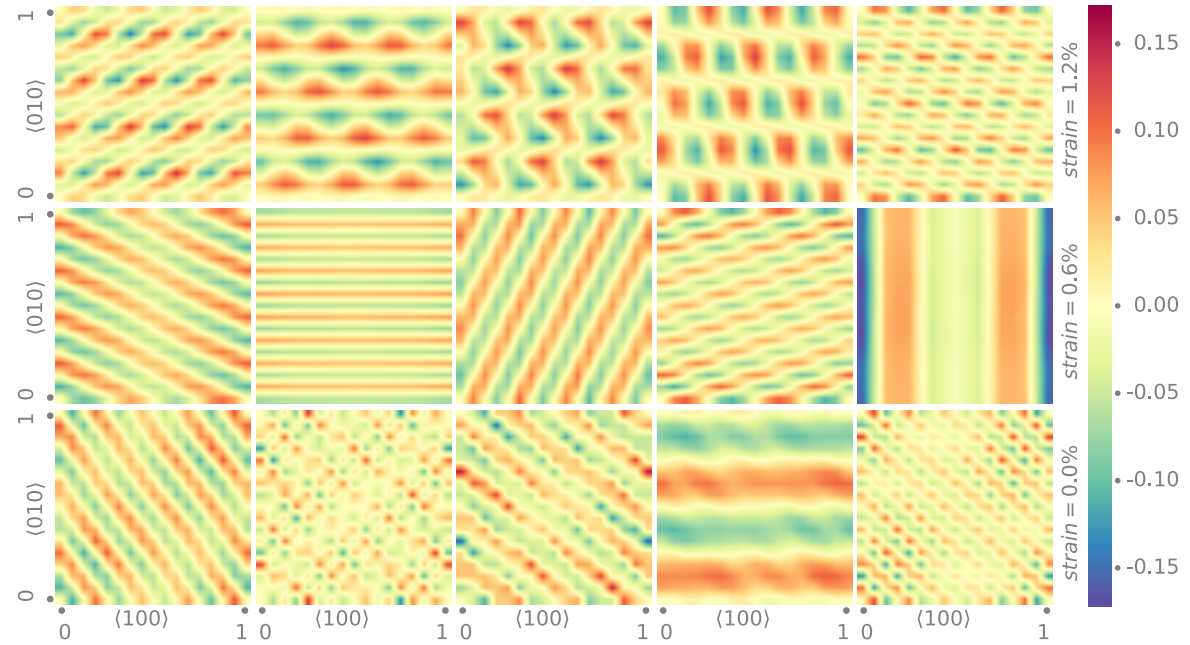

Figure 43: Superconducting pairing: nodal character and dimensionality: The superconducting pairing gap symmetries for the leading five eigenvalues are shown for different strains ε_x in the (100)-(010) plane in crystal coordinates. Nodal lines, gap minima and anti-nodal lines can be observed across all three spatial directions. The nodal structure evolves in a non-trivial fashion under strain, keeping the basic three dimensional gap structure intact across all strains. The first two eigenvalues for all strains are nearly degenerate.

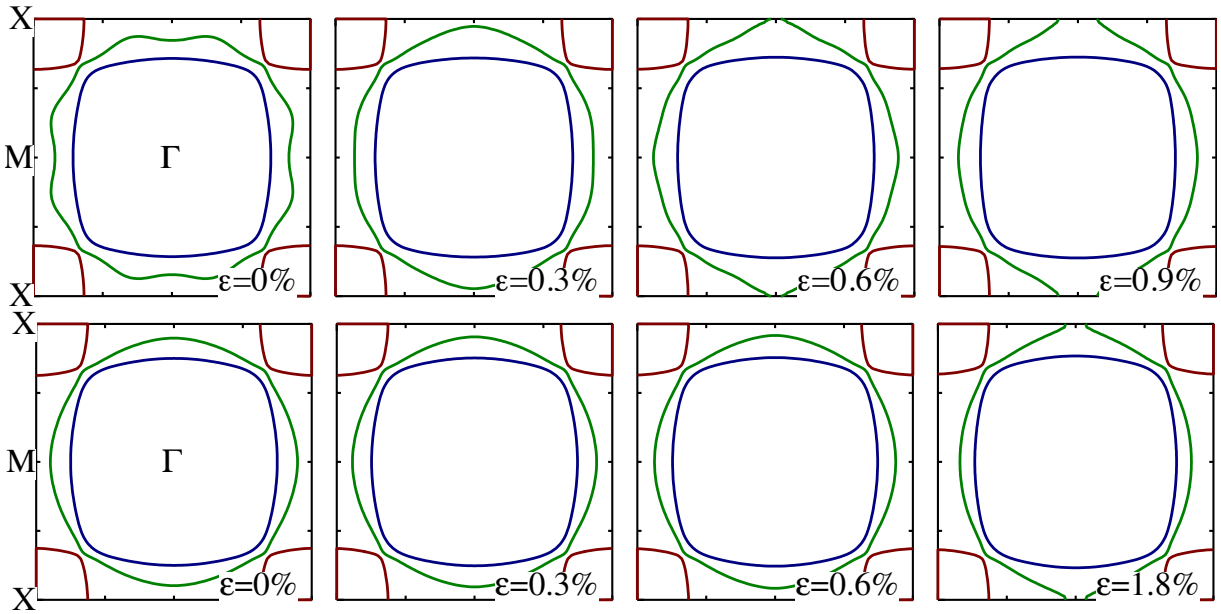

Figure 44: Evolution of Fermi surface topology under strain: Top row shows the QS*GW* Fermi surfaces in the basal plane, for a [100] compressive strain with ε_x=(0%, 0.3%, 0.6%, 0.9%). Spin orbit coupling is included (its omission makes a modest change to the Fermi surfaces). States derive almost exclusively of Ru t_{2g} orbitals xy, xz, yz; the orbital character of each pocket changes moving around the contour. xy character is present on the entire Fermi surface: it resides on the blue pocket on the Γ-X line, and on the green on the Γ-M line. Under strain, the four M points lose the 4-fold rotational symmetry, and at $\varepsilon_x = \varepsilon^*_x$ the topology of the green band changes. Bottom row shows corresponding results for DFT. In DFT the transition also occurs, but near ε_x=1.8% (bottom right panel), instead of ε^*_x.

Comparison between Density Functional Theory and Density Functional Tight Binding approaches for finding the muon stopping site in organic molecular crystals

S. Sturniolo, L. Liborio, S. Jackson

Theoretical and Computational Physics Group, Scientific Computing Department, RAL, STFC, UK

Finding the possible stopping sites for muons inside a crystalline sample is a key problem of muon spectroscopy. In a previous work[1], we suggested a computational approach to this problem, using Density Functional Theory software in combination with clustering techniques and a random structure searching approach using a Poisson sphere distribution. In this work we test this methodology further by applying it to three organic molecular crystals model systems: durene, bithiophene, and tetracyanoquinodimethane (TCNQ). Using the same sets of random structures we compare the performance of Density Functional Theory software CASTEP and the much faster lower level approximation of Density Functional Tight Binding provided by DFTB+, combined with the use of the 3ob-3-1 parameter set. We show the benefits and limitations of such an approach and we propose the use of DFTB+ as a viable alternative to more cumbersome simulations for routine site-finding in organic materials. Finally, we introduce the Muon Spectroscopy Computational Project software suite, a library of Python tools meant to make these methods standardized and easy to use.

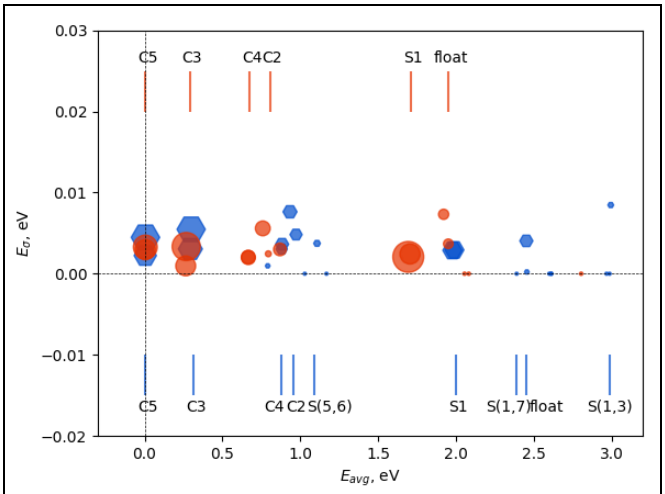

Figure 45: Bithiophene

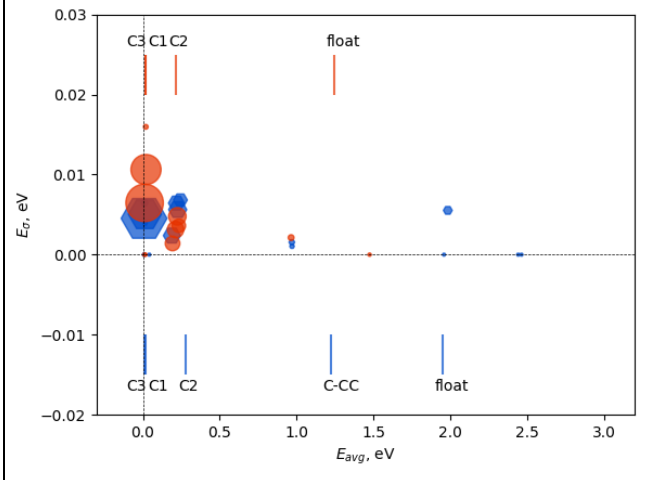

Figure 46: Durene

Figures 45, 46 and 47 show the clusters that our method obtained for durene, bithiophene, and TCNQ. The circles represent CASTEP generated clusters and the hexagons are DFTB+ clusters. The size of the markers is proportional to the number of structures in each cluster. The average energies and corresponding standard deviations of each cluster are indicated in the x-axis and y-axis respectively. Labels are added to show the average energies for structures classified by site for CASTEP and DFTB+ results. These average energies for structures classified by the type of molecular sites -specific molecular stopping sites can be represented by more than one cluster- are also marked in each plot by lines for CASTEP-optimized structures (top) and DFTB+ ones (bottom).

Low standard deviations indicate a more ‘consistent’ cluster, with less dispersed energies, thus better convergence to the minimum. Energies are naturally different from different molecular sites, though they tend to vary very little for crystallographically inequivalent realizations of the same molecular site.

More importantly, CASTEP and DFTB+ results tend to match remarkably well in energy in a lot of cases. Low energy sites tend to match especially well (e.g. C5 and C3 in bithiophene, C3 and C2 in durene, and C3 in TCNQ). Some of the higher energy sites (S1 in bithiophene, C4 and C2 in TCNQ, and the floating sites in general) have growing discrepancies as the energies get higher. The biggest error appears for the N1 site in TCNQ, which is the lowest in energy in CASTEP but is approximately 0.6 eV higher in DFTB+.

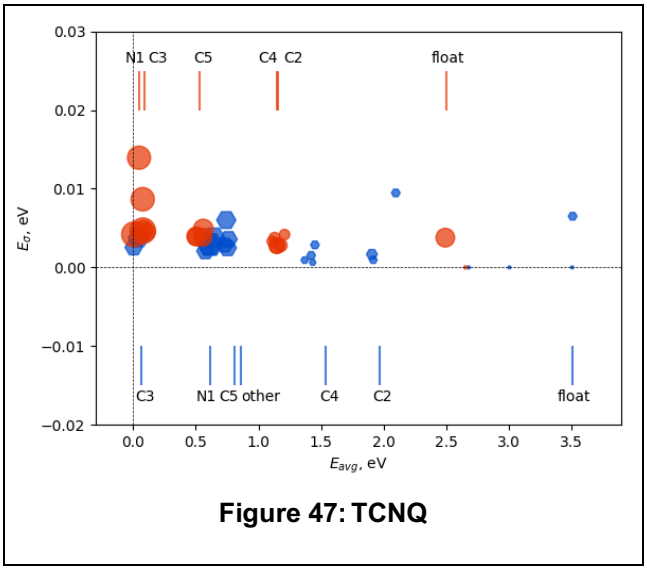

Figure 47: TCNQ

In this work, the muon stopping sites predicted for bithiophene, TCNQ and durene, by using a DFT-based methodology, were compared with those predicted using a higher level approximation that uses Density Functional Tight Binding (as implemented in the DFTB+ code).

The potential muon stopping sites found by the DFTB+-based methodology agree very well with those found by the CASTEP-based methodology. Moreover, DFTB+ calculations are computationally much cheaper than DFT calculations and could potentially be used for treating very large organic systems such as polymers or proteins. This work offers a strong case that it would be reasonable to do so, while also highlighting what are the limitations that a user of the tight binding approach should be watching out for.

A paper based on this work was submitted to the Journal of Chemical Physics.

References

[1] L. Liborio, S. Sturniolo and D. Jochym, The Journal of Chemical Physics, 148, 134114 (2018)

Monte Carlo simulations of ISIS TS1 target, reflector and moderator assembly using FLUKA

Lina Quintieri, Steven Lilley

ISIS Facility, STFC Rutherford Appleton Laboratory, Chilton, Didcot, UK

The 800 MeV proton beam from the ISIS synchrotron is serving two target stations: Target Station 1 (TS-1) which was up and running by 1987 and Target Station 2 (TS-2) following in 2008. The TS-1 target is a twelve-plate tantalum-clad tungsten target, irradiated by a 40-pulses-per-second proton beam (beam current is approximately 160 μA). The neutrons produced in spallation reactions are slowed to energies useful for neutron scattering experiments by moderators (surrounded by beryllium reflector) which are designed to meet the instrument requirements for neutron flux and resolution. The target, reflector and moderators (TRAM) of ISIS Target Station 1 is currently being redesigned to increase maintainability, extend the life of the target station and (if possible) provide an increase in useful neutron output. The new TRAM design geometry has been accurately reproduced with FLUKA code [1] based on the latest engineering drawings, shown in Figure 48.

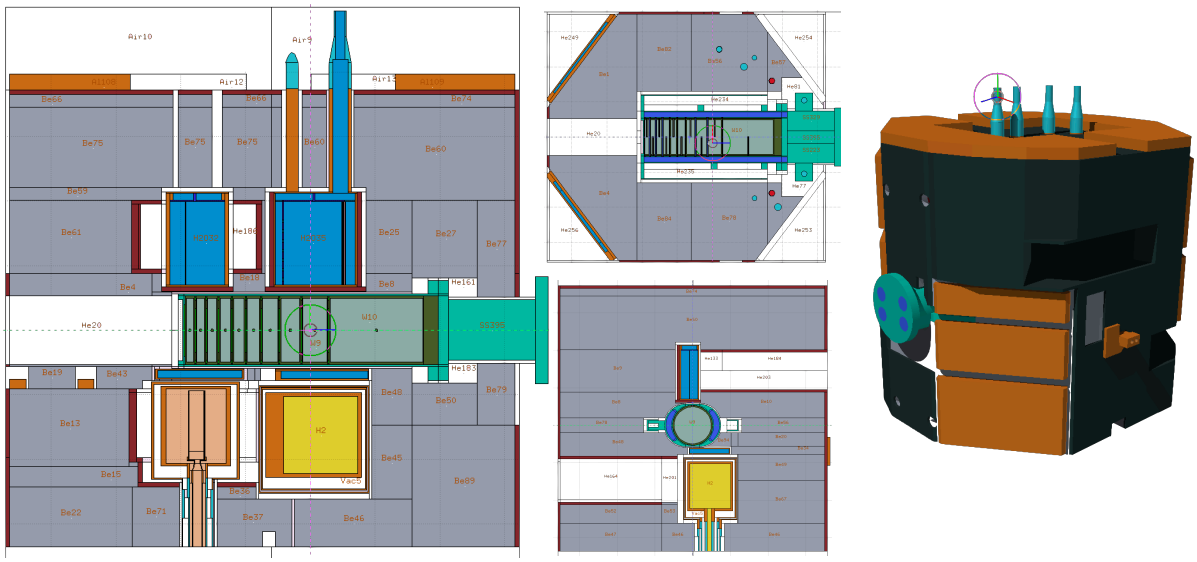

Figure 48: FLUKA model geometry

FLUKA is a Monte Carlo radiation transport code which can simulate the proton beam interactions with the target, the subsequent neutron and gamma production and the further transport of these particles down from 800 MeV to 1 meV. The simulation outputs include neutron production, nuclear heating, activation products and decay heat. The nuclear heating is particularly important as it determines the cooling requirements in order to ensure the target can be operated safely. The nuclear heating varies by material and particle type as some materials do not absorb some particles as readily as other e.g. Boron is very good at stopping neutrons but not very good at stopping gamma rays.

The spatial distribution of nuclear heating for different particle types is shown in Figure 49 These results have been used to cross check earlier calculations.

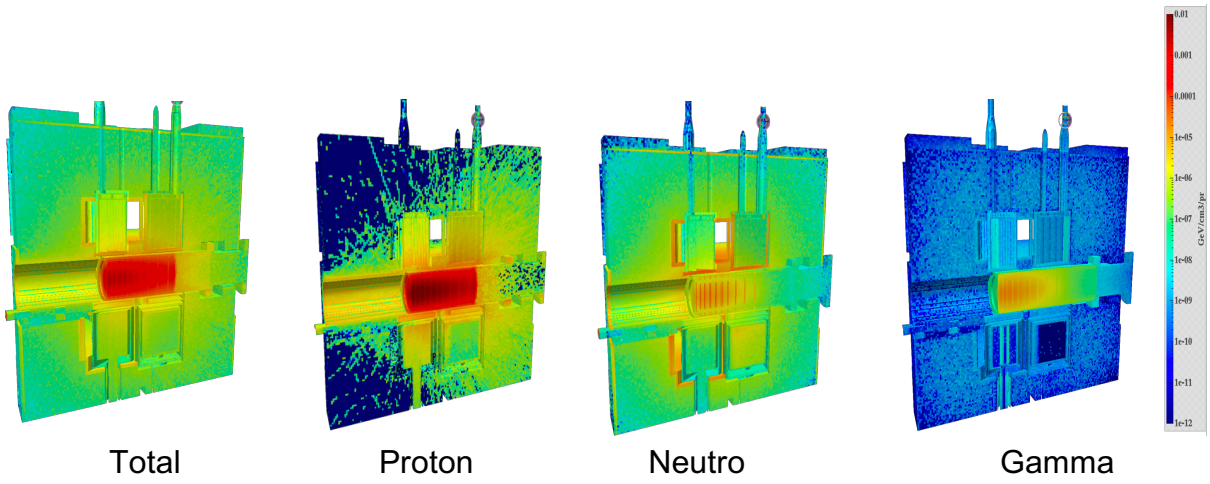

Figure 49: Energy deposition profile: contribution of different particles

References:

[1] A. Fassò et al. - FLUKA: a multi-particle transport code, Tech. Rep. CERN- 2005-10 (2005), INFN/TC-05/11,SLAC-R-773

Predicting asphaltene aggregate structure from molecular dynamics simulation: Comparison to neutron total scattering data

Thomas F. Headen[1], Michael P. Hoepfner[2]

1. *STFC, ISIS*
2. *The University of Utah*

Asphaltenes are a complex and problematic fraction of crude oil that can precipitate, alter wettability of oil reservoirs and stabilise unwanted oil-in-water emulsions. Asphaltenes have a high proportion of aromatic carbon and heteroatoms (N, S, O) and are generally thought to consist of one (or more) condensed aromatic cores with alkyl side chains.

Asphaltenes have been extensively studied by molecular simulation techniques allowing aggregation structure and dynamics to be studied in unprecedented detail. However, to date, there has been little experimental verification of the simulations methods used. In this study, wide *Q*-range neutron total scattering data was collected for precipitated asphaltene solids and concentrated solutions in 1-methylnaphthalene using the Near and InterMediate Range Order Diffractometer (NIMROD) on the second target station at ISIS.

The scattering data from the NIMROD instrument can simultaneously probe structural correlations from < 1Å to >300Å. Large molecular dynamics simulations of both solid asphaltenes and the concentrated asphaltene solutions were run using the GROMACS Molecular Dynamics (MD) code on the SCARF compute cluster, with the resulting trajectories used to calculate simulated scattering data for three diverse asphaltene molecular structural models.

For the asphaltene solutions we found that the simulated scattering closely matched the slope of the experimental small-angle scattering, indicating good replication of the fractal nature of asphaltene aggregation. However, the size of the aggregates in the simulation was constrained by the attainable simulation box-size which limited the fit to the data at low *Q*. In the intermediate *Q* region, two broad peaks are seen in the experimental data of solid asphaltenes, corresponding to aromatic stacking (at the highest *Q*) and non-specific nearest neighbour correlations at the lower *Q*. All simulations showed only one peak, indicating greater phase separation into aromatic rich and poor regions is required to match the data.

The results show that in both the solid and solution models, larger box sizes and longer simulation times are required to properly replicated asphaltene structures, with coarse-graining methods being considered as the best way to achieve this in reasonable timescales.

A paper based on this work was submitted to the Journal of Energy and Fuels.

Origin of Room Temperature Ferroelectricity in Croconic Acid

Sanghamitra Mukhopadhyay[1], Matthias J. Gutmann[1], and Felix Fernandez-Alonso[1,2]

1. *ISIS Facility, Rutherford Appleton Laboratory, Chilton, Didcot, Oxfordshire*
2. *Department of Physics and Astronomy, University College London, London*

Hydrogen bonded organic ferroelectrics are important functional materials for potential technological applications in flexible electronics. The observation of above-room-temperature ferroelectricity in the single-component molecular crystal croconic acid (molecular formula $C_5O_5H_2$) [1] has initiated a significant discussions on how carbon-based materials can develop and sustain a macroscopic electric polarization at high temperatures [2]. Role of hydrogen bonds is important in this class of materials for designing new functionalities. Microscopic knowledge of structure and dynamics of those hydrogen bonds are thus crucial.

As a continuation of a series of work on croconic acid we use state-of-the-art calculations based on plane wave pseudo potential density functional theory to predict the structure and dynamics of hydrogen bonds to search the origin of ferroelectricity in this material [3-5]. Temperature dependent inelastic neutron scattering (INS) experiments are done on IN1-Lagrange spectrometer at Institut Laue-Langevin, Grenoble, France and TOSCA spectrometer at ISIS, UK. The INS spectrum are interpreted using first principles lattice dynamics calculations within quasi-harmonic approximations. Correlating structure and dynamics of this functional material, it is found that the in-plane strains on hydrogen bonds originated from Jahn-Taylor type distortion are responsible for high ferroelectric polarisation of these organic solids.

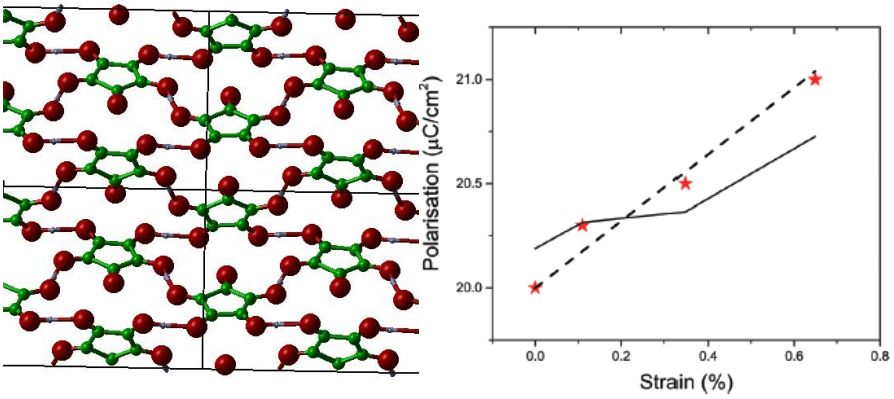

Figure 50: Left: Hydrogen bond structure in croconic acid, Right: Linear relationship with strain and polarisation as obtained from calculations and compared with experiments.

Electronic-structures and subsequently lattice dynamics calculations are performed with the DFT code CASTEP on SCARF computer. For all calculations, optimized normconserving pseudopotentials generated with the Perdew–Burke–Ernzerhof (PBE) functional within the generalized-gradient approximation (GGA) have been used. The dispersion corrections (PBE + D) following the methodology of Tkatchenko and Scheffler (TS) are incorporated in all calculations. A plane-wave cutoff of 800 eV and a Brillouin-zone (BZ) sampling on 18 symmetry reduced k-points are used to converge energy and atomic forces to $9.6x10^3$ eV per ion and $1.0x10^3$ eV $Å^{-1}$, respectively. The lattice dynamics calculations are done via diagonalisation of dynamical matrices computed using density-functional perturbation theory (DFPT) and linear-response methods. Unit-cell polarizations are obtained via Berry-phase method, as implemented in CASTEP.

The calculated values of temperature dependent net spontaneous polarisation qualitatively agree with experiments [6]. It is found that the ferroelectricity is quantum mechanical in nature having contributions (about 20%) from long range ionic structures. The microscopic analysis of the polarisation reveals that the in-homogeneous thermal expansion of lattice introduces extra strain on the hydrogen bond structure of croconic acid leading to high ferroelectricity above room temperature (Fig. 50(b)). An almost-linear relationship between in-plane strain and ferroelectricity has been found which is rare even in inorganic compounds. More details about these calculations can be found in Ref. [6]. These results may help in designing room temperature ferroelectrics from hydrogen bonded organic layered materials.

References:

[1] S. Horiuchi, Y. Tokunaga, G. Giovannetti, S. Picozzi, H. Itoh, R. Shimano, R. Kumai and Y. Tokura, Nature, **463**, 789 (2010).
[2] A. Stroppa, D. D. Sante, S. Horiuchi, Y. Tokura, D. Vanderbilt and S. Picozzi, Phys. Rev. B: Condens. Matter Mater. Phys., **84**, 014101 (2011).
[3] F. Fernandez-Alonso, M. J. Gutmann, S. Mukhopadhyay, D. B. Jochym, K. Refson, M. Jura, M. Krzystyniak, M. Jimenez- Ruiz and A. Wagner, J. Phys. Soc. Jpn., **82**, SA001 (2013).
[4] S. Mukhopadhyay, M. J. Gutmann, M. Jura, D. B. Jochym, M. Jimenez-Ruiz, S. Sturniolo, K. Refson and F. Fernandez-Alonso, Chem. Phys., **427**, 95 (2013).
[5] S. Mukhopadhyay, M. J. Gutmann and F. Fernandez-Alonso, Phys. Chem. Chem. Phys., **16**, 26234 (2014).
[6] S. Mukhopadhyay, M. J. Gutmann, M. Jiménez-Ruiz, D. B. Jochym, K. T. Wikfeldt, K. Refson and F. Fernandez-Alonso, Phys. Chem. Chem. Phys., **19**, 32216 (2017).

Structure and Dynamics of Molten NaF using First Principles Molecular Dynamics

Sanghamitra Mukhopadhyay and Franz Demmel

ISIS Facility, Rutherford Appleton Laboratory, Chilton, Didcot, Oxfordshire

Molten salts are ionic liquids at high temperatures. In this molten form these salts find industrial applications as heat storage in modern solar power plants and in next generation nuclear reactors by exploiting their unique properties, such as large heat capacities and high temperature ionic conductivities with a stability for a wide liquid temperature range [1,2]. A microscopic model of molten salts, which assume its structure as a random network of charged particles with charge ordering due to the long range Coulomb interactions, is important to understand and design the material in these purposes. Due to the complex disordered and ionic nature, the formulation of microscopic models of these molten salts is challenging. In this respect, molten alkali halides attract a lot of attention both from experimental and computational scientists as prototypes of molten salts.

We have done microscopic analysis of structure and dynamics of molten NaF through first principles molecular dynamics (MD) simulations and have compared results with a quasi elastic neutron scattering (QENS) experiments done on OSIRIS spectrometer at ISIS [3,4]. MD simulations are performed based on first principles DFT using CASTEP code on a supercell consisting of 256 NaF molecules on SCARF and national high performance computer facility ARCHER computers. The ultrasoft pseudopotentials generated with the Perdew-Burke-Ernzerhof (PBE) functional within the generalized-gradient approximation (GGA) have been used. A plane-wave cut off energy 1000 eV and tolerance for self-consistent energy minimisation below $2.5x10^{-8}$ eV per ion are used. The NPT ensemble with Nose-Hoover thermostat and Andersen-Hoover barostat are incorporated to stabilize temperature and pressure, respectively. A pressure of 1 bar is kept constant and a MD time step of 2 fs is used throughout all calculations. As a property of Andersen's method, during simulations the volume of the cell is allowed to change with temperatures by keeping the shape preserved until the mass density during is 1.914 g/cm^3, which is very near to the experimental density, achieved. Production runs are taken at the experimental temperature 1300 K at that density after equilibriating the simulation cell by 5 ps.

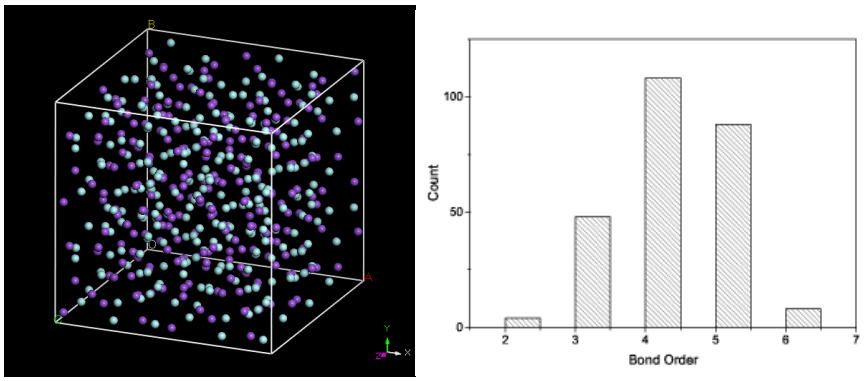

Figure 51: Left: The simulation box of molten NaF. Right: The distribution of bond order of F in simulated molten NaF.

Structural properties of molten salts are studied over 50 ps production run. As expected from calculated PDF, this distribution also shows the most probable peak at 2.3 Å, the interatomic distances of Na and F ions. About 32 % of all Na-F bonds are lying between 2.2-2.4Å, however, the distribution of bond lengths varies from as small as 1.7 Å to almost 3.0 Å predicting the preservation of short range order even in the molten form. The value of F-Na-F varies widely showing a non-Gaussian distribution. Only about 35% of all such

angles are between 80^0 -90^0 and about 40% are more than 110^0 predicting that all Na ions are not octahedral as expected from cubic ionic structure. The analysis on coordination numbers reveals that both Na and F ions are mostly tetrahedral. Five and six coordinated Na and F ions are also been found in the melt. That result agrees with previous structural investigations on molten salts done by force field based MD calculations.

The structure of a liquid is not static but changes with time and temperatures. That is captured through the investigation of its dynamical properties. The calculated dynamical structure factor and intermediate scattering functions are compared well with QENS experiments along with the calculated diffusion coefficients. It is found that F decays a little bit faster than Na at the first 5 ps, but overall diffusion constants of Na and F are almost the same. The initial faster motion of F ions is predicted due to its smaller mass and also change in coordination number with respect to Na as discussed above. More information of this work will be found in [4].

References

[1] C. LeBrun, J. Nuclear Mat. **360**, 1 (2007).
[2] S. Delpech, E. Merle-Lucotte, D. Heuer, M. Allibert, C. L.-B. V. Ghetta, X. Doligez, and G. Picard, Fluorine Chem. **360**, 11 (2009).
[3] F. Demmel and S. Mukhopadhyay, J. Chem. Phys.,**144**, 14503 (2016).
[4] S. Mukhopadhyay and F. Demmel, AIP Conf Proc **1969**, 030001 (2018).

Glassy Dynamic features in Halo-methane Crystals

Jonathan F. Gebbia[1] and Sanghamitra Mukhopadhyay[2]

1. *Grup de Caracterizació de Materials, Departament de Fisica, EEBE and Barcelona Research Center in Multiscale Science and Engineering,Universitat Politècnica de Catalunya, Barcelona, Catalonia*
2. *ISIS Neutron and Muon Source Facility, Rutherford Appleton Laboratory, UK*

Conventional and orientational glasses exhibit complex atomic dynamics which cannot be explained through traditional description of phonons suitable for periodic crystalline solids [1,2]. Structural disorder affects the low-frequency excitations and thus reflects on thermodynamic and transport anomalies with respect to their crystalline counterparts. To understand this issue a number of experiments and simulations are done on halomethanes family, namely CBr_nCl_{4-n} with n = 0, 1, 2. These materials show orientational disorder preserving long range positional order [3].

Electronic structure calculations are performed using CASTEP code on SCARF cluster. A number of calculations are done on CBr_nCl_{4-n} with n = 0, 1, 2 family with unit cell consisting of 32 molecular units. For all calculations, optimized normconserving pseudopotentials generated with the Perdew–Burke–Ernzerhof (PBE) functional within the generalized-gradient approximation (GGA) have been used supplemented with a dispersion correction PBE-G06. A plane-wave cutoff of 950 eV and a Brillouin-zone (BZ) sampling on 4x4x2 Monkuhrst-Pack k-point sampling grid are used. Lattice dynamics calculations are performed by density-functional perturbation theory method (DFPT) implemented in CASTEP code. Full phonon dispersion calculations are done on 8 Q points in the BZ. Linear interpolation method is used to get phonon dispersion plot as shown in Fig. 52. The thermodynamic parameters, for example specific heat (C_p), are calculated from this vibrational data as implemented in the CASTEP code.

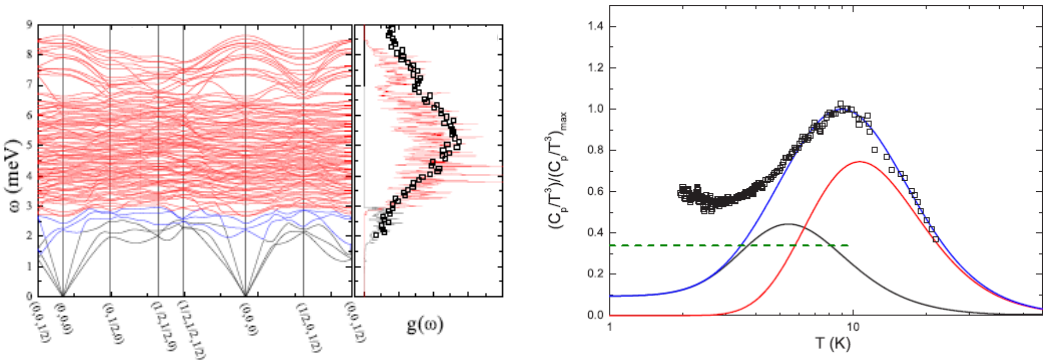

Figure 52: Left: Phonon dispersion and densities of states of CCl_4 crystal Right: Calculated specific heat plotted with experimental data (black square). For more details see Ref [4].

A comparison of these computational results for CCl4 crystal with experiments is shown in the Fig. 52 (a). Excellent agreement between the calculated data and experiments are obtained. From the DFT calculations, it is found that low energy phonons (3-4meV) contribute heavily in the low temperature specific heat of this material and subsequently to the anomalous behaviour of that specific heat. Overlapping phonon branches in the BZ boundary are also found to be responsible for providing Boson like peaks in the specific heat at low temperatures.

References:

[1] A. Bunde, et al. “Vibrational models for the Boson peak”, J. Non-Cryst. Solids 307 - 310 96 (2002).
[2] K. Binder and W. Kob, “Glassy Materials and Disordered Solids” (World Scientific, Singapore, (2005).
[3] B. Parat et al “Polymorphism of CBrCl3” Chemistry of Materials, 17 3359 (2005).

[4] M. Moratalla, J. F. Gebbia, M. A. Ramos, L. Carlos Pardo, S. Mukhopadhyay, S. Rudić, F. Fernandez-Alonso, F. J. Bermejo, and J. L. Tamarit, Phys. Rev. B. **99**, 024 301 (2019).

4. APPENDIX: SCARF HARDWARE DETAILS

Host group	CPU type and frequency	Nodes	Cores /node	Total cores	Interconnect	Total memory
SCARF18	Intel Xeon Gold 6126 CPU @ 2.60GHz	148	24	3552	EDR Infiniband	28416 GB
SCARF17/ DeRevolutionIbus	Intel E5-2650v4 @ 2.2GHz	201	24	4824	EDR Infiniband	25728 GB
SCARF16/ MagnaCarta/ IBIS	Intel E5-2650v3 @ 2.30GHz	56	20	1120	FDR Infiniband	7168 GB
SCARF15	Intel E5-2650v3 @ 2.30GHz	68	20	1360	FDR Infiniband	8704 GB
SCARF14	Intel E5-2650v2 @ 2.60GHz	56	16	896	QDR Infiniband	7168 GB
SCARF13	Intel E5-2660 @ 2.20GHz	84	16	1344	QDR Infiniband	5376 GB
Grand Totals		**613**		**13096**		**82560 GB**

5. APPENDIX: PUBLICATIONS AND PRESENTATIONS

Publications

	Title	Authors	Journal
1	Neutronic Developments on TOSCA and VESPA: Progress to Date.	M. Zanetti, S. Bellissima, L. del Rosso, F. Masi, M. Chowdhury, A. De Bonis, L. Di Fresco, C. Scatigno, J. Armstrong, S. Rudić, S.F. Parker, M. Hartl, D. Colognesi, R. Senesi, C. Andreani, G. Gorini, F. Fernandez-Alonso	Proceedings of 8th workshop on Inelastic Neutron Spectrometers – WINS2018 (in Physica B: Condensed Matter), submitted.
2	The neutron guide upgrade of the TOSCA spectrometer,	R.S. Pinna, S. Rudić, S. F. Parker, J. Armstrong, M. Zanetti, G. Škoro, S. P. Waller, D. Zacek, C. A. Smith, M. J. Capstick, D. J. McPhail, D. E. Pooley, G. D. Howells, G. Gorini, and F.Fernandez-Alonso.	Nuclear Instruments & Methods in Physics Research Section A, 896, 2018.
3	Detailed characterisation of the incident neutron beam on the TOSCA spectrometer	R. S. Pinna, S. Rudić, M. J. Capstick, D. J. McPhail, D. E. Pooley, G. D. Howells, G. Gorini, F. Fernandez-Alonso	Nuclear Instruments and Methods in Physics Research Section A: Accelerators, Spectrometers, Detectors and Associated Equipment, Volume 870, 2017, Pages 79-83, ISSN 0168-9002
4	TOSCA Secondary Spectrometer Upgrade.	R.S. Pinna, S. Rudić, M. Zanetti, D. Zacek, S.F. Parker, G. Gorini, F. Fernandez-Alonso	RAL Technical Reports RAL-TR-2017-013. STFC, 2017.
5	Water Participation in Catalysis: An Atomistic Approach to Solvent Effects in the Catalytic Isomerization of Allylic Alcohols	Franco Scalambra, Nicole Holzmann, Leonardo Bernasconi, Silvia Imberti, Antonio Romerosa	ACS Catal. 2018, 8, 5, 3812-3819 [doi: 10.1021/acscatal.8b00199]
6	Charge transfer in trans-combretastatins	Nicole Holzmann, Leonardo Bernasconi, Kathrin M.Callaghan,	Chem. Phys. Let., 692, 146-151 [doi:

		Roger H. Bisby, Anthony W. Parker	10.1016/j.cplett.2017.12.028]
7	Influence of charge transfer on the isomerisation of stilbene derivatives for application in cancer therapy.	Nicole Holzmann, Leonardo Bernasconi, Roger H. Bisby, Anthony W. Parker	Phys. Chem. Chem. Phys., 2018, Advance Article [doi: 10.1039/C8CP05375H]
8	Muon contact hyperfine field in metals: A DFT calculation	Ifeanyi John Onuorah, Pietro Bonfà, Roberto De Renzi	Phy. Rev. B 97, 174414, (2018)
9	Disentangling superconducting and magnetic orders in $NaFe_{1-x}Ni_xAs$ using muon spin rotation	Sky C. Cheung, Zurab Guguchia, Benjamin A. Frandsen, Zizhou Gong, Kohtaro Yamakawa, Dalson E. Almeida, Ifeanyi J. Onuorah, Pietro Bonfà, et al	Phys. Rev. B 97, 224508, (2018).
10	Inelastic neutron scattering study of reline: shedding light on the hydrogen bonding network of deep eutectic solvents	A.C.F. Araújo, J.A.P. Coutinho, M.M. Nolasco, S.F. Parker, P.J.A. Ribeiro-Claro, S. Rudić, B.I.G. Soares, P.D.Vaz	Phys. Chem. Chem. Phys., 19 (2017), 17998–18009. DOI: 10.1039/c7cp01286a
11	Inside PEF: Chain Conformation and Dynamics in Crystalline and Amorphous Domains	C.F. Araujo, M.M. Nolasco, P.J.A. Ribeiro-Claro, S. Rudić, A.J.D. Silvestre, P.D. Vaz, A.F. Sousa	Macromolecules, 51 (2018) 3515–3526. DOI: 10.1021/acs.macromol.8b00192
12	Hydrogen Bond Dynamics of Cellulose through Inelastic Neutron Scattering Spectroscopy	C. Araujo, C.S.R. Freire, M.M. Nolasco, P.J.A. Ribeiro-Claro, S. Rudić, A.J.D. Silvestre, P.D. Vaz	Biomacromolecules, 19 (2018) 1305-1313. DOI: 10.1021/acs.biomac.8b00110
13	Understanding the vibrational spectra of crystalline isoniazid: Raman, IR and INS spectroscopy and solid-state DFT study	P.J.A. Ribeiro-Claro, P.D. Vaz, M.M. Nolasco, A.M. Amado	Spectrochimica Acta Part A, 204 (2018) 452–459. DOI: 10.1016/j.saa.2018.06.073
14	Solventless Olefin Epoxidation Using a Mo-Loaded Biomass Catalyst	C. Petit, M. Velez, A.S. Mestre, C.O. Ania, P.D. Vaz, A.P. Carvalho, C.D. Nunes	ChemistrySelect, 3 (2018), 10357– 10363. DOI: 10.1002/slct.201802055

15	Exploring the Temperature Dependent Solid-State ALC Spectrum of the C6H6Mu• Radical with Ab-Initio Simulation Techniques	S. Sturniolo, L. Liborio, F.L. Pratt, S.P. Cottrell, D.B. Jochym, B. Montanari	JPS Conf. Proc. 21, 011036 (2018)
16	Enhancing relativistic electron beam propagation through the use of graded resistivity guides	R. A. B. Alraddadi, A. P. L. Robinson, J. Pasley and N. C. Woolsey	Phys. Plasmas, 25, 023104 (2018)
17	Evening out the spin and charge parity to increase T_c in unconventional superconductors	Swagata Acharya, Dimitar Pashov, Cédric Weber, Hyowon Park, Lorenzo Sponza, Mark van Schilfgaarde	arXiv:1811.05143
18	High-quality positrons from a multi-proton bunch driven hollow plasma wakefield accelerator,	Y. Li, G. Xia, K. V. Lotov, A. Sosedkin, and Y. Zhao,	Plasma Phys. Control. Fusion **61** 025012
19	Predicting asphaltene aggregate structure from molecular dynamics simulation: Comparison to neutron total scattering data	T. F. Headen, M. P. Hoepfner,	Energy and Fuels, doi:10.1021/acs.energyfuels.8b03196
20	Mechanism of enhancement of ferroelectricity of croconic acid with temperature	S Mukhopadhyay, MJ Gutmann, M Jimenez-Ruiz, DB Jochym, KT Wikfeldt, K Refson, F Fernandez-Alonso	Phys Chem Chem Phys **19**, 32216-32225 (2017). doi:10.1039/C7CP06039D
21	Emergence of glassy features in halomethane crystals	M. Moratalla, J. F. Gebbia, M. A. Ramos, L. Carlos Pardo, S. Mukhopadhyay, S. Rudić, F. Fernandez-Alonso, F. J. Bermejo, and J. L. Tamarit	Phys. Rev. B. **99**, 024301 (2019). doi:10.1103/PhysRevB.99.024301
22	A QM/MM Study of Nitrite Binding Modes in a Three-Domain Heme-Cu Nitrite Reductase	Sen, K.; Hough, M.A., Strange, R.W., Yong. C. W., Keal, T.W.	Molecules, **2018**, 23, 2997
23	Enzyme catalysis captured using multiple structures from one crystal at varying temperatures	Horrell, S.; Kekilli, D., Sen, K., Owen, R.L., Dworkowski, F.S.N., Antonyuk, S.V.; Keal, T.W., Yong, C.W.; Eady, R.R., Hasnain,	*IUCrJ* **2018**, *5*, 283

		S.S., Strange R. W.; Hough, M. A.	

Presentations

	Conference	Title	Presenter
1	Centro de Física de Materiales and Donostia International Physics Centre, 12th November 2018, San Sebastián, Spain.	(Invited seminar) Pulsed Neutrons for Materials Discovery	F. Fernandez-Alonso
2	8th workshop on Inelastic Neutron Spectrometers – WINS2018, 16-20th July 2018, Hong Kong	(Invited talk) Recent developments on TOSCA and VESPA	M. Zanetti
3	Croucher Summer School on Neutron Scattering, 9-14th July 2018, Hong Kong.	(Invited lecture) Neutron Sources and Instrumentation	F. Fernandez-Alonso
4	A 21st Century View of Disordered Matter – A Tribute to Alan Soper, 7-9th May 2018, Milton Hill, Oxfordshire, United Kingdom.	(Invited talk) Classical and Quantum Disorder – A Spectroscopic Perspective	F. Fernandez-Alonso
5	ESS IKON14 - Detectors and Data Acquisition for Instruments Meeting, 12th February 2018, Paris, France.	VESPA: Monitors and Detectors	M. Zanetti
6	Photoinduced Processes in Embedded Systems, Italy	(Poster) Influence of Charge Transfer on the Photoinduced Isomerisation of Stilbene Derivatives for Application in Cancer Therapy	N. Holzmann, L. Bernasconi, R. H. Bisby, A. W. Parker
7	Non-adiabatic quantum dynamics: From Theory to Experiments, Switzerland.	(Poster) Influence of Charge Transfer on the Photoinduced Isomerisation of Stilbene Derivatives for Application in Cancer Therapy	N. Holzmann, L. Bernasconi, R. H. Bisby, A. W. Parker
8	UK Fluids Network, Nuclear Thermal Hydraulics Special Interest Group Meeting,	Current progress on feasibility study of the application of frozen salt walls to molten salt fast reactors	S. Rolfo, G. M. Cartland-Glover, A. Skillen, C. Moulinec, D. R. Emerson, D. Litskevich, B. Merk

	Manchester, 19 February 2018		
9	Code_Saturne/Code_Neptune User Meeting 2018, Saclay, Paris, 5-6 April 2018	(Poster) Coupling the neutronics code DYN3D-MG to Code_Saturne to model molten salt fast reactors	G. M. Cartland-Glover, A. Skillen, D. Litskevich, S. Rolfo, D. R. Emerson, B. Merk, C. Moulinec
10	CCP5 Meeting on the Modelling and Simulation of Nuclear Materials in Bristol, UK, 4-5 June 2018	Feasibility of the use of frozen walls in molten salt fast reactors (MSFR-FW)	G. M. Cartland-Glover, S. Rolfo, D. Litskevich, A. Skillen, D. R. Emerson, B. Merk, C. Moulinec.
11	6th European Conference on Computational Mechanics (ECCM 6) and 7th European Conference on Computational Fluid Dynamics (ECFD 7) 11-15 Glasgow, UK, June 2018	(Paper/Presentation) Profiling and application of the multi-scale universal interface (MUI),	A. Skillen, S.M. Longshaw, G. Cartland-Glover, C. Moulinec, D.R. Emerson
12	26th International Conference on Nuclear Engineering, London UK, July 22-26, 2018 ICONE26-82170	(Refereed Paper/Presentation). Modelling the neutronics of a molten salt fast reactor using DYN3D-MG for the investigation of the application of frozen wall technology	G. M. Cartland-Glover, S. Rolfo, A. Skillen, D. R. Emerson, C. Moulinec, D. Litskevich, B. Merk
13	26th International Conference on Nuclear Engineering, London UK, July 22-26, (2018) ICONE26-82210	(Refereed Paper/Presentation) Modelling frozen salt films in a molten salt fast reactor	G. M. Cartland-Glover, S. Rolfo, A. Skillen, D. R. Emerson, C. Moulinec, D. Litskevich, B. Merk
14	CFD4NRS-7 OECD-NEA & IAEA Workshop, Shanghai, China, September 4-6, 2018	(Refereed Paper/Presentation) On the numerical modelling of frozen walls in a molten salt fast reactor.	G. M. Cartland-Glover, S. Rolfo, A. Skillen, D. R. Emerson, C. Moulinec, D. Litskevich, B. Merk
15	International Nuclear Engineering Conference 2018, Manchester, UK, 4-5 October 2018	Modelling frozen salt films in a molten salt fast reactor	G. M. Cartland-Glover, S. Rolfo, D. Litskevich, A. Skillen, D. R. Emerson, B. Merk, C. Moulinec.
16	12th International Topical Meeting on Nuclear	(Refereed Paper/Presentation) On the feasibility of the	G. M. Cartland-Glover, S. Rolfo, A.

	Reactor Thermal-Hydraulics, Operation and Safety, NUTHOS-12, Qingdao, China, October 14-18, 2018	application of frozen walls to a molten salt fast reactor	Skillen, D. R. Emerson, C. Moulinec, D. Litskevich, B. Merk
17	Supercomputing 2018, Dallas, Texas, 12-15 November 2018	(Stand Poster) Simulating frozen walls within a molten salt fast reactor	G. M. Cartland-Glover
18	PRACE-MaX Tutorial on high-throughput computations: general methods and applications using AiiDA. CINECA – Bologna, Italy, 30th May – 1st June 2018	(Poster Presentation) Theoretical study of muon implantation site, its interactions and quantum effects in MnSi'	I. J. Onuorah, P. Bonfà, R. De Renzi
19	New generation in Strongly correlated electrons systems, Donostia- San Sebastian, Spain, 3rd-7th September, 2018	Theoretical study of muon implantation site, its interactions and quantum effects within an effective anharmonic approximation.	I. J. Onuorah
20	Muon spectroscopy user meeting 2018. Cosener's House, Abingdon, UK. 16th -17th July, 2018	Candidate muon stopping sites in NaFe1-xNixAs and Quantum effects within an anharmonic approximation.	I. J. Onuorah
21	Jornadas CICECO 2018, June 2018, Aveiro, Portugal	(Poster) Inside PEF: chain conformation and dynamics in crystalline and amorphous domains	C.F. Araújo, M.M. Nolasco, P.J.A. Ribeiro-Claro, S. Rudić, A.J.D. Silvestre, P.D. Vaz, A.F. Sousa
22	X Iberian Spectroscopy Conference, XXVI National Spectroscopy Meeting, July 2018, Lisbon, Portugal	(Poster) Vibrational portrait of a deep eutectic solvent: shape and hydrogen bonds	C.F. Araújo, J.A.P. Coutinho, M.M. Nolasco, S.F. Parker, P.J.A. Ribeiro-Claro, S. Rudić, B.I.G. Soares, P.D. Vaz
23	PATh Spring Workshop 2017 – 2nd edition – Deep Eutectic Solvents (DES), Aveiro, Portugal, June 2017	Architecture of deep eutectic solvents – lessons learned from vibrational spectroscopy	C. Araujo, J. A. P. Coutinho, M. M. Nolasco, S.F. Parker, P. J. A. Ribeiro-Claro, S. Rudić, B. I. G. Soares, P. D. Vaz
24	μSR2017 Conference, Sapporo, June 2017	Probing Quantum Critical Spin Liquids with μSR	F. Pratt

25	ISIS Muon User and Site Calculation Meeting, Abingdon, July 2018	CalcALC: a user tool for predicting and interpreting ALC and QLCR spectra	F. Pratt
26	ISCM Conference, Busan, Korea, July 2018	(Invited Presentation) μSR of Layered Molecular Conductors: from Vortex Phases in Superconductors to Quantum Critical Phases in Spin Liquids	F. Pratt
27	ICCC Conference, Sendai, Japan, Aug 2018	Recent advances in molecular conductors: functionality	F. Pratt
28	ICMFS/RIKEN Symposium, Sanur, Indonesia, Nov 2018	(Invited Talk)	F. Pratt
29	Ab Initio Spin Modelling, November 26 - 28, 2018, Lausanne, Switzerland	(Invited Talk) Towards a comprehensive Ab initio Description of Magnetic phenomena	M. van Schilfgaarde
30	Lawrence Berkeley Laboratory, December 2018		M. van Schilfgaarde
31	Arizona State University, December 2018	(Seminar)	Mark van Schilfgaarde
32	AWAKE Collaboration Meeting, CERN, Switzerland, 21 September 2018	High-quality positrons from a multiproton bunch driven hollow plasma wakefield accelerator	Y. Li (presenter), G. Xia, K. V. Lotov, A. Sosedkin, and Y. Zhao
33	Channeling 2018, Ischia, Italy	Towards positron acceleration and high quality preservation in nonlinear wakefields in hollow plasma	Y. Li (presenter), G. Xia, K. V. Lotov, A. Sosedkin, and Y. Zhao
34	SATIF-14: 14th Specialists' workshop on Shielding aspects of Accelerators, Targets, and Irradiation Facilities-South Korea	Monte Carlo simulation of ISIS Target Station 1 using FLUKA code and comparion with the MCNPX reference model	L. Quinteri, S. Lilley, G. Skoro
35	Joint conference on Quasielastic neutron scattering and the workshop on inelastic neutron spectrometers	Modelling of structure and dynamics of molten NaF using first principles molecular dynamics.”	S Mukhopadhyay and F Demmel.

	QENS/WINS 2016: Probing Nanoscale Dynamics in Energy Related Materials, 5–9 September 2016, Potsdam, Germany		
36	DPG-Frühjahrstagung und EPS-CMD27, 11-16th March, Berlin, Germany (2018).	Role of Hydrogen Bonds in Organic Ferroelectrics using Neutron Scattering and First principles Simulations	S. Mukhopadhyay
37	Neutron and Muon Users Meeting, 25-27th April, University of Warwick, Warwick, UK (2018).	Mechanism of Ferroelectricity in Organic Ferroelectric Croconic Acid using Neutron Scattering and First principles Simulations	S. Mukhopadhyay
38	ILL & ESS users Meeting, 11-12th October, Grenoble, France (2018).	How Hydrogen & Halogen Bonds Influence Mechanism of Ferroelectricity in Organic Ferroelectrics	S. Mukhopadhyay
39	International Conference on Perspective in Vibrational Spectroscopy (ICOPVS 2018), 25-29th November, Bhaba Atomic Research Center, Mumbai, India (2018).	Fingerprint Information of Ferroelectricity in Organic Ferroelectrics using Vibrational Neutron Spectroscopy	S. Mukhopadhyay
40	NOMAD Summer - A hands-on course on tools for novel-materials discovery, CECAM-HQ-EPFL, Lausanne, Switzerland	(Poster) Computer Simulations for Interpreting Muon-spin Relaxation Experiments	L. Liborio, S, Sturniolo, D. Jochym
41	TranSIESTA and TBtrans workshop, DTU, Lyngby, Denmark		L. Liborio
42	Italian Neutron Scattering Conference 2018 (4-6 July 2018, Parma, Italy)	(Poster) Probing Structure and Mobility of Proteins in the Amorphous State at Low Hydration	E. Chiessi
43	ILL & ESS users Meeting, 11-12th October, Grenoble, France (2018).	(Poster) Probing Structure and Mobility of Proteins in the Amorphous State at Low Hydration	M. Telling
44	The 6th International symposium on Negative	The RF H−Ion Source Project at RAL	O. Tarvainen

	Ions, Beams and Sources, Novosibirsk, Russia		

6. APPENDIX: SCARF QUEUE USAGE 2017-18

General SCARF Queues

SCARF migrated to the SLURM batch system, and took this opportunity to update the queues provided. As the SLURM service was all RedHat Enterprise 7, the scarf-rhel7 queue was retired. Two new queues were provided, the preemptable queue, which allows users to run across all hardware with the caveat that the job may be ended if the nodes were required by a job in another queue; and the devel queue, which is intended for small, short, interactive workloads.

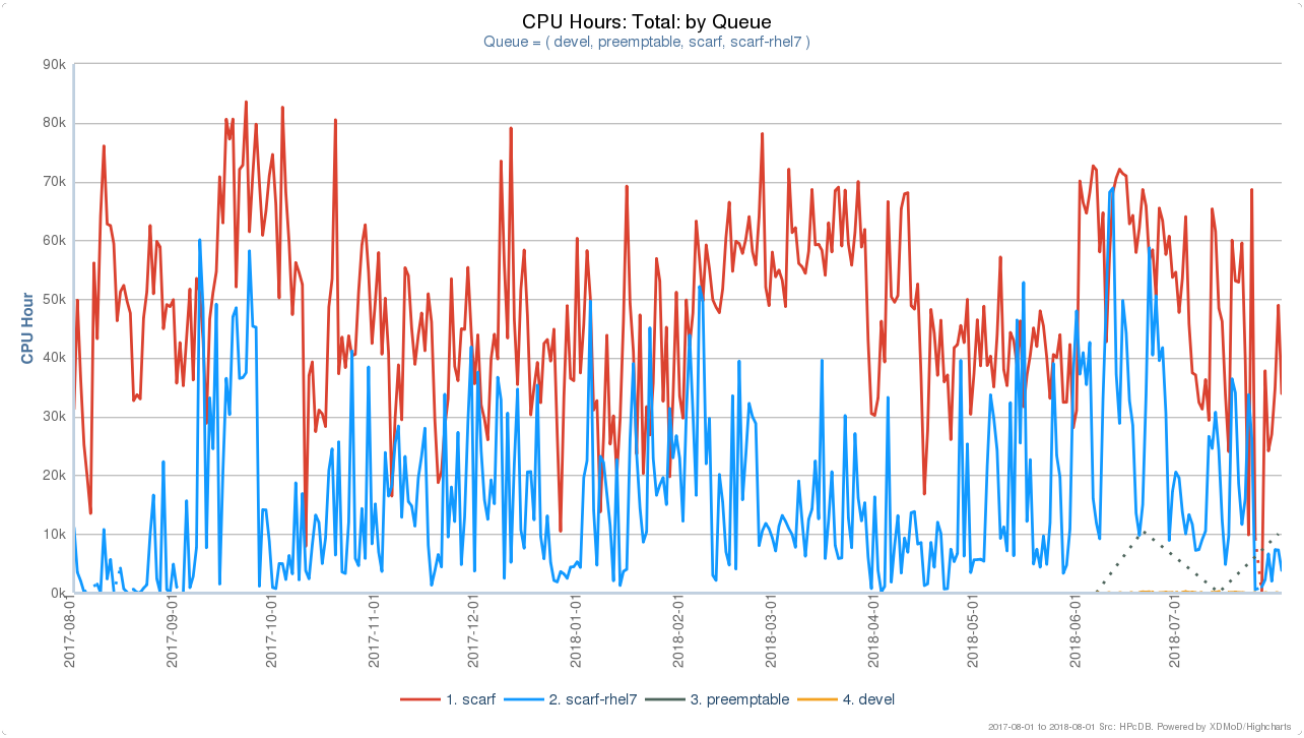

Figure 53: SCARF Queue Usage

The LSF "SLA" mechanism was used to allow groups of users to get preferential access to portions of hardware they have contributed money to purchase, while still making the hardware available to other users' jobs up to 24 hours in length. This was in place for ISIS on SCARF13 and SCARF17 and ISIS and CLF Octopus on SCARF14 and SCARF15.

The following graphs show the usage on each combination of user community and hardware. The blue line shows the level that is guaranteed to the user community. The red line shows usage by the community of their guarantee. The yellow line shows the community's usage of the hosts covered by the particular SLA.

This functionality is not available in Slurm so the preferential access has been implemented as higher fairshare priority for ISIS and separate partitions for CLF Octopus.

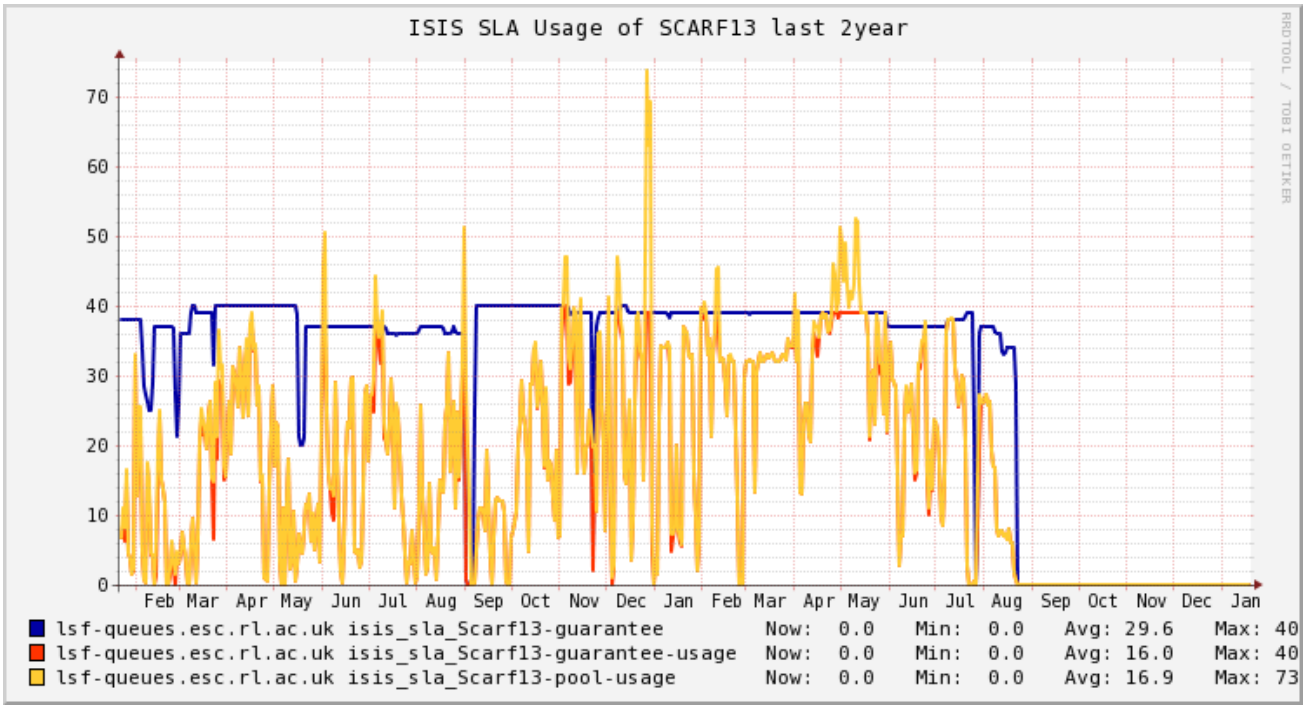

Figure 54: ISIS SLA Usage of SCARF 13

While the yellow line does exceed the blue line on a number of occasions, for the most part ISIS usage of SCARF13 has been well under that guaranteed to them, averaging at just under half of the guaranteed hosts.

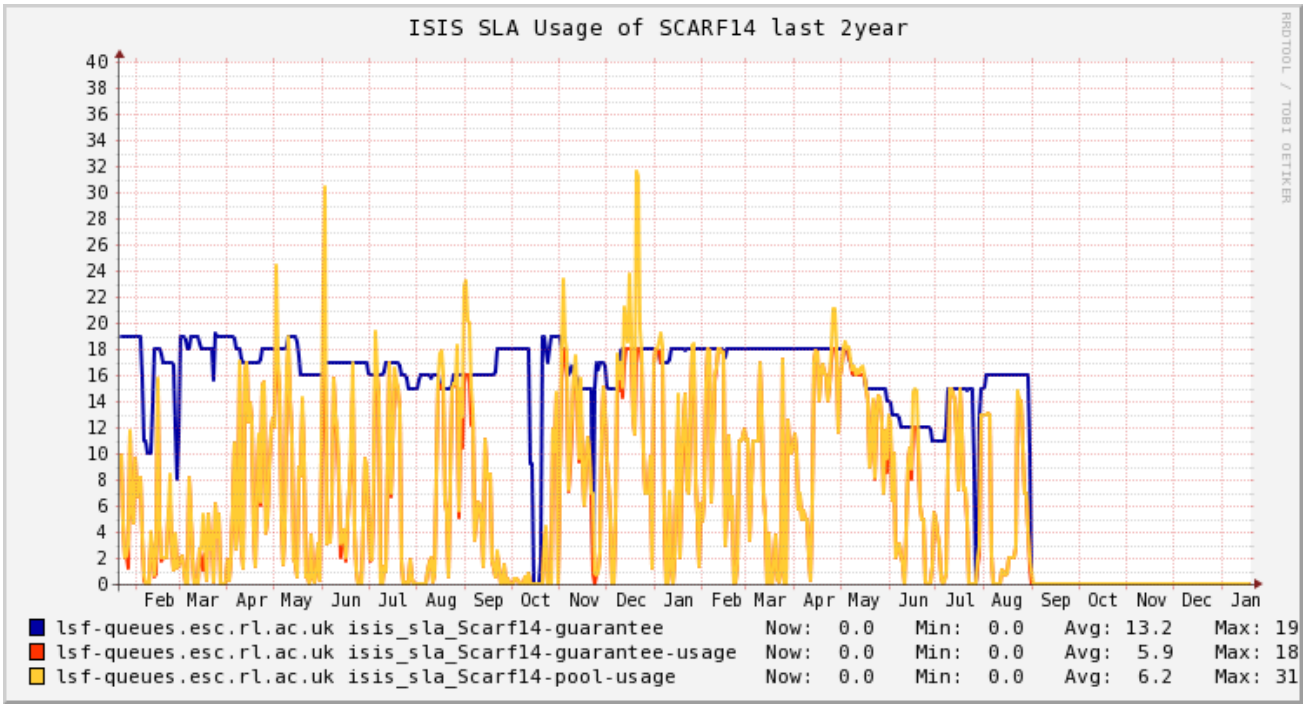

Figure 55: ISIS SLA Usage of SCARF 14

The SCARF14 SLA for ISIS shows a similar pattern of usage to that of SCARF13 above.

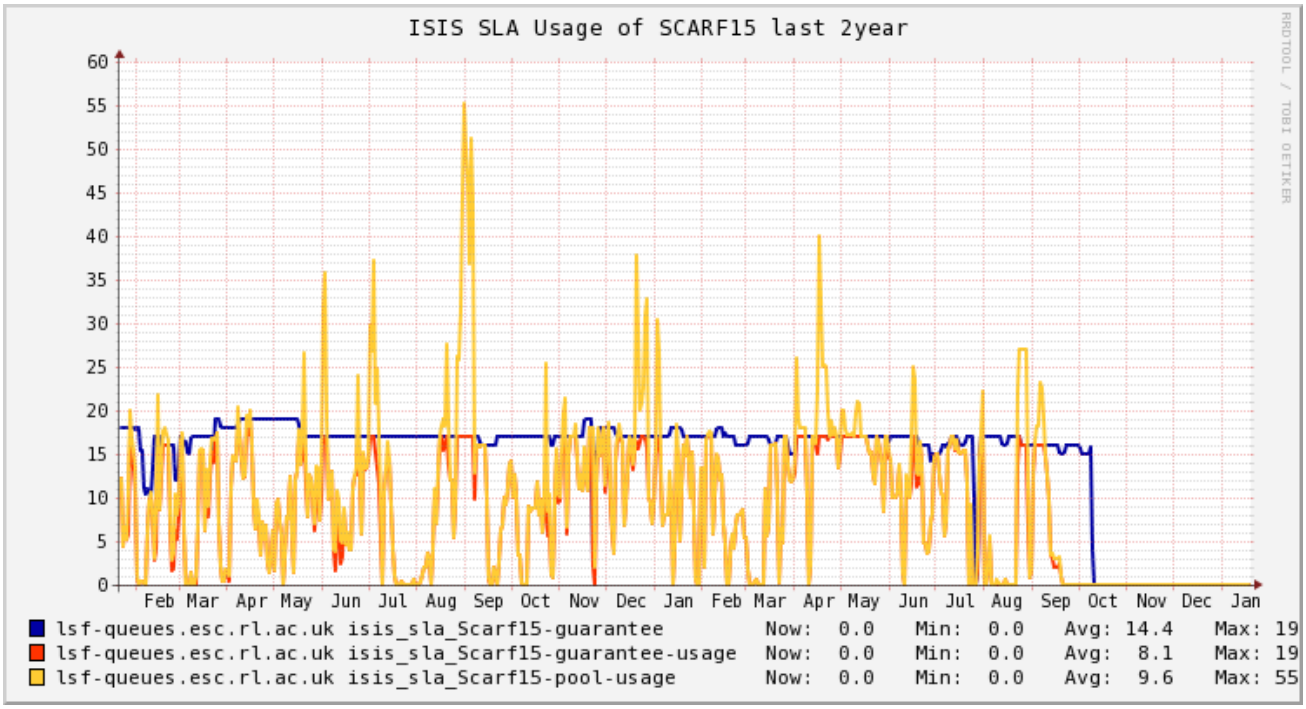

Figure 56: ISIS SLA Usage of SCARF 15

While the SCARF15 usage broadly fits the same pattern as SCARF13 and SCARF14, the periods where usage exceeds the guarantee are much larger.

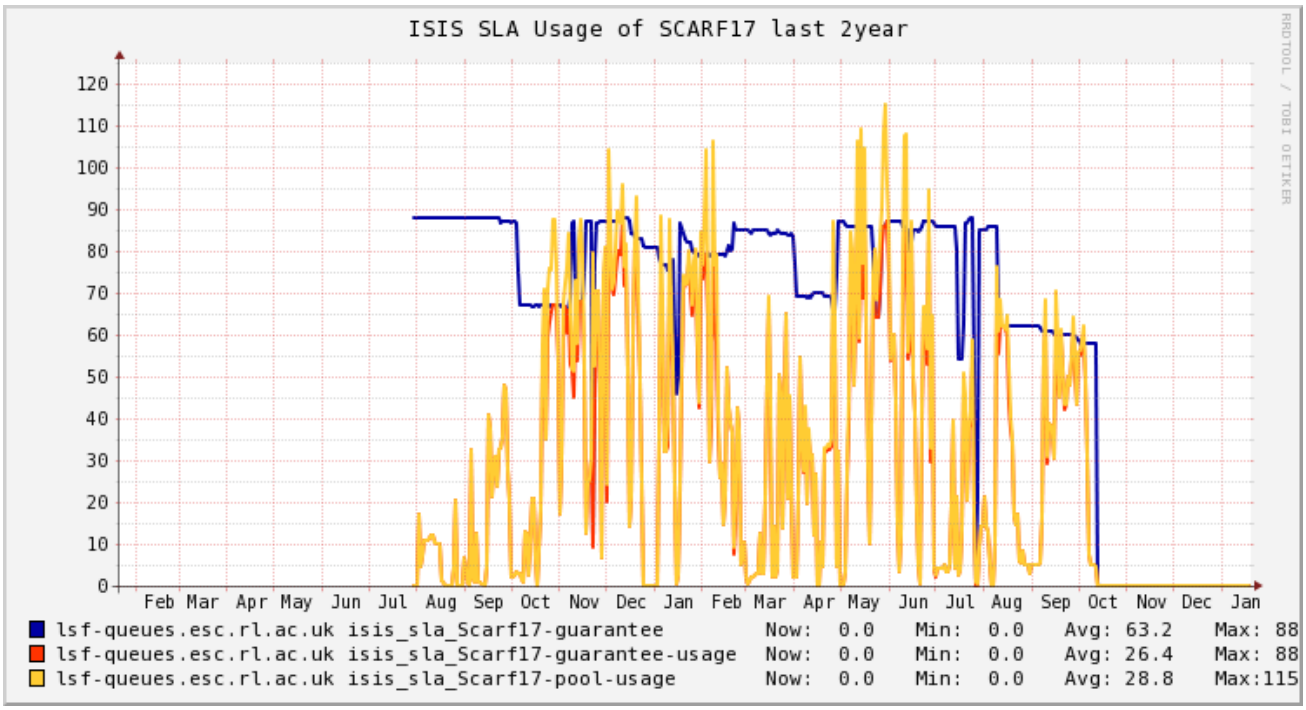

Figure 57: ISIS SLA Usage of SCARF 17

ISIS usage of SCARF17 followed same the pattern as the older hardware.

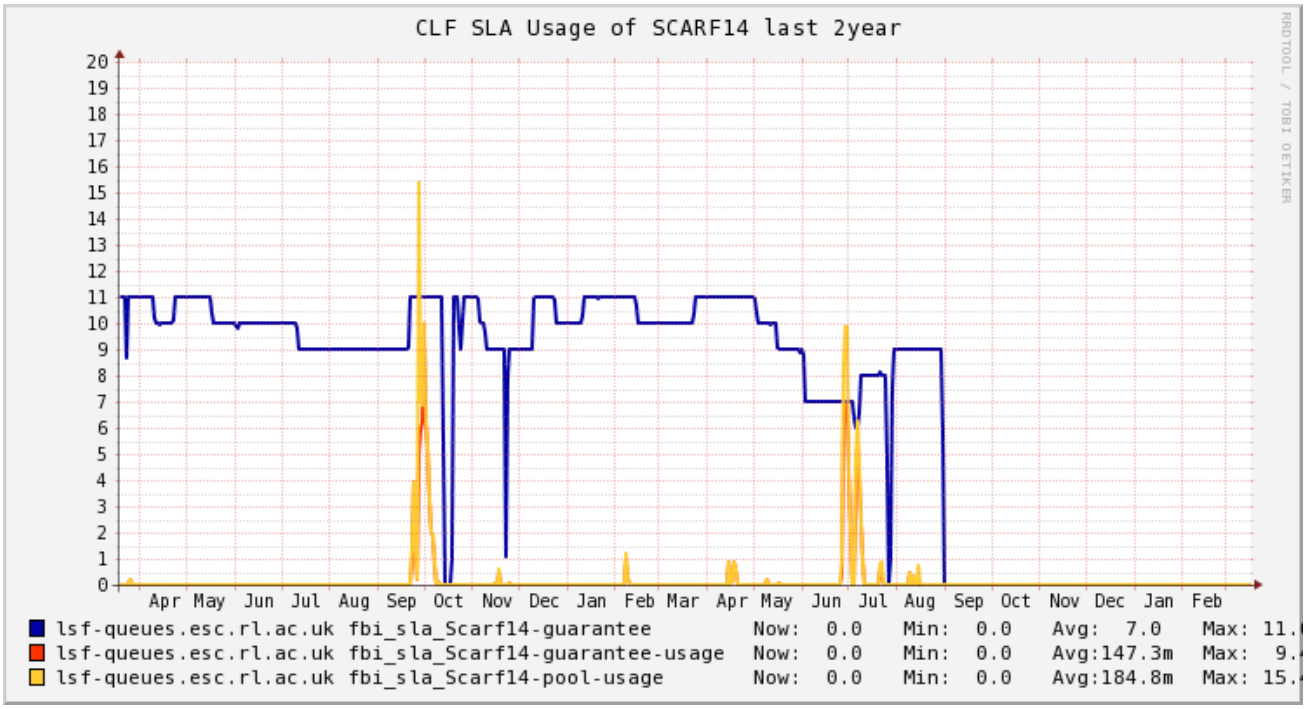

Figure 58: CLF SLA Usage of SCARF 14

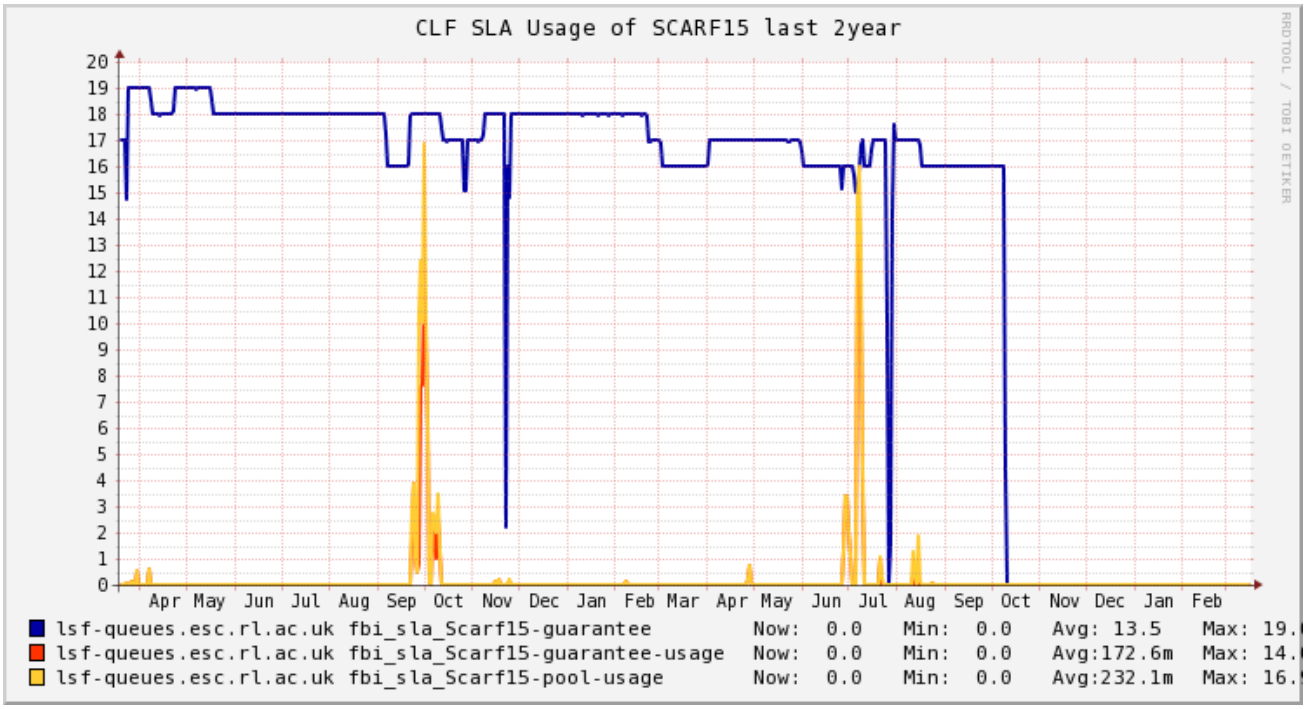

Figure 59: CLF SLA Usage of SCARF 15

The SCARF14 and SCARF15 plots for CLF FBI show that while they are not regularly making use of their guaranteed hosts, there have been some bursts of activity throughout the year.

MagnaCarta, Lexicon2 and DeRevolutionibus Queues

These queues are primarily for CLF Plasma Physics use. MagnaCarta has 480 cores purchased in 2016.. DeRevolutionibus has 1608 cores purchased in 2017. Lexicon2 had 544 cores purchased in 2010, but was decommissioned with the move to Slurm.

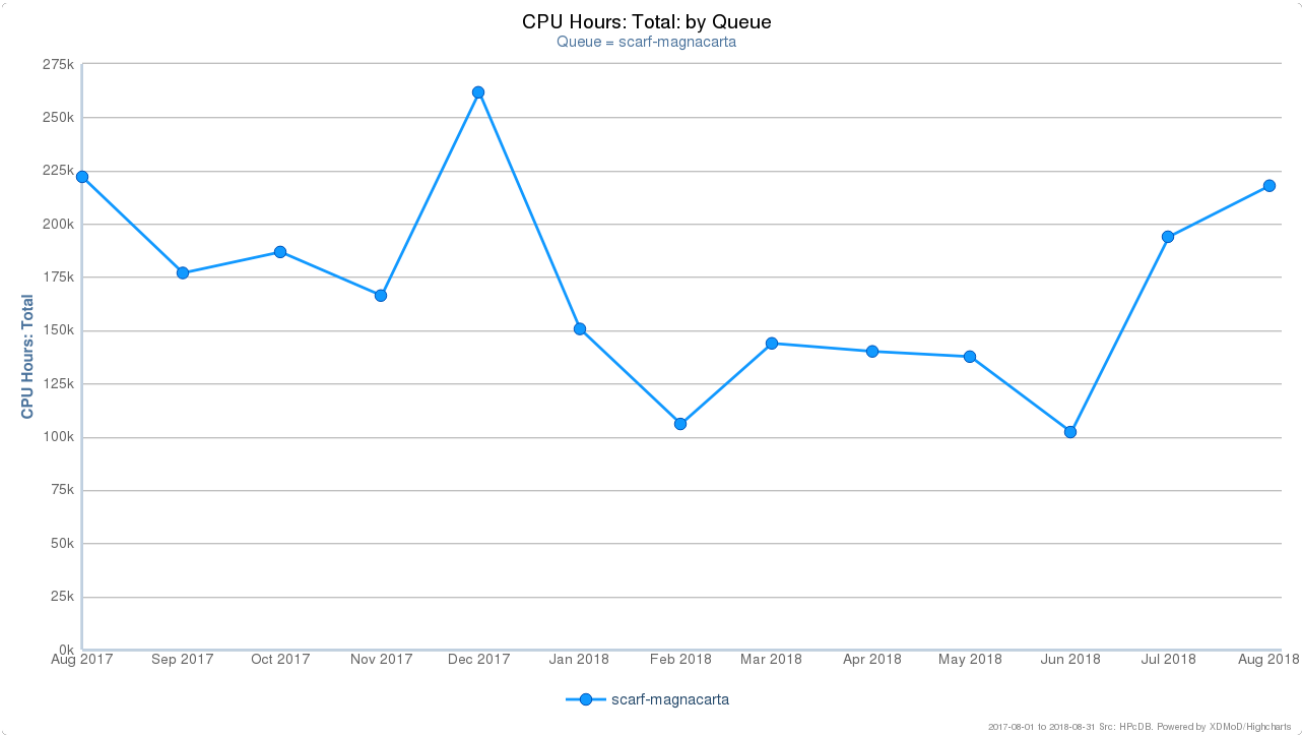

Figure 60: SCARF-MagnaCarta Usage

The graph for the SCARF-MagnaCarta queue shows significant usage, as it is available to CLF external collaborators.

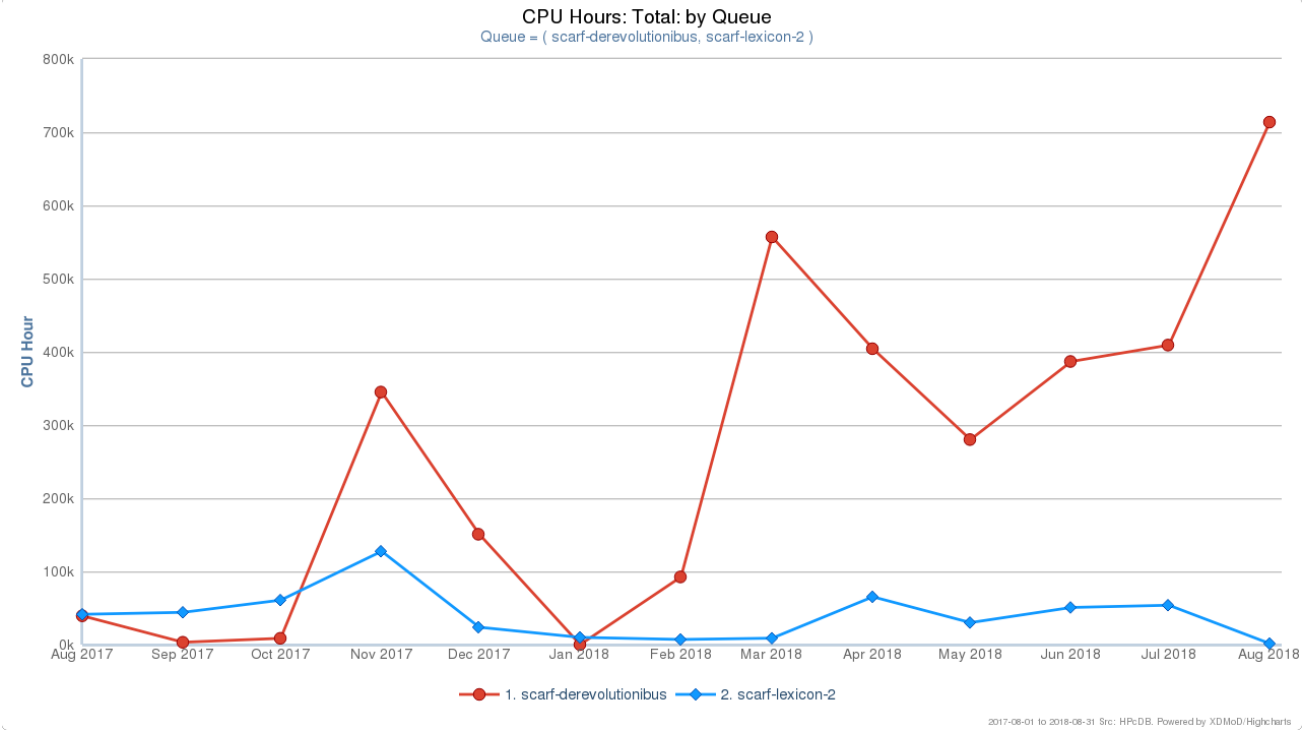

Figure 61: SCARF Lexicon-2 and DeRevolutionIbus Usage

SCARF-Lexicon-2 and DeRevolutionibus continue to be used for higher priority MagnaCarta users and on demand to support CLF experiments, though clearly usage of DeRevolutionIbus is now outstripping Lexicon 2.

SCARF-IBIS

SCARF-IBIS has a capacity of 240 CPU cores. They are used for the Intense Beams in Synchrotrons collaboration.

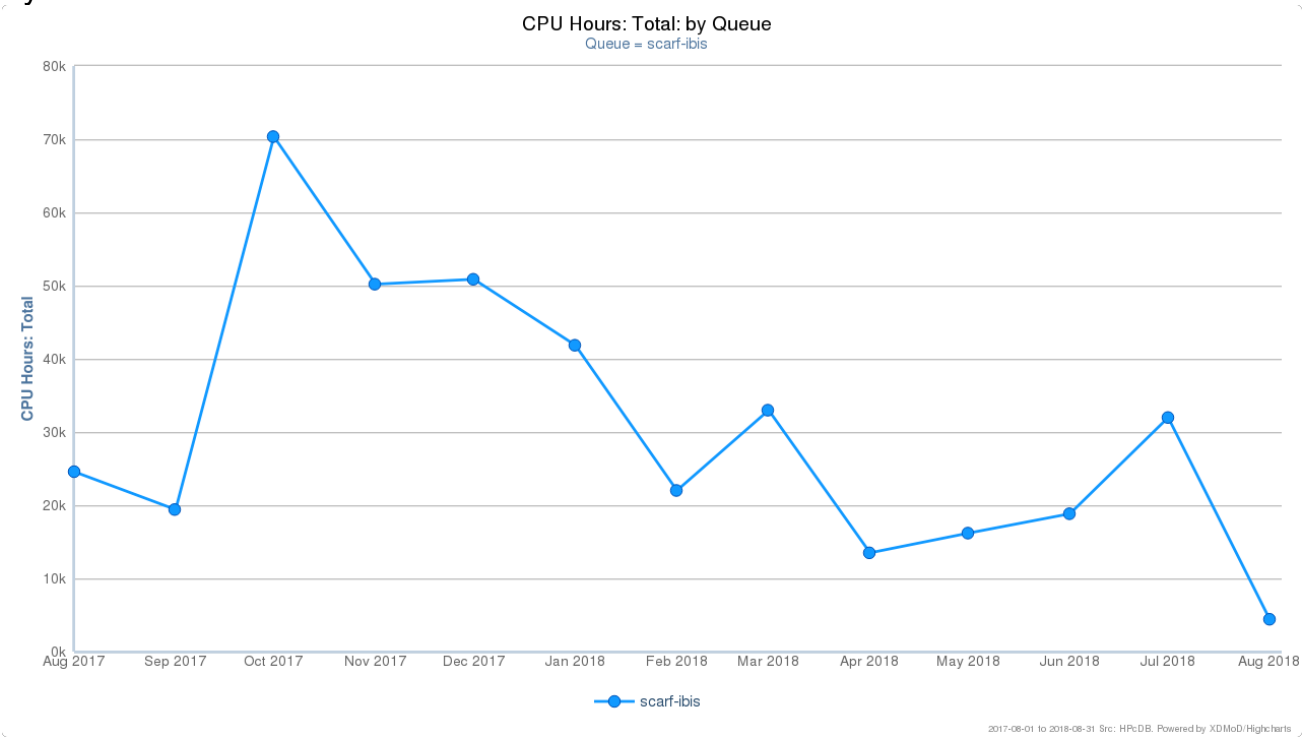

Figure 62: SCARF-IBIS Usage

SCARF Total Power draw

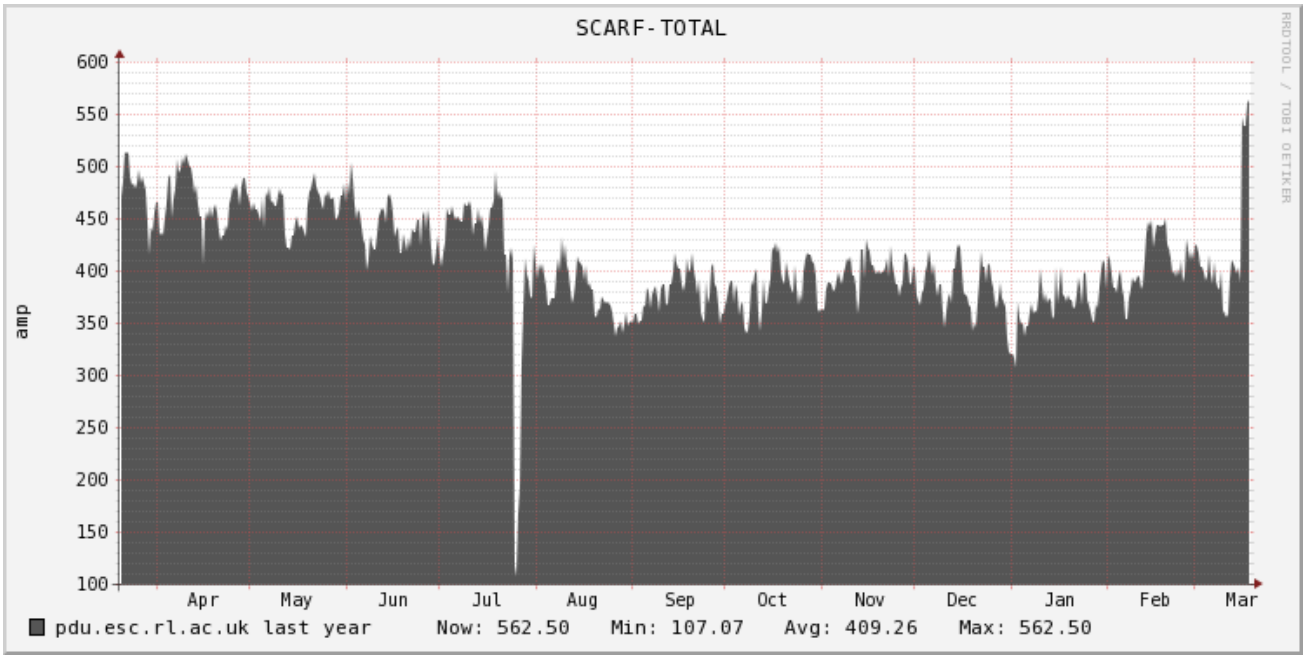

Figure 63: SCARF Power Usage

In the graph above, the outage for R89 Power Testing in July can be clearly. Also noticeable is a dip in the power after that period – this is due to taking SCARF10, 11 and 12 out of service as part of the migration to SLURM. SCARF18 was only added to the monitoring recently, and its impact can be seen by the sudden increase at the right-hand edge of the graph. The approximate average power draw of the SCARF cluster is about 560 amps or 134 kW, excluding the power needed to cool, pump and move cold air.

Year Purchased	Gflops/W
2013	0.59
2014	0.98
2015	1.95
2016	1.95
2017	2.05
2018	3.05

Figure 64: GFlops/W for SCARF generations of equipment

From the above table it is clear that the Gflops/W achieved increase per generation of the SCARF equipment. This supports the continual refresh rate of SCARF hardware rather than a big bang approach. SCARF16 is the same hardware as SCARF15 which accounts for the identical Gflops/W.

Filesystem Usage

The plot below outlines the use of the Panasas filespace on the SCARF service. The filespace is shared across a number of projects therefore not all space is available to SCARF users, but SCARF users benefit as increasing the amount of space also increases the bandwidth to the storage as files are redistributed around the Panasas system automatically. A new storage system has been deployed which increases the capacity.

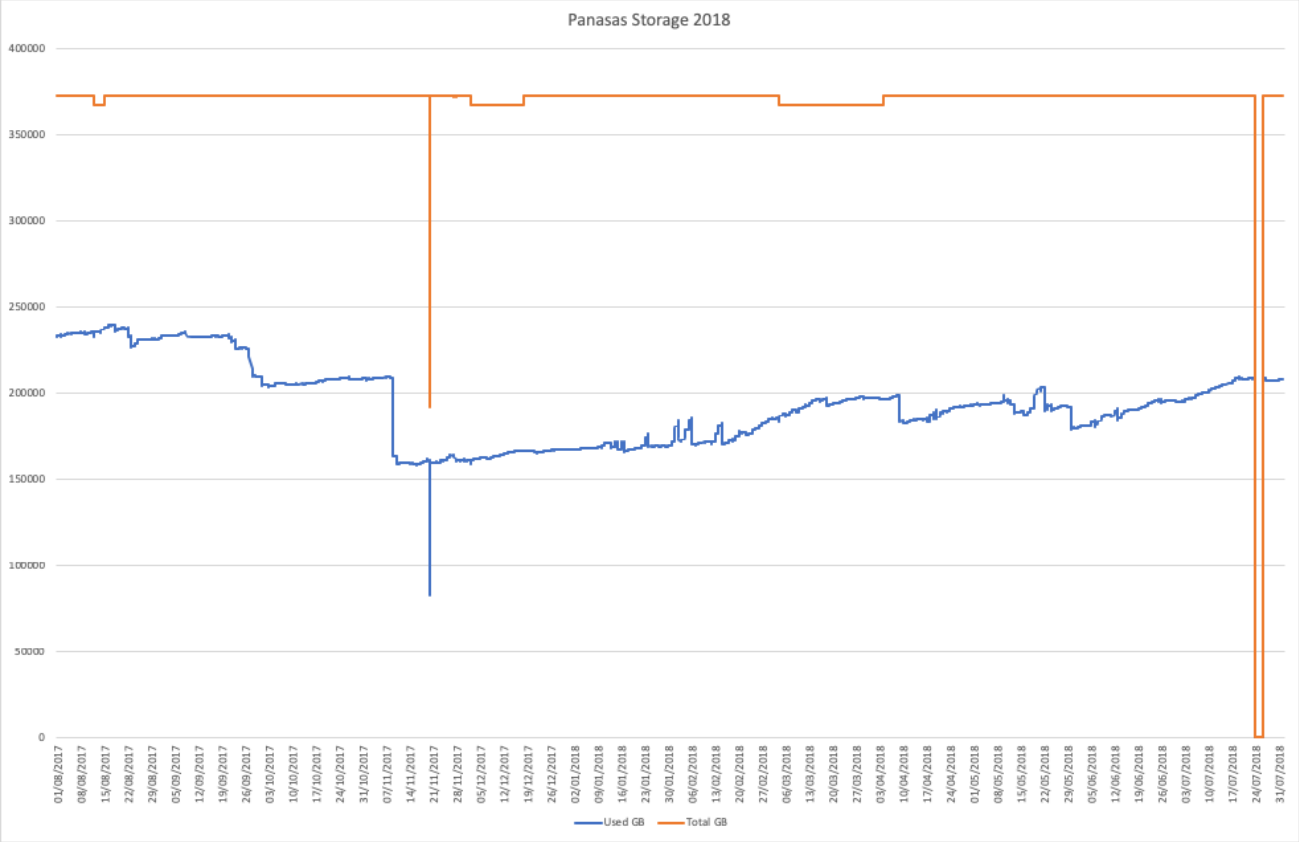

Figure 65: Filespace usage on the Panasas Storage

Networking

The diagram below shows the SCARF compute clusters embedded in the larger Research Infrastructure group's networking infrastructure. This year a significant change was the migration to the new RIG network infrastructure and the consolidation of the Panasas Storage and SCARF compute nodes under a single dedicated switch. The new RIG network infrastructure allows increased bandwidth to other departments and also permits connecting to the Scientific Computing bridge network which will enable transfers between SCD networks to bypass the STFC core network allowing additional capacity for high-speed transfers.

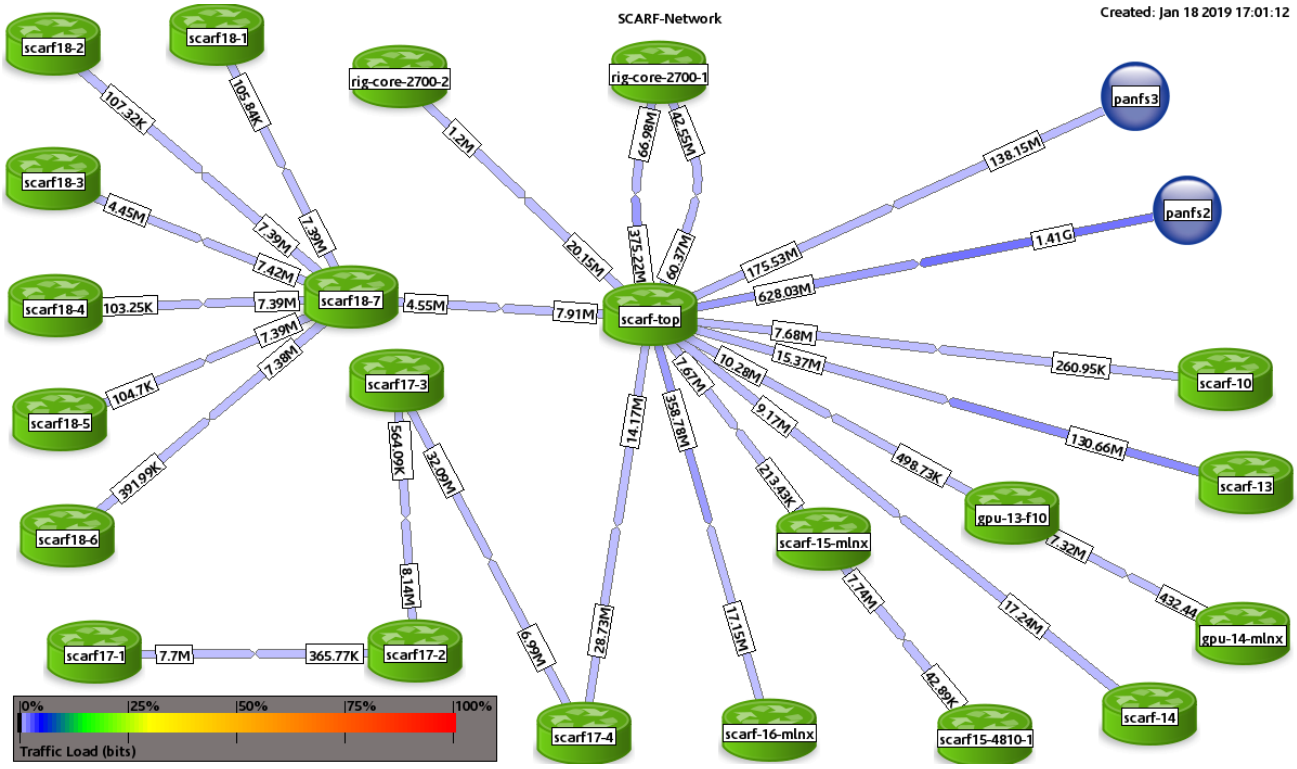

Figure 66: SCARF Network Topology

7. APPENDIX: SCARF DEVELOPMENTS

It has been a busy year for the SCARF service. Users' will have noticed most impact with the additional of capacity and upgrades to applications. However, a lot of effort goes into improving the management of SCARF.

Technical Developments

- In August 2018 the hardware tranche of 148 nodes providing 3552 cores was made available
- SCARF moved to the SLURM batch system
- SCARF completed its migration to the RHEL7 operating system
- During power testing of the R89 machine room the network configuration of SCARF was revised
- The Panasas storage system was upgraded to a new software version to allow concurrent access to the new Panasas storage system, which will replace the existing one

Application Stack

A selection of new or updated applications is in the table below:

Application	Area	Version
Cuda	Allows harnessing of GPUs	10.0.130
GNU compiler	Fortran, C, C++ compilers and Maths libraries	8.1.0
PGI compilers	Fortran, C, C++ compilers and Maths libraries	18.7
CASTEP	Computational Chemistry	17.2.1

A full list of the available software on SCARF can be found on the SCARF website: http://www.scarf.rl.ac.uk/applications-libraries.

8. APPENDIX: INDEX OF FIGURES